ON THE CONTROLLABLE SPIN-WAVE DYNAMICS IN MAGNONIC CRYSTALS

A Dissertation

by

ANKANG LIU

Submitted to the Graduate and Professional School of
Texas A&M University
in partial fulfillment of the requirements for the degree of

DOCTOR OF PHILOSOPHY

Chair of Committee,	Alexander Finkel'stein
Committee Members,	Artem G. Abanov
	Donald G. Naugle
	Peter Kuchment
Head of Department,	Grigory Rogachev

August 2023

Major Subject: Physics

ABSTRACT

Spin waves are the collective wave excitations in the magnetically ordered system, which have the frequencies typically ranged from GHz up to even THz. In recent years, the study of spin waves, which is referred to as "magnonics", has been significantly advanced; and the low-damping coherent spin waves are considered as a suitable candidate for performing rapid data processing and wave computing. The scalability of such spin-wave based computing devices is rather promising due to the possibilities of exciting spin waves with wavelengths down to the nanometer range. Magnonic crystals are various forms of spatial modulation of magnetic properties that can be seen as magnetic metamaterials. The magnonic crystals, as a widely used approch to tailor the spin-wave band structure and an effective way to control the spin-wave propagation, have been studied extensively. In this dissertation, we explore the possibilities of utilizing various kinds of magnonic crystals for the controllable spin-wave dynamics in different magnetic systems.

We first develop a description of spin waves in a $3D$ quantum XY antiferromagnet (AFM) in terms of macroscopic variables, magnetization and Néel vector densities. We consider a layered AFM with spins located on the honeycomb lattice. We show that, in the discussed system, the spectrum of spin waves consists of four modes, all well captured by our macroscopic description. The gapless mode of the spin waves, i.e., magnons, is described by a system of equations, which has a structure general for the Goldstone mode in AFMs. We demonstrate that the parameters in the spin Hamiltonian can be evaluated by fitting the experimental data with the results obtained for the four modes using the macroscopic variable approach. The description of AFM in terms of macroscopic variables can be easily extended to the case when the lattice of the magnetic substance is deformed by an external strain or acoustic wave.

Next, we study the spin-wave dynamics in such a layered AFM in the presence of a periodic lattice deformation. We suggest to use spatially modulated strain (a type of magnonic crystals) for the control of a spin wave propagating inside a bulk AFM. The modulation with the wave vector q, by virtue of magnetoelasticity, mixes spin waves with wave vectors near $q/2$ and $-q/2$. This

leads to lifting the degeneracy of the symmetric and antisymmetric eigenstate combinations of these waves. Therefore, a moving spin wave being subjected to the lattice modulation after some time alters its propagation direction to the opposite one, and so on. The resulting picture reminds one of a tunneling particle in a symmetric double-well potential. The effect can be utilized for the control of the spin-wave propagation that can be useful for magnonic applications. The control may include a delay line element, filtering, and waveguide of the spin waves in AFM.

For a ferromagnet (FM), we investigate its spin-wave dynamics under a switchable current-induced magnonic crystal. In this case, we consider a ferromagnetic (FM) sample with a metallic meander pattern (whose spatial modulation is described by a wave vector q) fabricated on its top surface. The magnonic crystal will be switched on and off by applying a current to the meander structure. For a conventional magnonic crystal with direct current (DC) supply, the spin waves around $q/2$ are resonantly coupled to the waves near $-q/2$, and similar to the periodically deformed AFM, a band gap is opened at $k = \pm q/2$. We further demonstrate that if instead of the DC current the magnonic crystal is supplied with an alternating current (AC), then the band gap is shifted to k satisfying $|\omega_s(k) - \omega_s(k-q)| = \omega_{ac}$; here $\omega_s(k)$ is the dispersion of the spin wave, while ω_{ac} is the frequency of the AC modulation. The resulting gap in the case of the AC magnonic crystal is the half of the one caused by the DC with the same amplitude of modulation. The time evolution of the resonantly coupled spin waves controlled by properly suited AC pulses can be well interpreted as the motion on a Bloch sphere. The tunability of the AC magnonic crystal broadens the perspective of spin-wave computing.

ACKNOWLEDGMENTS

I would like to express my deep gratitude and sincere thanks to my advisor, Dr. Alexander Finkel'stein, for his patient guidance, consistent support, and invaluable feedback throughout the entire process of completing this dissertation and my graduate study. His dedication, insightful criticism, and constructive advice have been essential in shaping my research, improving the quality of my work, and broadening my perspective as a scholar.

I would also like to thank my parents and girlfriend for their constant encouragement during my Ph.D. study. Without their support, I would not be where I am today.

CONTRIBUTORS AND FUNDING SOURCES

Contributors

This work was supported by a dissertation committee consisting of Professor Alexander Finkel'stein [advisor], Artem Abanov, and Donald Naugle of the Department of Physics & Astronomy and Professor Peter Kuchment of the Department of Mathematics.

All work conducted for the dissertation was completed by the student under the supervision of Professor Alexander Finkel'stein.

Funding Sources

Graduate study was supported by the graduate teaching and research assistantship from the Department of Physics & Astronomy of Texas A&M University.

NOMENCLATURE

AFM	Antiferromagnet/Antiferromagnetic
FM	Ferromagnet/Ferromagnetic
DC	Direct current
AC	Alternating current
YIG	Yttrium iron garnet
RWA	Rotating wave approximation

TABLE OF CONTENTS

Page

LIST OF FIGURES

1. INTRODUCTION*

Classical computers, which are based on electronic circuits, exploit binary digits, known as bits, to store and process information. Each bit has a value of either 0 or 1, which can be represented by an electrical signal. Complex calculation tasks are performed via logic gates, which are constructed using billions of transistors on integrated circuits. The processing speed of a classical computer is mainly determined by the number of transistors on an integrated circuit; and according to the prediction of Moore's Law, this number approximately doubles every two years. Over the past few decades, the computational capacity of classical computers has grown rapidly. However, it will become more and more impractical to maintain this exponential growth as the size of transistors becomes smaller and we approach the limits of classical physics.

Quantum computers, on the other hand, provide a potential solution to these limitations and have been extensively studied to continue enhancing the computing capabilities. Unlike classical computers, a quantum computer explores the physics of quantum superposition and entanglement to perform computations. Instead of bits, quantum computing uses quantum bits, or qubits, which can be in a superposition of states (i.e., a linear combination of both 0 and 1 states at the same time). This enables quantum computers to process a large amount of information simultaneously and execute certain types of calculations much faster than the classical ones. Although quantum computing shows great promise, its practical implementation in the real world is severely limited by the intrinsic susceptibility of a quantum system to external perturbations and noises. To build a truly functional quantum computer, the issue of quantum decoherence in multiple-qubit system must be addressed.

Classical waves lack the full capacity for quantum entanglement, but they still possess the superposition property. Lloyd has theoretically shown that, with an extra resource overhead, interference of waves can be exploited for building a computing device that outperform the clas-

---

*Part of this chapter is reprinted with permission from "Spin-wave dynamics controlled by tunable ac magnonic crystal" by Ankang Liu and Alexander M. Finkel'stein, 2023. Phys. Rev. B (to be published), Copyright 2023 by American Physical Society.

sical one on database search [1]. This is accomplished by implementing a specific version of Grover's algorithm that does not involve quantum entanglement. In addition, other studies (e.g., Refs. [2, 3, 4, 5]) have suggested that quantum speedup may rely more on the parallelism of a quantum system rather than on the entanglement. In these works the authors also discussed the possibilities of using classical waves to achieve quantum-like speedup.

Spin waves are the collective wave excitations in the magnetically ordered system, which have the frequencies typically ranged from GHz up to even THz. In fact, the utilization of spin waves for the purposes of quantum-information exchange was proposed long ago in Ref. [6]. In recent years, the study of spin waves, which is referred to as "magnonics", has been significantly advanced, see Refs. [7] and [8] for reviews. As it is shown in Refs. [9, 10, 11], the spin waves excited in the low-damping ferromagnetic (FM) material yttrium iron garnet (YIG) can have both life time and coherence time longer than 100 ns. As a result, the low-damping coherent spin waves are now considered as a suitable candidate for performing rapid data processing and wave computing [9, 10, 11, 12, 13, 14, 15]. The scalability of such spin-wave based computing devices is rather promising due to the possibilities of exciting spin waves with wavelengths down to the nanometer range [16, 17]. Specifically, as demonstrated in Ref. [13], a computing machine relying on the spin-wave superposition exhibits faster performance on database searching tasks compared to a classical digital computer. Futhermore, the authors claim that "classical wave-based devices can perform some of the quantum algorithms with the same efficiency as quantum computers as long as quantum entanglement is not required". The results of this study imply that spin-wave-based computing devices have the potential to achieve quantum-like speedups on certain tasks, which provide an alternative avenue to bypass the intractable issue of quantum decoherence when building a quantum computer.

In the abovementioned work, the qubit state was encoded as a linear superposition of two spin waves with different phases, with each "qubit" sent through its own waveguide (a thin YIG stripe that guides spin waves) and controlled by an individual phase shifter (an apparatus that adjusts the phase of a spin wave). However, scaling up such a spin-wave computing device will be a significant challenge. To address this challenge, in this dissertation we study the spin-wave dynamics in various kinds of magnonic crystals for different magnetically ordered systems, and finally we explore the possibility of using AC magnonic crystals to control different spin-wave pairs. We expect that distinct spin-wave pairs will be independently manipulated by the AC magnonic crystals with different *modulating frequencies* through what we will call the "*shifted resonance*". The key advantage of the proposed scheme is that all pairs of spin waves in the same waveguide can be simultaneously controlled by a single hardware, which has a fixed spatially modulation.

This dissertation is written based on my three papers on Physical Review B [18, 19, 20]. The dissertation is organized as the follows: In Chapter 2, we employ simple isotropic exchange spin models to give an intuitive picture of how long-wavelength spin waves arise in a ferromagnet (FM) and antiferromagnet (AFM). In Chapter 3, we investigate the spin-wave excitations in van der Waals layered magnetic material $CoTiO_3$ and develop a quantitatively good description of all four spin-wave branches in this material using a formalism based on macroscopic variables. The established formalism can be easily extended to the magnetic system with a lattice deformation and is applicable to a generic quantum XY AFM. In Chapter 4, we utilize the macroscopic-variable spin-wave description introduced in Chapter 3 to study the antiferromagnetic (AFM) spin-wave dynamics under a spatially modulated strain. We demonstrate that the periodic strain acts like a magnonic crystal on spin waves propagating along the same direction of the modulation; and switching on the strain modulation leads to a *to-and-fro* motion of the spin waves that satisfy the *spatial* resonance condition. In Chapter 5, we focus on the spin-wave dynamics under a current-induced magnonic crystal, which has more tunability than the strain-modulated magnonic crystal. We discuss the possibility of using a tunable AC magnonic crystal for the purpose of spin-wave computing. Finally, in Chapter 6, we summarize the dissertation by presenting an overview of the work and outlining future directions for research. Appendices A, B, and C provide supplemental information to Chapters 3, 4, and 5, respectively.

2. EXCHANGE MODELS FOR SPIN WAVES*

In this chapter, we employ the exchange Hamiltonian to demonstrate how spin-wave excitations are formed in magnetically ordered systems such as FMs and AFMs.

2.1 Spin Wave in Ferromagnet

Spin-wave excitation in a FM can arise from various kinds of interactions, e.g., the long-range magnetic dipole-dipole interactions and the short-range exchange couplings [21]. For readers who are interested in a full treatment of spin waves that originating from the mixture of the dipole-dipole and exchange interactions, we refer to papers [22] and [23]. To illustrate the concept of shifted resonance, which will be introduced in later chapter, we restrict ourselves to the spin waves purely originating from the short-range exchange couplings. This is sufficient for demonstrating the idea. To be concrete, we study the isotropic Heisenberg's spin Hamiltonian

$$H^{FM} = -J \sum_{(i,j)} \boldsymbol{S}_i(t) \cdot \boldsymbol{S}_j(t). \tag{2.1}$$

Here, $J > 0$ is the FM exchange coupling between the spin $\boldsymbol{S}_i(t)$ on the lattice site i and the spin $\boldsymbol{S}_j(t)$ on its nearest neighbors. The summation (i, j) runs over all pairs of the nearest-neighboring sites. Using the Heisenberg equation of motion $\dot{\boldsymbol{S}}_i = \frac{1}{i}[\boldsymbol{S}_i, H^{FM}]$, one gets

$$\begin{aligned}
\frac{dS_i^x}{dt} =& J \sum_{\delta} (S_i^y S_{i+\delta}^z - S_i^z S_{i+\delta}^y), \\
\frac{dS_i^y}{dt} =& J \sum_{\delta} (S_i^z S_{i+\delta}^x - S_i^x S_{i+\delta}^z), \\
\frac{dS_i^z}{dt} =& J \sum_{\delta} (S_i^x S_{i+\delta}^y - S_i^y S_{i+\delta}^x).
\end{aligned} \tag{2.2}$$

---

*Part of this chapter is reprinted with permission from "Spin-wave dynamics controlled by tunable ac magnonic crystal" by Ankang Liu and Alexander M. Finkel'stein, 2023. Phys. Rev. B (to be published), Copyright 2023 by American Physical Society.

Here we dropped the argument t in $\boldsymbol{S}_i$ in Eq. (2.2) for simplicity of notation. In the case where all spins are located on a cubic lattice with the lattice constant a (as it is shown in Fig. 2.1), the summation of δ runs over $a(\pm1,0,0)$, $a(0,\pm1,0)$, and $a(0,0,\pm1)$.

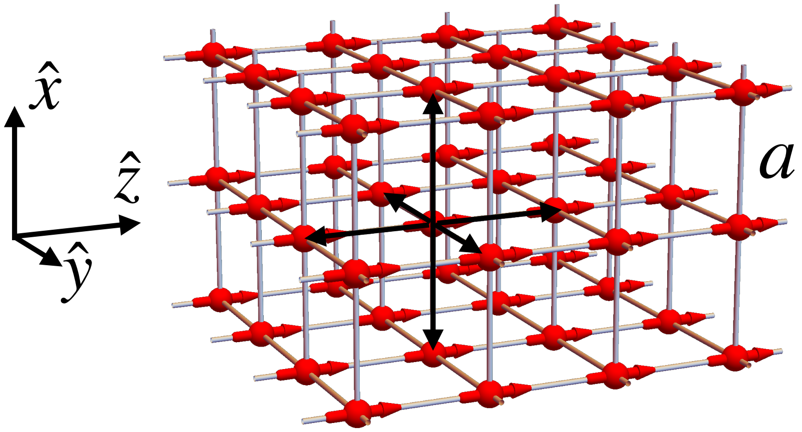

Figure 2.1: A schematic picture of FM cubic spin lattice with lattice constant a. Spins are indicated as red arrows on each site, and we assume that all spins are aligned along the z direction in the equilibrium.

Since only the dynamics of long-wavelength spin waves will be studied, in the continuum limit one can replace the spin operators $\boldsymbol{S}_i(t)$ by the continuous variable $\boldsymbol{S}(\boldsymbol{r},t)$ and expand its coordinate dependence, see e.g., Ref. [24]. $\boldsymbol{S}(\boldsymbol{r},t)$ is introduced here as a classical variable, which can be understood as the averaged spin over a small volume around the position $\boldsymbol{r}$. As an example, the term $\sum_\delta S_i^z S_{i+\delta}^y$ becomes

$$\begin{aligned} &S^z(\boldsymbol{r},t)\sum_\delta \left(S^y(\boldsymbol{r},t)+\frac{\partial S^y(\boldsymbol{r},t)}{\partial r^\alpha}\delta^\alpha+\frac{1}{2}\frac{\partial^2 S^y(\boldsymbol{r},t)}{\partial r^\alpha \partial r^\beta}\delta^\alpha\delta^\beta+\cdots\right)\approx \\ &6S^z(\boldsymbol{r},t)S^y(\boldsymbol{r},t)+a^2 S^z(\boldsymbol{r},t)\big(\nabla^2 S^y(\boldsymbol{r},t)\big). \end{aligned} \tag{2.3}$$

Here, the summations of α and β over x, y, and z are indicated explicitly. Eventually, the equations of motion (2.2) become

$$\frac{d\boldsymbol{S}}{dt} = (Ja^2)(\boldsymbol{S} \times \nabla^2 \boldsymbol{S}), \tag{2.4}$$

which is nothing else but the Landau–Lifshitz–Gilbert equation without the damping term (cf. Ref. [25]). We can assume, without loss of generality, that all spins are aligned along the z direction in the ground state. As a result, the spin variable $\boldsymbol{S}(\boldsymbol{r}, t)$ takes the form $(0, 0, S_0)$ in equilibrium, where S_0 is the saturated spin value. In the case of a spin-wave excitation, $\boldsymbol{S}(\boldsymbol{r}, t)$ deviates from the equilibrium value, and becomes $\boldsymbol{S}(\boldsymbol{r}, t) = \Big(S^x(\boldsymbol{r}, t), S^y(\boldsymbol{r}, t), \sqrt{S_0^2 - [S^x(\boldsymbol{r}, t)]^2 - [S^y(\boldsymbol{r}, t)]^2}\Big)$. In the weak-excitation limit $|S^{x,y}(\boldsymbol{r}, t)| \ll S_0$, we get a linearized equation in $S^{x,y}(\boldsymbol{r}, t)$:

$$\frac{dS^{\pm}}{dt} = \pm i J a^2 S_0 \nabla^2 S^{\pm}, \tag{2.5}$$

where $S^{\pm}(\boldsymbol{r}, t) \equiv S^x(\boldsymbol{r}, t) \pm i S^y(\boldsymbol{r}, t)$. It can be easily checked that this equation is solved by a plane wave $S^{\pm}(\boldsymbol{r}, t) = (\Delta S) e^{\pm i[\boldsymbol{k}\cdot\boldsymbol{r} - \omega_s(\boldsymbol{k})t + \varphi_s]}$ with $\omega_s(\boldsymbol{k}) = Ak^2$. Here ΔS is the amplitude of the spin wave, φ_s is the initial phase, and $A \equiv Ja^2 S_0$. Note that $\omega_s(\boldsymbol{k}) \to 0$ as $k \to 0$, which corresponds to the Goldstone gapless mode of the Heisenberg FM.

2.2 Spin Wave in Antiferromagnet

Now let us show how the spin-wave excitation looks like in an AFM. For simplicity, we study again the isotropic spin Hamiltonian

$$H^{AFM} = J \sum_{(i,j)} \boldsymbol{S}_i(t) \cdot \boldsymbol{S}_j(t), \tag{2.6}$$

where $J > 0$ and the summation (i, j) runs over all pairs of the nearest-neighboring sites on a cubic lattice as well. Note that the opposite sign in this spin Hamiltonian compared with the one of a FM (cf. Eq. (2.1)). Therefore, as it is schematically depicted in Fig. 2.2, all spins on the A sublattice are aligned oppositely to the spins on the B sublattice in the thermal equilibrium. This leads to a vanishing total magnetization for an AFM.

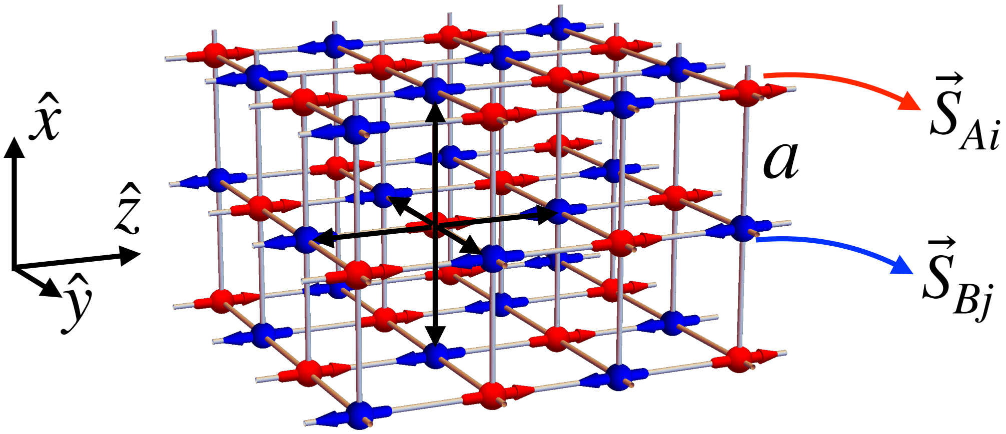

Figure 2.2: A schematic picture of AFM cubic spin lattice with lattice constant a. Spins on different sublattices are indicated as red and blue arrows on the corresponding sites. In the ground state, all spins on the A sublattice are aligned along the positive z direction while the ones on the B sublattice are along the negative z direction.

Following the same procedure in the last section, namely, calculating the commutation relations of $\boldsymbol{S}_i(t)$ and H^{AFM}, replacing the spin operators with the corresponding continuous variables in the continuum limit, and making the gradient expansions, we eventually get

$$\frac{d\boldsymbol{S}_A(\boldsymbol{r},t)}{dt} \approx -6J(\boldsymbol{S}_A \times \boldsymbol{S}_B) - (Ja^2)(\boldsymbol{S}_A \times \nabla^2 \boldsymbol{S}_B) \tag{2.7}$$

and

$$\frac{d\boldsymbol{S}_B(\boldsymbol{r},t)}{dt} \approx -6J(\boldsymbol{S}_B \times \boldsymbol{S}_A) - (Ja^2)(\boldsymbol{S}_B \times \nabla^2 \boldsymbol{S}_A) \tag{2.8}$$

for the spin dynamics on the A and B sublattices, respectively. To proceed, we introduce the total magnetization $\boldsymbol{m} \equiv \boldsymbol{S}_A + \boldsymbol{S}_B$ and the Néel vector $\boldsymbol{l} \equiv \boldsymbol{S}_A - \boldsymbol{S}_B$. Using Eqs. (2.7) and (2.8), one obtains

$$\frac{d\boldsymbol{m}}{dt} \approx \frac{Ja^2}{2}(\boldsymbol{l} \times \nabla^2 \boldsymbol{l}) \text{ and } \frac{d\boldsymbol{l}}{dt} \approx 6J(\boldsymbol{m} \times \boldsymbol{l}) \tag{2.9}$$

after neglecting the terms that do not contribute to the lowest-order spin-wave dynamics. Next, we apply the standard parametrization (see e.g., Refs. [26, 27, 28])

$$\begin{aligned}\boldsymbol{l} =& 2S_0\sqrt{1-\left(\frac{|\vec{m}|}{2S_0}\right)^2}\left(\cos\theta\cos\phi, \cos\theta\sin\phi, \sin\theta\right), \\ \boldsymbol{m} =& (-m_\theta\sin\theta\cos\phi - m_\phi\sin\phi, -m_\theta\sin\theta\sin\phi + m_\phi\cos\phi, m_\theta\cos\theta)\end{aligned} \tag{2.10}$$

to the total magnetization and Néel vector. Here, S_0 is the saturated spin value on both A- and B-sublattices. The parameters θ, m_θ, and m_ϕ have the equilibrium values $\theta^{(0)}=0$, $m_\theta^{(0)}=0$, and $m_\phi^{(0)}=0$, while $\phi^{(0)}$ can be an arbitrary angle. Note that, by the definitions, $\boldsymbol{m}\cdot\boldsymbol{l}=0$, and this orthogonality is automatically fulfilled by the parametrization (2.10).

Finally, we substitute the parametrization (2.10) into Eqs. (2.9), keep only the linear terms in the parameters that deviate from its equilibrium values, and get two decoupled pairs of linearized equations:

$$\begin{aligned}\dot{m_\theta} \approx& (2S_0)^2(\frac{Ja^2}{2})\nabla^2\phi, \\ \dot{\phi} \approx& 6Jm_\theta\end{aligned} \tag{2.11}$$

and

$$\begin{aligned}\dot{m_\phi} \approx& -(2S_0)^2(\frac{Ja^2}{2})\nabla^2\theta, \\ \dot{\theta} \approx& -6Jm_\phi.\end{aligned} \tag{2.12}$$

Both pairs of equation lead to the same spin-wave dispersion $\omega_s(\boldsymbol{k})=\sqrt{12}JS_0a|\boldsymbol{k}|$. In contrast to the quadratic dispersion in a FM, the AFM spin wave has a linear spectrum. It is worth pointing out that the degeneracy of two pairs will be lifted by an external magnetic field. In the presence of an external magnetic field $B_0\hat{z}$, the equilibrium value of m_θ becomes finite, which indicates that a net magnetization along z direction is induced by the external magnetic field. One can easily check that, in this case, the spin wave described by the pair (m_θ, ϕ) remains gapless, while the (m_ϕ, θ)-pair spin-wave branch acquires a nonzero energy gap which is $\propto B_0$. The gapless spin-wave branch (m_θ, ϕ) is associated with U(1) symmetry of the system, which is directly related to the spin-superfluidity transport [28, 29, 30].

At the end of this section, we demonstrate an unconventional way of deriving the AFM Lagrangian density. The standard route to find the the Lagrangian density requires going through the whole complicated process of constructing the path integral [27, 28]. Here we show that one can simply restore the Lagrangian density from the equations of motion (2.9), which avoids the mathematical complications of the path-integral formalism. In the continuum limit, the spin Hamiltonian (2.6) is approximated as

$$\begin{aligned} H^{AFM} \sim \int d^3\boldsymbol{r}\mathcal{H}^{AFM} &= \int d^3\boldsymbol{r} \left\{ 6J\boldsymbol{S}_A \cdot \boldsymbol{S}_B + \frac{Ja^2}{2} \left[\boldsymbol{S}_A \cdot (\nabla^2 \boldsymbol{S}_B) + \boldsymbol{S}_B \cdot (\nabla^2 \boldsymbol{S}_A) \right] \right\} \\ &\approx \int d^3\boldsymbol{r} \left[3J\boldsymbol{m}^2 + \frac{Ja^2}{4} \sum_\alpha (\partial_\alpha \boldsymbol{l})^2 \right]. \end{aligned} \tag{2.13}$$

In the above equation, the summation of α runs over all three spatial coordinates x, y, and z. The action, which describes the dynamics of the system, will generally take the form

$$A^{AFM} \propto \int d\tau d^3\boldsymbol{r}\mathcal{L}^{AFM} = \int d\tau d^3\boldsymbol{r} \left(\mathcal{L}_{gk}^{AFM} - \mathcal{H}^{AFM} \right). \tag{2.14}$$

Here $\mathcal{L}_{gk}^{AFM}$ is a *geometric kinetic* term, which appears in the process of constructing the path integral with the use of the spin coherent states technique. This term is also called the *Berry phase* of the spin history [27]. The equations of motion for $\boldsymbol{m}$ and $\boldsymbol{l}$ are obtained by minimizing the action A^{AFM}. By requiring $\delta A^{AFM}/\delta \boldsymbol{m} = 0$, one gets

$$\frac{\partial \mathcal{L}_{gk}^{AFM}}{\partial \boldsymbol{m}} - 6J\boldsymbol{m} = 0. \tag{2.15}$$

On the other hand, one has

$$\boldsymbol{l} \times \frac{d\boldsymbol{l}}{dt} \approx (2S_0)^2 6J\boldsymbol{m} \tag{2.16}$$

from the second equation in (2.9). Therefore, we find that $\mathcal{L}_{gk}^{AFM} = (2S_0)^{-2}\boldsymbol{m} \cdot (\boldsymbol{l} \times \partial_t \boldsymbol{l})$ and

$$\mathcal{L}^{AFM} = (2S_0)^{-2}\boldsymbol{m} \cdot (\boldsymbol{l} \times \partial_t \boldsymbol{l}) - 3J\boldsymbol{m}^2 - \frac{Ja^2}{4}\sum_{\alpha} (\partial_\alpha \boldsymbol{l})^2 . \tag{2.17}$$

One can easily check that, with the use of this Lagrangian density, $\delta A^{AFM}/\delta \boldsymbol{l} = 0$ gives the first equation in (2.9). In this way, the explicit expression of the Berry-phase term was found, and the AFM Lagrangian density could be restored without the need for constructing the path integral.

3. SPIN WAVES IN LAYERED ANTIFERROMAGNETS WITH HONEYCOMB STRUCTURE*

In this chapter we derive the equations of motion for the system of spins in a quantum XY AFM in terms of pairs of macroscopic quantities, which are the magnetization and the Néel vector densities. Compared to other classes, the XY AFMs are relatively limited in occurrence. Usually, they could be met in systems with a hexagonal symmetry of the crystalline lattice, see Ref. [31]. At the present moment, a number of materials has been confirmed to be the layered AFM with in-plane spins, including $NiPS_3$ [32], $CoPS_3$ [33], CuMnAs [34], $CrCl_3$ [35, 36, 37], etc. Here, for concreteness, we consider the XY-type layered $CoTiO_3$, although the approach is general and expected to be applicable to any layered AFM.

We arrive to a relatively simple description of quantum AFM in terms of the gradient expansion of the pairs of macroscopic variables that in the continuous limit reproduces the main features of the results obtained for $CoTiO_3$ in Ref. [38]. In particular, this method allows to describe accurately all four spin-wave modes existing in the discussed system. By comparing their spectrum calculated here using the macroscopic variables approach with the experimental data of Ref. [38], we extracted the values of the parameters in the spin Hamiltonian and confirm the XY character of the intralayer spin exchange in this material.

In a series of papers [39, 40, 41], the magnon backward scattering by a magnonic crystal was studied experimentally in FMs. The periodic scattering potential (i.e., the magnonic crystal) was created by a set of current carrying meander wires. The perspective of this experimental method for bulk AFM samples remains unclear. We, therefore, study here the effect of the lattice deformation on the spin dynamics. The deformations change distances between spins, and thus modify exchange coupling constants. The modulation of the coupling constants causes in its turn scattering of the spin waves. The description in terms of the macroscopic variables developed in

---

*Reprinted with permission from "Spin waves in layered antiferromagnets with honeycomb structure" by Ankang Liu and Alexander M. Finkel'stein, 2022. Phys. Rev. B, 105, 214409, Copyright 2022 by American Physical Society.

this chapter can be easily extended to a system with deformations, and allows one to obtain the dynamics of the scattering spin waves in the modulated crystal. This is another goal of this chapter.

3.1 Spin Dynamics in the Absence of Lattice Deformations

CoTiO$_3$ is a layered AFM material, and is a sort of a magnetic “ABC-stacked graphite".

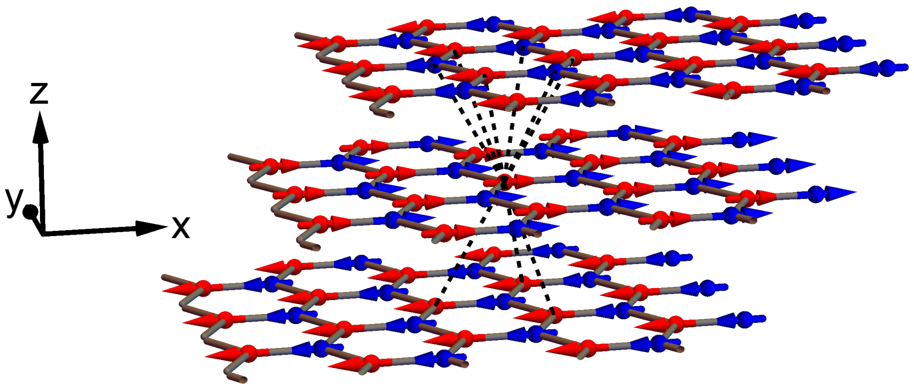

Figure 3.1: Schematic spin lattice structure of CoTiO$_3$. The period along the z direction comprises six layers including the ABC stacking and the alternating $\pm x$ spin ordering in the neighbor layers. The red and blue spheres represent atoms located on the A and B sublattices, respectively, while arrows indicate the direction of their spins. CoTiO$_3$ is an intralayer FM and simultaneously an interlayer AFM. The dashed lines display couplings of a selected atom in the middle layer to the nine next-nearest neighbors in the other two layers. Each of the red atoms on the A sublattice in the middle layer is coupled with six blue atoms in the top layer and three red atoms in the bottom layer. A blue atom on the B sublattice in the middle layer is coupled with three blue atoms in the top layer and six red atoms in the bottom layer.

Namely, in each of the layers, spins are arranged on a honeycomb lattice (xy plane), and different layers are ABC-stacked along the third direction (z axis). A schematic structure of the spin lattice is shown in Fig. 3.1. The exchange coupling $J_{\parallel}$ within a layer is FM, i.e., $J_{\parallel} < 0$, while the exchange coupling constant between layers is AFM, $J_{\perp} > 0$. Previous measurements (cf. Ref. [38], and see also the discussion in Section 3.4) found out that the Hamiltonian describing best the magnetic excitations in $\mathrm{CoTiO_3}$ is

$$H = \sum_{i,\delta_1} J_\parallel (S_i^x S_{i+\delta_1}^x + S_i^y S_{i+\delta_1}^y) + \sum_{i,\delta_2} J_\perp (S_i^x \bar{S}_{i+\delta_2}^x + S_i^y \bar{S}_{i+\delta_2}^y + S_i^z \bar{S}_{i+\delta_2}^z) + \{S^{x/y/z} \leftrightarrow \bar{S}^{x/y/z}\}. \tag{3.1}$$

Notations here are the same as in Ref. [38]; the index i runs over all sites of spin, while δ_1 and δ_2 run over the nearest neighbors within the same layer, and all the next-nearest neighbors between the layers. In the Hamiltonian (3.1) we have introduced $\boldsymbol{S}$ and $\bar{\boldsymbol{S}}$ that are the spin operators for the $\pm x$-ordered magnetic layers, respectively. Using the Heisenberg equations of motion, $\dot{\boldsymbol{S}} = \frac{1}{i}[\boldsymbol{S}, H]$, for each of the spin components of $\boldsymbol{S}_i$, we find

$$\begin{aligned}
\frac{dS_i^x}{dt} =& \sum_{\delta_1} J_\parallel S_i^z S_{i+\delta_1}^y + \sum_{\delta_2} J_\perp (S_i^z \bar{S}_{i+\delta_2}^y - S_i^y \bar{S}_{i+\delta_2}^z), \\
\frac{dS_i^y}{dt} =& -\sum_{\delta_1} J_\parallel S_i^z S_{i+\delta_1}^x + \sum_{\delta_2} J_\perp (-S_i^z \bar{S}_{i+\delta_2}^x + S_i^x \bar{S}_{i+\delta_2}^z), \\
\frac{dS_i^z}{dt} =& \sum_{\delta_1} J_\parallel (S_i^y S_{i+\delta_1}^x - S_i^x S_{i+\delta_1}^y) + \sum_{\delta_2} J_\perp (S_i^y \bar{S}_{i+\delta_2}^x - S_i^x \bar{S}_{i+\delta_2}^y).
\end{aligned} \tag{3.2}$$

The equations of motion for $\bar{\boldsymbol{S}}$ could be obtained by making the exchange: $\boldsymbol{S} \leftrightarrow \bar{\boldsymbol{S}}$. Although the period of the spin lattice along the z direction is six layers, there is no need in considering the dynamics of all six layers. Instead, one just needs to calculate the equations of motion for $\boldsymbol{S}$ and $\bar{\boldsymbol{S}}$, which are the spin operators of two oppositely ordered layers. Suppose we start from the bottom layer in Fig. 3.1 and move upward. Then each next layer requests for the same operation, i.e., change in the direction of the spin ordering along with a shift by one unit length along the $+x$ direction. Hence, each layer is in the same environment and does not feel the periodicity along the z direction.

Next, in order to get a continuum model, we make an expansion in $\boldsymbol{S}$ with respect to its coordinate dependence (cf. Chapter 2). As an example, let us take the term $\sum_{\delta_1} J_\parallel S_i^z S_{i+\delta_1}^y$ and assume that the site i is on the A sublattice. We are interested in finding the equation of motion for a spin located on this site. For this, we need to explore its environment. Performing the expansion, we obtain

$$\begin{aligned}\sum_{\delta_1} S_i^z S_{i+\delta_1}^y =& \sum_{\delta_1} S_{iA}^z (S_{iB}^y + \frac{\partial S_{iB}^y}{\partial r^\alpha}\delta_1^\alpha + \frac{1}{2}\frac{\partial^2 S_{iB}^y}{\partial r^\alpha \partial r^\beta}\delta_1^\alpha \delta_1^\beta + \cdots) \\ \approx& 3S_{iA}^z S_{iB}^y + \frac{3}{4} S_{iA}^z (\frac{\partial^2}{\partial x^2} + \frac{\partial^2}{\partial y^2}) S_{iB}^y . \end{aligned} \tag{3.3}$$

Here and further on, the subscription A/B stands for the A/B sublattices. There are three nearest neighbors for the honeycomb lattice, and $\boldsymbol{\delta}_1$ are taken to be $\boldsymbol{\delta}_{1,1} = (1,0,0)$, $\boldsymbol{\delta}_{1,2} = (-1/2, \sqrt{3}/2, 0)$, and $\boldsymbol{\delta}_{1,3} = (-1/2, -\sqrt{3}/2, 0)$. In Eq. (3.3) the summation over α and β is assumed, where $\alpha, \beta = x, y, z$ combines the three Cartesian components of the vector $\boldsymbol{\delta}_{1,j}$ with three coordinate derivatives. Note that for the convenience of the discussion, lengths are measured in the units of either intra- or inter-layer lattice constants.

Similarly, for a term describing the interlayer interaction, $\sum_{\delta_2} J_\perp S_i^z \bar{S}_{i+\delta_2}^y$, we have

$$\sum_{\delta_2} S_i^z \bar{S}_{i+\delta_2}^y \approx 3S_{iA}^z(\bar{S}_{iB}^y + 2\bar{S}_{iA}^y) + 3S_{iA}^z[\frac{\partial \bar{S}_{iB}^y}{\partial z} + \frac{1}{4}(\frac{\partial^2}{\partial x^2} + \frac{\partial^2}{\partial y^2} + 2\frac{\partial^2}{\partial z^2})(\bar{S}_{iB}^y + 2\bar{S}_{iA}^y)]. \tag{3.4}$$

Here we assumed that a site i is on one of the A sublattices (i.e., i is red), and that δ_2 runs over nine next-nearest neighbors as indicated by the dashed line in Fig. 3.1.

To derive the equations of motion for the macroscopic quantities, we substitute the leading expansion terms as shown in Eqs. (3.3) and (3.4) back into Eq. (3.2). The calculations are straightforward, and details are presented in Appendix A.1. Then, after making a transition from the site spin operators $\boldsymbol{S}_i(t)$ to the continuous variable $\boldsymbol{S}(\boldsymbol{r}, t)$, we introduce the macroscopic quantities for each of the two sub-lattices: the total magnetization $\boldsymbol{m}_{A/B}(\boldsymbol{r}, t) \equiv \boldsymbol{S}_{A/B}(\boldsymbol{r}, t) + \bar{\boldsymbol{S}}_{A/B}(\boldsymbol{r}, t)$ and the Néel vector $\boldsymbol{l}_{A/B}(\boldsymbol{r}, t) \equiv \boldsymbol{S}_{A/B}(\boldsymbol{r}, t) - \bar{\boldsymbol{S}}_{A/B}(\boldsymbol{r}, t)$, which will be used for describing the long-wavelength spin wave excitation. Finally, for the two spin-wave branches with the lowest energy we implement the approximation $\boldsymbol{m}_A = \boldsymbol{m}_B = \boldsymbol{m}$ and $\boldsymbol{l}_A = \boldsymbol{l}_B = \boldsymbol{l}$, and as a result get:

$$\frac{dm^x}{dt} \approx \frac{3}{2} J_\parallel (l^z l^y) + \frac{9}{8} J_\perp (l^y \nabla_+^2 l^z), \tag{3.5}$$

$$\frac{dm^y}{dt} \approx -\frac{3}{2} J_\parallel (l^z l^x) - \frac{9}{8} J_\perp (l^x \nabla_+^2 l^z), \tag{3.6}$$

$$\frac{dm^z}{dt} \approx -\frac{3}{8} J_\parallel [\boldsymbol{l} \times (\nabla_-^2 \boldsymbol{l})]_z + \frac{9}{8} J_\perp [\boldsymbol{l} \times (\nabla_+^2 \boldsymbol{l})]_z, \tag{3.7}$$

$$\frac{dl^x}{dt} \approx (\frac{3}{2} J_\parallel - 9 J_\perp)(l^y m^z) - \frac{9}{8} J_\perp (l^y \nabla_+^2 m^z), \tag{3.8}$$

$$\frac{dl^y}{dt} \approx (-\frac{3}{2} J_\parallel + 9 J_\perp)(l^x m^z) + \frac{9}{8} J_\perp (l^x \nabla_+^2 m^z), \tag{3.9}$$

and

$$\frac{dl^z}{dt} \approx 9 J_\perp (\boldsymbol{m} \times \boldsymbol{l})_z - \frac{3}{8} J_\parallel [\boldsymbol{l} \times (\nabla_-^2 \boldsymbol{m})]_z - \frac{9}{8} J_\perp [\boldsymbol{l} \times (\nabla_+^2 \boldsymbol{m})]_z. \tag{3.10}$$

Here, the short notation $\nabla_\pm^2 \equiv \nabla^2 \pm \partial^2/\partial z^2$ has ben introduced; the indices x, y, z mark the x, y, and z component of the vectors, respectively. In the following, we drop the last terms in Eqs. (3.8) and (3.9), because they lead to the terms in dispersion, which are of higher order in k^2, while we are interested in ω^2 only up to the order $\sim \mathcal{O}(k^2)$.

To proceed further, we will apply the standard parametrization (2.10) to the vectors $\boldsymbol{m}$ and $\boldsymbol{l}$ by simply replacing S_0 there with $\tilde{S}$, which is the effective spin in this system. Note that, under this parametrization, the vectors $\boldsymbol{m}$ and $\boldsymbol{l}$ are automatically constrained by $\boldsymbol{m} \cdot \boldsymbol{l} = 0$ and, at the same time, the lengths of $\boldsymbol{S}$ and $\bar{\boldsymbol{S}}$ are taken to be a fixed value $\tilde{S}$. De facto, by the transition from spin operators to the classical variables $\boldsymbol{m}$ and $\boldsymbol{l}$, we have implemented the language of the nonlinear sigma model (NLSM) for the description of the AFM dynamics.

Keeping only the linear terms in Eqs. (3.5)-(3.10), we get two decoupled pairs of equations in terms of the variables as introduced in Eqs. (2.10):

$$\begin{aligned} \dot{m}_\theta &\approx (4\tilde{S}^2)(-\frac{3}{8}J_\parallel \nabla_-^2 \phi + \frac{9}{8}J_\perp \nabla_+^2 \phi), \\ \dot{\phi} &\approx (-\frac{3}{2}J_\parallel + 9J_\perp)m_\theta; \end{aligned} \tag{3.11}$$

and

$$\begin{aligned} \dot{m}_\phi &\approx (4\tilde{S}^2)(-\frac{3}{2}J_\parallel \theta - \frac{9}{8}J_\perp \nabla_+^2 \theta), \\ \dot{\theta} &\approx (-9J_\perp - \frac{3}{8}J_\parallel \nabla_-^2 - \frac{9}{8}J_\perp \nabla_+^2)m_\phi. \end{aligned} \tag{3.12}$$

Note that $\theta^{(0)} = 0$, $m_\theta^{(0)} = 0$, and $m_\phi^{(0)} = 0$ are the equilibrium values for these equations, while ϕ can be arbitrary, because this system has a rotational symmetry along the z direction. In fact the form of the equations (3.11) and (3.12) does not depend much on the microscopic details of the Hamiltonian (3.1) and is determined by the symmetry of the system. Only the numerical prefactors are specific to the model and are determined by the lattice structure.

By taking another time derivative in Eqs. (3.11) and (3.12) we obtain closed equations of the second order. For example, for m_θ and m_ϕ they look as follows

$$\begin{aligned} \ddot{m}_\theta \approx &(4\tilde{S}^2)[-\frac{3J_\parallel}{8}(-\frac{3J_\parallel}{2} + 9J_\perp)\nabla_-^2 + \frac{9J_\perp}{8}(-\frac{3J_\parallel}{2} + 9J_\perp)\nabla_+^2]m_\theta, \\ \ddot{m}_\phi \approx &(4\tilde{S}^2)[\frac{27}{2}J_\parallel J_\perp + \frac{9}{16}J_\parallel^2 \nabla_-^2 + \frac{9J_\perp}{8}(\frac{3J_\parallel}{2} + 9J_\perp)\nabla_+^2]m_\phi. \end{aligned} \tag{3.13}$$

These equations give eigen-frequencies of the two low-energy spin-wave branches

$$\begin{aligned} \omega_a \approx &(2\tilde{S})[(\frac{9}{16}J_\parallel^2 - \frac{81}{16}J_\parallel J_\perp + \frac{81}{8}J_\perp^2)(k_x^2 + k_y^2) + (-\frac{27}{8}J_\parallel J_\perp + \frac{81}{4}J_\perp^2)k_z^2]^{\frac{1}{2}}, \\ \omega_{sh} \approx &(2\tilde{S})[-\frac{27}{2}J_\parallel J_\perp + \frac{9}{16}J_\parallel^2(k_x^2 + k_y^2) + (\frac{81}{8}J_\perp^2 + \frac{27}{16}J_\parallel J_\perp)(k_x^2 + k_y^2 + 2k_z^2)]^{\frac{1}{2}}. \end{aligned} \tag{3.14}$$

Here, ω_a and ω_{sh} are the acousticlike and the opticlike branches of the spin waves, respectively. In fact, the two branches exactly repeat each other after *shifting* k_z on $\pm\pi$. (This is why we indicate the “fake" opticlike branch by “sh".)

It remains to obtain the two "true" opticlike branches with higher energies. Since the opticlike excitations are not related with the rotational symmetry along the z directions, we perturb the spins on A and B sublattices in the anti-phase manner: An ansatz $\boldsymbol{m}_{A/B} = \pm(\delta m^x \hat{x} + \delta m^y \hat{y} + \delta m^z \hat{z})$ and $\boldsymbol{l}_{A/B} = 2\tilde{S}\hat{x} \pm (\delta l^x \hat{x} + \delta l^y \hat{y} + \delta l^z \hat{z})$ is implemented for these eigenmodes. Here, $+$ and $-$ stand for A and B sublattices, respectively. Note that, without loss of generality, we take the equilibrium Néel vector to be along the x direction, $\boldsymbol{l}_0 = 2\tilde{S}\hat{x}$. As above, $\boldsymbol{m}_{A/B}$ and $\boldsymbol{l}_{A/B}$ are subject to the constraint $\boldsymbol{m}_{A/B} \cdot \boldsymbol{l}_{A/B} = 0$. Note that, to fulfill this constraint, one can implement for vectors $\boldsymbol{m}_{A/B}$ and $\boldsymbol{l}_{A/B}$ the standard parametrization (cf. Eqs. (2.10)):

$$\boldsymbol{l}_{A/B} = 2\tilde{S}\sqrt{1 - \left(\frac{|\boldsymbol{m}_{A/B}|}{2\tilde{S}}\right)^2}\Big(\cos\big(\theta_{A/B}\big)\cos\big(\phi_{A/B}\big), \cos\big(\theta_{A/B}\big)\sin\big(\phi_{A/B}\big), \sin\big(\theta_{A/B}\big)\Big) \quad (3.15)$$

and

$$\begin{aligned}\boldsymbol{m}_{A/B} =& \Big(-(m_\theta)_{A/B}\sin\big(\theta_{A/B}\big)\cos\big(\phi_{A/B}\big) - (m_\phi)_{A/B}\sin\big(\phi_{A/B}\big),\\ &-(m_\theta)_{A/B}\sin\big(\theta_{A/B}\big)\sin\big(\phi_{A/B}\big) + (m_\phi)_{A/B}\cos\big(\phi_{A/B}\big), (m_\theta)_{A/B}\cos\big(\theta_{A/B}\big)\Big). \quad (3.16)\end{aligned}$$

Here, $\theta_{A/B} = \pm\theta$, $\phi_{A/B} = \pm\phi$, $(m_\theta)_{A/B} = \pm m_\theta$, and $(m_\phi)_{A/B} = \pm m_\phi$. After linearization, we get $\delta l^x_{A/B} \approx 0$, $\delta l^y_{A/B} \approx \pm 2\tilde{S}\phi$, $\delta l^z_{A/B} \approx \pm 2\tilde{S}\theta$, $\delta m^x_{A/B} \approx 0$, $\delta m^y_{A/B} \approx \pm m_\phi$, and $\delta m^z_{A/B} \approx \pm m_\theta$, which are equivalent to the expansions used here. Expanding the magnetization density and Néel vector around the equilibrium, we get (more details can be found in Appendix A.1)

$$\frac{d\delta m^x}{dt} \approx 0, \quad (3.17)$$

$$\frac{d\delta m^y}{dt} \approx 2\tilde{S}[(-\frac{3}{2}J_\parallel + 3J_\perp) - \frac{3}{8}J_\perp\nabla_+^2]\delta l^z, \quad (3.18)$$

$$\frac{d\delta m^z}{dt} \approx 2\tilde{S}[(3J_\parallel - 3J_\perp) + \frac{3}{8}J_\parallel \nabla_-^2 + \frac{3}{8}J_\perp \nabla_+^2]\delta l^y, \tag{3.19}$$

$$\frac{d\delta l^x}{dt} \approx 0, \tag{3.20}$$

$$\frac{d\delta l^y}{dt} \approx 2\tilde{S}[(-\frac{3}{2}J_\parallel + 6J_\perp) + \frac{3}{8}J_\perp \nabla_+^2]\delta m^z, \tag{3.21}$$

and

$$\frac{d\delta l^z}{dt} \approx 2\tilde{S}[(3J_\parallel - 6J_\perp) + \frac{3}{8}J_\parallel \nabla_-^2 - \frac{3}{8}J_\perp \nabla_+^2]\delta m^y. \tag{3.22}$$

We, thus, get two pairs of equations: Eqs. (3.18) and (3.22) for the pair $(\delta m^y, \delta l^z)$, and Eqs. (3.19) and (3.21) for $(\delta m^z, \delta l^y)$. Consequently, these pairs of equations lead us to two opticlike modes

$$\begin{aligned}
\omega_{o1} \approx &(2\tilde{S})[\frac{9}{2}(J_\parallel - 2J_\perp)^2 - \frac{9}{16}J_\parallel(J_\parallel - 2J_\perp)(k_x^2 + k_y^2) - \frac{9}{16}J_\perp(J_\parallel - 2J_\perp)(k_x^2 + k_y^2 + 2k_z^2)]^{\frac{1}{2}}, \\
\omega_{o2} \approx &(2\tilde{S})[\frac{9}{2}(J_\parallel - J_\perp)(J_\parallel - 4J_\perp) - \frac{9}{16}J_\parallel(J_\parallel - 4J_\perp)(k_x^2 + k_y^2) \\
&+ \frac{9}{16}J_\perp(J_\parallel + 2J_\perp)(k_x^2 + k_y^2 + 2k_z^2)]^{\frac{1}{2}}.
\end{aligned} \tag{3.23}$$

The gradient terms in Eqs. (3.18), (3.22), and in (3.19), (3.21) determine the dispersion of the opticlike modes.

3.2 Holstein–Primakoff Approach

As a comparison, we introduce an 8×8 model using the Holstein–Primakoff transformation, which quantitatively describes the spectrum of the spin waves in $CoTiO_3$ with using the Hamiltonian given by Eq. (3.1).

3.2.1 The 8×8 model

For a layer, where the magnetization is ordered along x direction, we introduce the standard Holstein-Primakoff operators

$$\begin{aligned}
S^x_{A/B} &= \tilde{S} - (a^\dagger a)/(b^\dagger b), \\
S^+_{A/B} &\equiv S^y_{A/B} + iS^z_{A/B} = \sqrt{2\tilde{S} - (a^\dagger a/b^\dagger b)}(a/b), \\
S^-_{A/B} &\equiv S^y_{A/B} - iS^z_{A/B} = (a^\dagger/b^\dagger)\sqrt{2\tilde{S} - (a^\dagger a/b^\dagger b)}.
\end{aligned} \tag{3.24}$$

Here, the subscription A/B indicates the A/B sublattices and, similarly, $a^\dagger/b^\dagger$ and a/b are creation and annihilation operators of spin excitations on the A and B sublattices, respectively. In the discussed system, $\mathrm{CoTiO_3}$, the effective spin $\tilde{S} = 1/2$; see the discussion on this point in Ref. [38]. Finally, for the neighboring layer, where the magnetization is ordered along the $-x$ direction, we use operators marked with a bar. We have

$$\begin{aligned}
\bar{S}^x_{A/B} &= (\bar{a}^\dagger \bar{a}/\bar{b}^\dagger \bar{b}) - \tilde{S}, \\
\bar{S}^+_{A/B} &\equiv -\bar{S}^y_{A/B} + i\bar{S}^z_{A/B} = \sqrt{2\tilde{S} - (\bar{a}^\dagger \bar{a}/\bar{b}^\dagger \bar{b})}(\bar{a}/\bar{b}), \\
\bar{S}^-_{A/B} &\equiv -\bar{S}^y_{A/B} - i\bar{S}^z_{A/B} = (\bar{a}^\dagger/\bar{b}^\dagger)\sqrt{2\tilde{S} - (\bar{a}^\dagger \bar{a}/\bar{b}^\dagger \bar{b})}.
\end{aligned} \tag{3.25}$$

Keeping only the quadratic form in terms of the creation and annihilation operators, one obtains a Hamiltonian H_{SW} in the quasi-momentum $\boldsymbol{k}$ space which determines the spectrum of the spin waves. The Hamiltonian $H_{SW} = \tilde{S}\sum_k V_k^\dagger H_k V_k$ is determined as follows:

$$V_k = \{a_k, b_k, a^\dagger_{-k}, b^\dagger_{-k}, \bar{a}_k, \bar{b}_k, \bar{a}^\dagger_{-k}, \bar{b}^\dagger_{-k}\}^T \tag{3.26}$$

and

$$H_k = \begin{pmatrix} H_{1k} & H_{2k} \\ H_{2k} & H_{1k} \end{pmatrix}. \tag{3.27}$$

Here, H_{1k} and H_{2k} are 4×4 matrices

$$H_{1k} = \begin{pmatrix} A_k & B_k & 0 & B_k \\ B_k^* & A_k & B_k^* & 0 \\ 0 & B_k & A_k & B_k \\ B_k^* & 0 & B_k^* & A_k \end{pmatrix} \tag{3.28}$$

and

$$H_{2k} = \begin{pmatrix} 0 & 0 & C_k & F_k \\ 0 & 0 & F_k^* & C_k \\ C_k & F_k & 0 & 0 \\ F_k^* & C_k & 0 & 0 \end{pmatrix}. \tag{3.29}$$

The matrix elements here are $A_k = -3J_{\|} + 9J_{\perp}$, $B_k = \frac{1}{2}J_{\|}\gamma_k$, $C_k = -J_{\perp}(e^{-ik_z}\gamma_k + e^{ik_z}\gamma_k^*)$, and $F_k = -J_{\perp}e^{-ik_z}\gamma_k^*$. The factor γ_k is determined by summation over the nearest neighbors, i.e., for the honeycomb lattice $\gamma_k = \sum_{j=1,2,3} e^{i\boldsymbol{k}\cdot\boldsymbol{\delta}_{1,j}}$ with $\boldsymbol{\delta}_{1,1} = (1,0,0)$, $\boldsymbol{\delta}_{1,2} = (-1/2, \sqrt{3}/2, 0)$, and $\boldsymbol{\delta}_{1,3} = (-1/2, -\sqrt{3}/2, 0)$. In our discussions, we take both in-plane and out-of-plane lattice constants to be 1 for simplicity. In Ref. [38], the best estimates of $J_{\|}$ and $J_{\perp}$ which match quantitatively well with the experimental data are found to be $J_{\|} = -4.41$ meV and $J_{\perp} = 0.57$ meV. In the discussions below, we will use for the parameters $J_{\|}$ and $J_{\perp}$ these values.

In Section 3.4, we get the parameters of the Hamiltonian (3.1) by analyzing the experimental data from Ref. [38] using our macroscopic description developed above. The extracted values of parameters, which optimally fit the data, are very close to the ones presented in Ref. [38].

Note that, this 8×8 model gives 4 branches of the magnon spectrum. These 4 branches could be divided into 2 groups by the symmetry of the eigenstates. To find the spectrum of magnons, one needs to solve the eigenvalue problem $H_k \left|\psi\right\rangle = E_k S_3 \left|\psi\right\rangle$ with the diagonal matrix $S_3 = \text{diag}(1, 1, -1, -1, 1, 1, -1, -1)$. The eigen vector $\left|\psi\right\rangle$ here is an eight-dimensional vector constructed in the basis V_k, see Eq. (3.26). It could be written as $\left|\psi\right\rangle = \{\psi_1^T, \psi_2^T\}^T$, where ψ_1 and ψ_2 are four-dimensional vectors within the subspaces $\{a_k, b_k, a_{-k}^\dagger, b_{-k}^\dagger\}^T$ and $\{\bar{a}_k, \bar{b}_k, \bar{a}_{-k}^\dagger, \bar{b}_{-k}^\dagger\}^T$, respectively. For one group of the eigenstates, which has the property $\psi_1 = \psi_2$, the eigenvalue equation becomes $(H_{1k} + H_{2k})\psi_1 = E_k \sigma_3 \psi_1$, where the diagonal $\sigma_3 = \text{diag}(1, 1, -1, -1)$ is a 4×4 matrix. For another group of the eigenstates with the property $\psi_1 = -\psi_2$, the eigenvalue equation reduces to $(H_{1k} - H_{2k})\psi_1 = E_k \sigma_3 \psi_1$. The effective 4×4 Hamiltonian $H_{1k} + H_{2k}$ coincides with Eqs. (6) and (7) in the Supplemental Material of Ref. [38]. Each of the reduced 4×4 Hamiltonians, $H_{1k} \pm H_{2k}$, describes two branches of the spin waves.

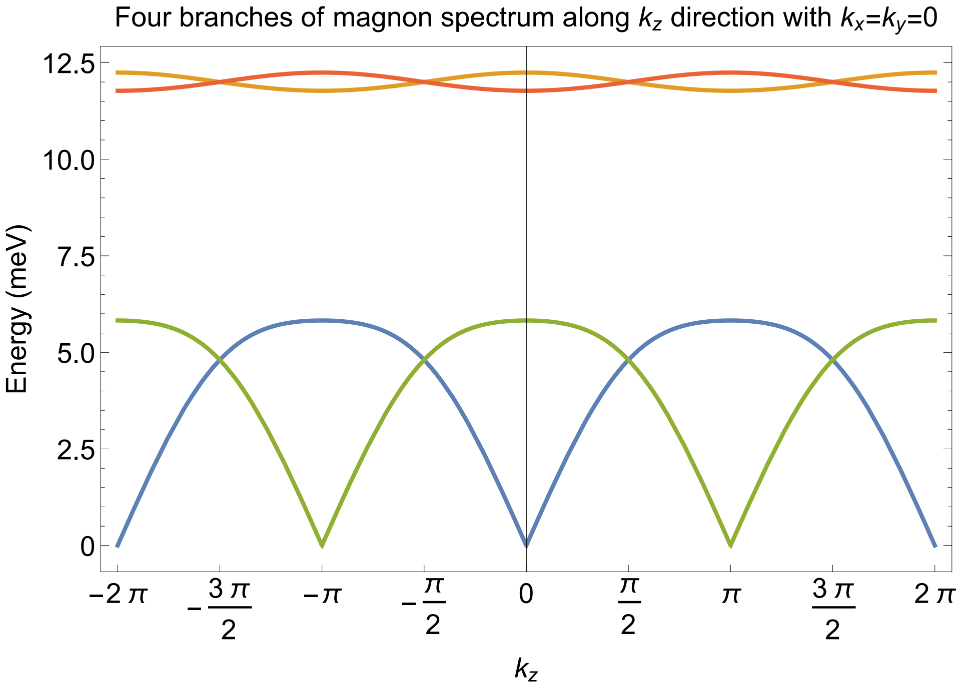

Figure 3.2: Four branches of the magnon spectrum obtained by solving the equations $(H_{1k} \pm H_{2k})\psi_1 = E_k \sigma_3 \psi_1$ with $J_\parallel = -4.41$ meV and $J_\perp = 0.57$ meV. The eigenvalues are plotted along the k_z direction with $k_x = k_y = 0$.

We plot in Fig. 3.2 the whole magnon spectrum consisting of four branches. The blue and orange curves are derived from $(H_{1k}+H_{2k})\psi_1 = E_k\sigma_3\psi_1$, while green and red ones correspond to $(H_{1k}-H_{2k})\psi_1 = E_k\sigma_3\psi_1$. Actually, these two pairs of branches are connected through π shifting along the k_z direction. This reveals the additional symmetry $\psi_1 = \pm\psi_2$ possessed by a spin system with the layered structure of CoTiO$_3$.

One of the four branches, the blue curve, touches zero at $\boldsymbol{k} = 0$. This acousticlike branch corresponds to the Goldstone mode. It is a direct consequence of the continuous symmetry with respect to rotation of the Néel vector $\boldsymbol{l}$ in the xy plane. The other branch (the green curve) after shifting k_z by π reproduces the Goldstone mode.

3.2.2 The eigenstates and eigenfrequencies

In principle, the magnon spectrum as well as its eigenstates can be found by solving the eigenvalue equations $(H_{1k} \pm H_{2k})\psi_1 = E_k^{(\pm)}\sigma_3\psi_1$. However, it is very intractable, and therefore we present an approximation here which allows us to describe the eigenstates and eigenfrequencies in a simplified but still comprehensive way. As an example, we demonstrate how it works for $H^+ \equiv H_{1k} + H_{2k}$. Under the basis of the subspace $\{a_k, a_{-k}^\dagger, b_k, b_{-k}^\dagger\}^T$, H^+ becomes

$$H^+ = \begin{pmatrix} A_k & C_k & B_k & G_k^+ \\ C_k & A_k & G_k^+ & B_k \\ B_k^* & (G_k^+)^* & A_k & C_k \\ (G_k^+)^* & B_k^* & C_k & A_k \end{pmatrix} \tag{3.30}$$

with $G_k^+ \equiv B_k + F_k$. Since the A and B sublattices are equivalent, we are looking for the eigenstate in the form

$$\tilde{\psi}_1 = a \begin{pmatrix} e^{i\chi_a} \\ 1 \\ e^{i\chi_{b_1}} \\ e^{i\chi_{b_2}} \end{pmatrix} + \frac{1}{8a} \begin{pmatrix} e^{i\chi_a} \\ -1 \\ e^{i\chi_{b_1}} \\ -e^{i\chi_{b_2}} \end{pmatrix}. \tag{3.31}$$

Here, a, χ_a, χ_{b_1}, and χ_{b_2} are functions of the wave-vector $\boldsymbol{k}$ that need to be evaluated. The magnitudes of the $\tilde{\psi}$-components are all determined by the parameter a, and are equal to $a \pm \frac{1}{8a}$. Note that $\tilde{\psi}_1$ satisfies the standard normalization condition $\tilde{\psi}_1^\dagger \tilde{\sigma}_3 \tilde{\psi}_1 = 1$, where $\tilde{\sigma}_3 = \mathrm{diag}(1, -1, 1, -1)$. Eq. (3.31) states that the dynamics of spins on the B sublattice is the same as the one on the A sublattice, except for the phase difference.

Expanding χ_a, χ_{b_1}, and χ_{b_2} around 0 (see Appendix A.2), we get the approximate solution of the equation $H^+\tilde{\psi}_1 = E\tilde{\sigma}_3\tilde{\psi}_1$:

$$\begin{aligned} E \approx& \sqrt{[A_k + \mathrm{Re}(B_k) + C_k + \mathrm{Re}(G_k^+)][A_k + \mathrm{Re}(B_k) - C_k - \mathrm{Re}(G_k^+)]}, \\ a \approx& \frac{1}{2\sqrt{2}} \Big(\frac{A_k + \mathrm{Re}(B_k) - C_k - \mathrm{Re}(G_k^+)}{A_k + \mathrm{Re}(B_k) + C_k + \mathrm{Re}(G_k^+)} \Big)^{\frac{1}{4}}, \end{aligned} \tag{3.32}$$

and

$$\begin{aligned} \chi_a \approx& - \Big\{ 16a^2[\mathrm{Im}(G_k^+)\,\mathrm{Re}(B_k) - \mathrm{Im}(B_k) Re G_k^+] \Big\} \times \Big\{ \mathrm{Re}(B_k)[(64a^4 - 1)\,\mathrm{Re}(B_k) \\ &+ (64a^4 + 1)\,\mathrm{Re}(G_k^+)] + C_k[(64a^4 + 1)\,\mathrm{Re}(B_k) + (64a^4 - 1)\,\mathrm{Re}(G_k^+)] \Big\}^{-1}, \\ \chi_{b_1} \approx& - \Big\{ \mathrm{Re}(B_k)[(64a^4 - 1)\,\mathrm{Im}(B_k) + (64a^4 + 1)\,\mathrm{Im}(G_k^+)] + C_k[(64a^4 + 1)\,\mathrm{Im}(B_k) \\ &+ (64a^4 - 1)\,\mathrm{Im}(G_k^+)] \Big\} \times \Big\{ \mathrm{Re}(B_k)[(64a^4 - 1)\,\mathrm{Re}(B_k) + (64a^4 + 1)\,\mathrm{Re}(G_k^+)] \\ &+ C_k[(64a^4 + 1)\,\mathrm{Re}(B_k) + (64a^4 - 1)\,\mathrm{Re}(G_k^+)] \Big\}^{-1}, \\ \chi_{b_2} =& \chi_a + \chi_{b_1} \end{aligned} \tag{3.33}$$

where $\mathrm{Re}(\cdots)$ and $\mathrm{Im}(\cdots)$ denote the real and imaginary part of "$\cdots$", respectively. The solution presented by Eq. (3.33) indicates the smallness of the phases, which is consistent with the expansion in phases χ_a, χ_{b_1}, and χ_{b_2} performed after Eq. (3.31).

As for the higher energy state, we use the same ansatz and repeat the above procedures, but expand χ_a and χ_{b_2} around π. Eventually we get the results similar to Eqs. (3.32) and (3.33) but with the following changes: (i) $B_k \to -B_k$; (ii) $C_k \to -C_k$; and finally (iii) phase π has to be added to χ_a and χ_{b_2}.

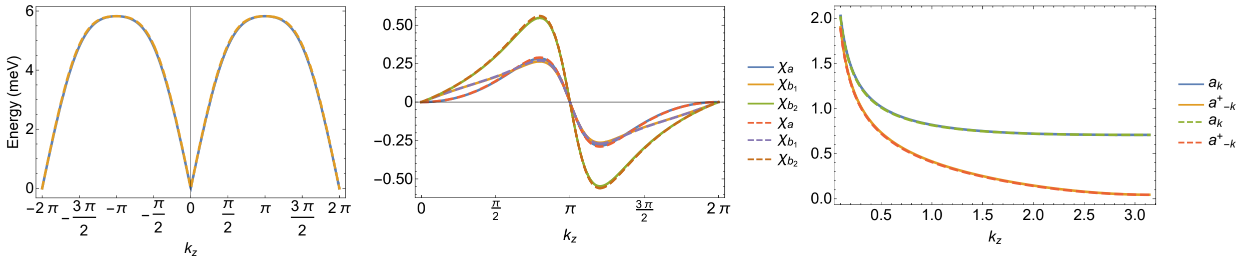

(a) Spectrum of the acousticlike branch

(b) Component phases of the acousticlike magnon state

(c) Amplitudes on each component of the acousticlike magnon state

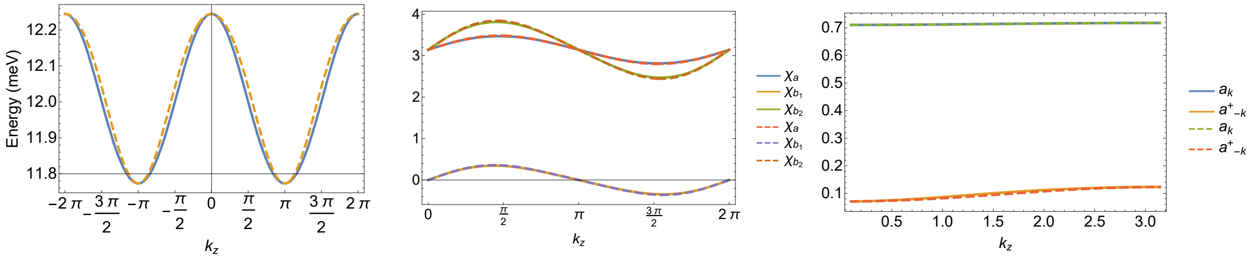

(d) Spectrum of the opticlike branch

(e) Component phases of the opticlike magnon state

(f) Amplitudes on each component of the opticlike magnon state

Figure 3.3: The acousticlike (first row) and opticlike (second row) branches of the magnon spectrum found by the Holstein-Primakoff method. Plot (a) and (d) give the spectrum; (b) and (e) are phases, while (c) and (f) are magnitudes of each of the components. Here, we plotted the dependence on k_z with $k_x = k_y = 0$. The solid curves represent the exact solutions for the eigenvalue equations$(H_{1k} + H_{2k})\psi_1 = E_k \sigma_3 \psi_1$, while the dashed curves stand for the approximated solutions Eqs. (3.32) and (3.33).

In Fig. 3.3, we compare the results obtained for the acousticlike and opticlike branches of the magnon spectrum by solving the eigenvalue equation exactly, and using the approximate equations (3.32) and (3.33). In all six plots, the dashed curves (approximate) almost match the solid ones (exact). Hence, the approximate Eqs. (3.32) and (3.33) work perfectly.

3.3 Results and Discussion

Let us compare the results of the Holstein-Primakoff approach with those obtained using the magnetization and Néel vector densities. To give a general picture, in Fig. 3.4, we plot four branches of the magnon spectrum given by two methods. As it is shown, each pair of two branches obtained through two different approaches is approximately matching with each other at small k_z.

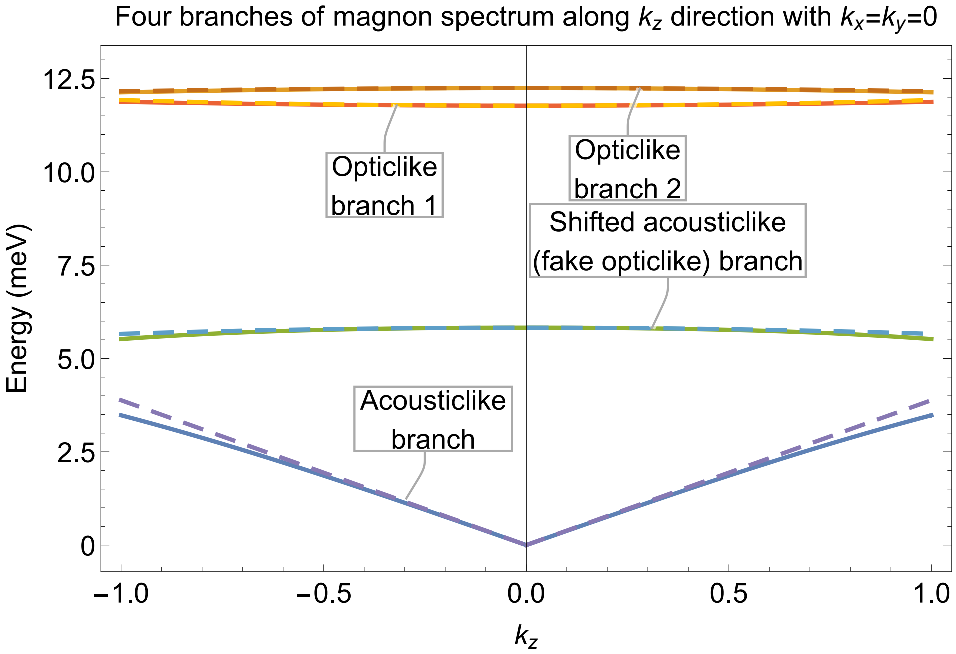

Figure 3.4: Four branches of the magnon spectrum obtained by the Holstein-Primakoff approach (solid curves) and macroscopic description (dashed curves). The eigenvalues are plotted along the k_z direction with $k_x = k_y = 0$.

3.3.1 Comparison of different methods

We now compare, in detail, the results of our description in terms of the macroscopic variables with those obtained from the exact solution of the 8×8 model. In Figs. 3.5, we plot the dispersion of the acousticlike and opticlike modes along the k_z and k_x directions. To quantitatively compare the results obtained by these two very different approaches, we estimate the spin wave velocities of the acousticlike branch along the x and z directions; see Figs. 3.5(a) and 3.5(e). We find $\partial\omega_a(\boldsymbol{k})/\partial k_z|_{\boldsymbol{k}=0} \approx 3.81$ for the 8×8 model and $\partial\omega_a(\boldsymbol{k})/\partial k_z|_{\boldsymbol{k}=0} \approx 3.88$ for our proposed macroscopic description. The mismatch is less than 2%. Along x direction, we get an even better agreement with $\partial\omega_a(\boldsymbol{k})/\partial k_x|_{\boldsymbol{k}=0}$ estimated to be 5.19 for both models. Consequently, we conclude that our macroscopic description of the acousticlike magnon branch agrees quantitatively well with the exact spectrum under the long wavelength limit, i.e., $k \lesssim 0.5$.

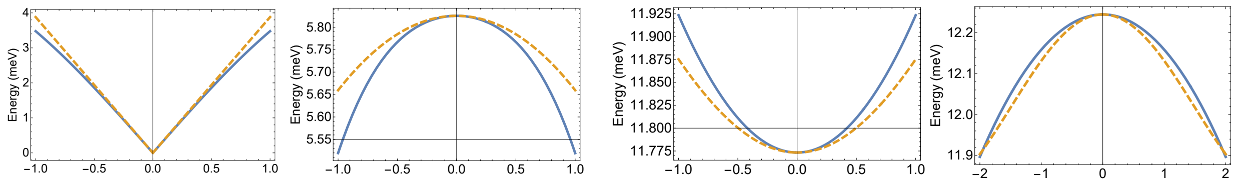

(a) Acousticlike branch along k_z direction

(b) Shifted acousticlike branch along k_z direction

(c) Opticlike branch 1 along k_z direction

(d) Opticlike branch 2 along k_z direction

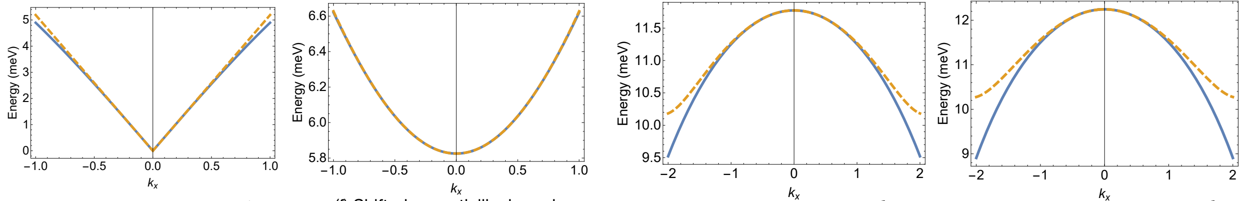

(e) Acousticlike branch along k_x direction

(f) Shifted acousticlike branch along k_x direction

(g) Opticlike branch 1 along k_x direction

(h) Opticlike branch 2 along k_x direction

Figure 3.5: The fragments of the spectrum of the acousticlike, shifted and two opticlike magnon modes. The first raw presents the spectrum along the k_z direction, while the second row gives the k_x direction. (a) and (e) are acousticlike branch; (b) and (f) are the fragments of the shifted acousticlike branch, while (c), (g), and (d), (h) are related to the opticlike branches 1, and 2, respectively. In each subfigure, the solid curve represents the exact solutions for the eigenvalue equations $(H_{1k} \pm H_{2k})\psi_1 = E_k\sigma_3\psi_1$, while the dashed curve is described by the semimacroscopic equations (3.14) and (3.23).

For completeness, we also compare the results obtained for other three branches of the spin waves (see Fig. 3.4). For the shifted acousticlike and two opticlike branches, using the Holstein-Primakoff method, we obtain for the k_z direction $\partial^2\omega_{sh}(\boldsymbol{k})/\partial^2 k_z|_{\boldsymbol{k}=0} \approx -0.41$, $\partial^2\omega_{o1}(\boldsymbol{k})/\partial^2 k_z|_{\boldsymbol{k}=0} \approx 0.22$, and $\partial^2\omega_{o2}(\boldsymbol{k})/\partial^2 k_z|_{\boldsymbol{k}=0} \approx -0.24$ (see Figs. 3.5(b), 3.5(c), and 3.5(d)). At the same time, our semimacroscopic approach yields, $\partial^2\omega_{sh}(\boldsymbol{k})/\partial^2 k_z|_{\boldsymbol{k}=0} \approx -0.33$, $\partial^2\omega_{o1}(\boldsymbol{k})/\partial^2 k_z|_{\boldsymbol{k}=0} \approx 0.30$, and $\partial^2\omega_{o2}(\boldsymbol{k})/\partial^2 k_z|_{\boldsymbol{k}=0} \approx -0.17$. On the contrary, for the k_x direction (cf. Figs. 3.5(f), 3.5(g), and 3.5(h)), both methods give the same estimates $\partial^2\omega_{sh}(\boldsymbol{k})/\partial^2 k_x|_{\boldsymbol{k}=0} \approx 1.71$, $\partial^2\omega_{o1}(\boldsymbol{k})/\partial^2 k_x|_{\boldsymbol{k}=0} \approx -1.02$, and $\partial^2\omega_{o2}(\boldsymbol{k})/\partial^2 k_x|_{\boldsymbol{k}=0} \approx -1.44$. Although there is a relatively large mismatch between the two approaches for the k_z direction, the dispersion within (k_x, k_y) momentum plane is well captured by our semimacroscopical scheme. We ascribe the discrepancy in the magnon spectrum along the k_z direction to the neglecting of $\pm\partial/\partial z$-terms in Eqs. (A.4)-(A.9) when deriving the macroscopic equations of motion, see Appendix A.1 for the details.

3.3.2 Dynamics of four branches in terms of the macroscopic variables

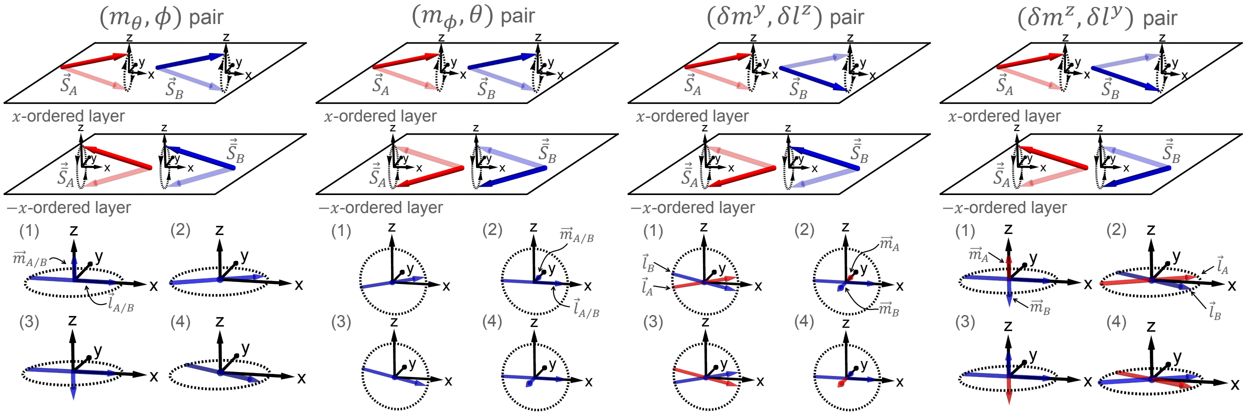

(a) Dynamics of (m_θ, ϕ) pair around $k = 0$

(b) Dynamics of (m_ϕ, θ) pair around $k = 0$

(c) Dynamics of $(\delta m^y, \delta l^z)$ pair around $k = 0$

(d) Dynamics of $(\delta m^z, \delta l^y)$ pair around $k = 0$

Figure 3.6: Dynamics of the four spin wave excitations in terms of the macroscopic pairs: (a) (m_θ, ϕ); (b) (m_ϕ, θ); (c) $(\delta m^y, \delta l^z)$, and (d) $(\delta m^z, \delta l^y)$ at $\boldsymbol{k} \approx 0$. Spin vectors, magnetization densities, and Néel vectors on the A and B sublattices are indicated by red and blue colors, respectively. In the lower part of each subfigure, (1), (2), (3), and (4) illustrate the magnitudes and directions of $\boldsymbol{m}_{A/B}$ and $\boldsymbol{l}_{A/B}$ at $t = 0$, $T/4$, $T/2$, and $3T/4$, respectively; T is the period of the spin wave.

In this section, to have a better understanding of the four spin-wave branches shown in Fig. 3.4, we give the schematic pictures of their spin dynamics. We start with the acousticlike magnon branch, i.e., the (m_θ, ϕ) pair. As it is shown in Fig. 3.6(a), spins on A and B sublattices are fully synchronized. The magnetization densities $\boldsymbol{m}_{A/B}$ alternate along the z direction, while the Néel vectors $\boldsymbol{l}_{A/B}$ rotate back and forth around the equilibrium position within the xy plane. The magnon frequency of this mode goes to zero as $k \to 0$, because of the rotational symmetry. Generally, this mode manifests the possibility of the spin superfluidity in a system with XY symmetry, see e.g., Refs. [28] and [30]. In contrast to the acousticlike branch, the other branch described by the (m_ϕ, θ) pair is looking like an opticlike branch due to its finite energy at $k = 0$ but, in fact, is the *shifted* version of the acousticlike branch. This mode has the same dynamics on both A and B sublattices. It exhibits alternating $\boldsymbol{m}_{A/B}$ along the y direction and rotating $\boldsymbol{l}_{A/B}$ within the xz plane. Because of absence of the rotational symmetry around the y direction, this mode gets a finite energy at $k = 0$. Note, however, that at $k_z = \pi$, the phase difference between two neighboring layers will interchange the picture of spin dynamics presented in Figs. 3.6(a) and 3.6(b). At $k_z = \pi$, the discussed branch (looking like the optic one) touches zero, while the acousticlike magnon acquires the finite frequency. This is the reason why we named this branch as the “shifted acousticlike"; see Fig. 3.2.

The dynamics of the other two (true) opticlike branches with finite energies along the whole spectrum are depicted in Figs. 3.6(c) and 3.6(d). The opticlike branch 1 is similar to the shifted acousticlike branch with $\boldsymbol{m}_{A/B}$ alternating along the y direction and $\boldsymbol{l}_{A/B}$ rotating within the xz plane. The decisive point here is that spins on A and B sublattices change oppositely. Finally, the opticlike branch 2 is a gapped analogue of acousticlike branch: it has out-of-layer magnetization densities and in-layer Néel vectors. However, spins on sites A and B evolve oppositely which makes this mode to be opticlike.

In the next section, we evaluated the parameters of the Hamiltonian (3.1) using results obtained here for the four spin-wave modes.

3.4 The XY Model Versus the XXZ Model

In this section, we justify the Hamiltonian (3.1), i.e., the XY-type intralayer exchange coupling of this model, by exploiting our macroscopic description and comparing it with the experimental data extracted from Ref. [38]. To do it, we first consider a general spin Hamiltonian of the type XXZ, i.e.,

$$\begin{aligned} H =& \sum_{i,\delta_1} J_{\parallel}(S_i^x S_{i+\delta_1}^x + S_i^y S_{i+\delta_1}^y + \zeta S_i^z S_{i+\delta_1}^z) + \sum_{i,\delta_2} J_{\perp}(S_i^x \bar{S}_{i+\delta_2}^x + S_i^y \bar{S}_{i+\delta_2}^y + \eta S_i^z \bar{S}_{i+\delta_2}^z) \\ &+ \{S^{x/y/z} \leftrightarrow \bar{S}^{x/y/z}\} \end{aligned} \tag{3.34}$$

where ζ and η characterize the anisotropy in the intra- and inter-layer couplings, respectively. Note that, $\zeta = 0$ and $\eta = 1$ leads to the XY model we used in this chapter. By following the same steps of deriving the equations of motion for the macroscopic variables as in Appendix A.1, we get

$$\begin{aligned} \dot{m}_\theta &\approx (4\tilde{S}^2)\left(-\frac{3}{8}J_{\parallel}\nabla_-^2 + \frac{9}{8}J_{\perp}\nabla_+^2\right)\phi, \\ \dot{\phi} &\approx \left(-\frac{3(1-\zeta)}{2}J_{\parallel} + \frac{9(1+\eta)}{2}J_{\perp}\right)m_\theta; \end{aligned} \tag{3.35}$$

and

$$\begin{aligned} \dot{m}_\phi &\approx (4\tilde{S}^2)\left(-\frac{3(1-\zeta)}{2}J_{\parallel} + \frac{9(1-\eta)}{2}J_{\perp} + \frac{3\zeta}{8}J_{\parallel}\nabla_-^2 - \frac{9\eta}{8}J_{\perp}\nabla_+^2\right)\theta, \\ \dot{\theta} &\approx \left(-9J_{\perp} - \frac{3}{8}J_{\parallel}\nabla_-^2 - \frac{9}{8}J_{\perp}\nabla_+^2\right)m_\phi. \end{aligned} \tag{3.36}$$

for the two lowest spin-wave branches. As for the pairs $(\delta m^y, \delta l^z)$ and $(\delta m^z, \delta l^y)$ which describe other two opticlike branches, we find:

$$\begin{aligned} \frac{d\delta m^y}{dt} \approx& (2\tilde{S})\left(-\frac{3(1+\zeta)}{2}J_{\parallel} + \frac{3(3-\eta)}{2}J_{\perp} - \frac{3\zeta}{8}J_{\parallel}\nabla_-^2 - \frac{3\eta}{8}J_{\perp}\nabla_+^2\right)\delta l^z, \\ \frac{d\delta l^z}{dt} \approx& (2\tilde{S})\left(3J_{\parallel} - 6J_{\perp} + \frac{3}{8}J_{\parallel}\nabla_-^2 - \frac{3}{8}J_{\perp}\nabla_+^2\right)\delta m^y; \end{aligned} \tag{3.37}$$

and

$$
\begin{aligned}
\frac{d\delta m^z}{dt} \approx& (2\tilde{S})\left(3J_{\parallel} - 3J_{\perp} + \frac{3}{8}J_{\parallel}\nabla_{-}^2 + \frac{3}{8}J_{\perp}\nabla_{+}^2\right)\delta l^y, \\
\frac{d\delta l^y}{dt} \approx& (2\tilde{S})\left(-\frac{3(1+\zeta)}{2}J_{\parallel} + \frac{3(3+\eta)}{2}J_{\perp} - \frac{3\zeta}{8}J_{\parallel}\nabla_{-}^2 + \frac{3\eta}{8}J_{\perp}\nabla_{+}^2\right)\delta m^z,
\end{aligned}
\tag{3.38}
$$

As the result, using Eqs. (3.35)-(3.38), we obtain

$$
\begin{aligned}
v_{ax} &\equiv \frac{\partial \omega_a}{\partial |k_x|}\bigg|_{\boldsymbol{k}\to 0} = \left(\frac{3\tilde{S}}{2}\right)\sqrt{\left(-(1-\zeta)J_{\parallel} + 3(1+\eta)J_{\perp}\right)\left(-J_{\parallel} + 3J_{\perp}\right)}, \\
v_{az} &\equiv \frac{\partial \omega_a}{\partial |k_z|}\bigg|_{\boldsymbol{k}\to 0} = \left(\frac{3\sqrt{6}\tilde{S}}{2}\right)\sqrt{\left(-(1-\zeta)J_{\parallel} + 3(1+\eta)J_{\perp}\right)J_{\perp}}, \\
\omega_{sh}(\boldsymbol{k}\to 0) &= (3\sqrt{6}\tilde{S})\sqrt{\left(-(1-\zeta)J_{\parallel} + 3(1-\eta)J_{\perp}\right)J_{\perp}}, \\
\omega_{o1}(\boldsymbol{k}\to 0) &= (3\sqrt{2}\tilde{S})\sqrt{\left(-(1+\zeta)J_{\parallel} + (3-\eta)J_{\perp}\right)\left(-J_{\parallel} + 2J_{\perp}\right)}, \\
\omega_{o2}(\boldsymbol{k}\to 0) &= (3\sqrt{2}\tilde{S})\sqrt{\left(-(1+\zeta)J_{\parallel} + (3+\eta)J_{\perp}\right)\left(-J_{\parallel} + J_{\perp}\right)}.
\end{aligned}
\tag{3.39}
$$

We take the effective spin $\tilde{S} = 1/2$ in Eq. (3.39) and adjust the parameters $J_{\parallel}$, $J_{\perp}$, ζ, and η to fit the measurement in Ref. [38]. From Figs. 3(a) and 3(e) in Ref. [38], we estimate $[\omega_{o1}(\boldsymbol{k}\to 0) + \omega_{o2}(\boldsymbol{k}\to 0)]/2 \approx 11.9$ meV, $v_{ax} \approx 5.1$ meV, $\omega_{sh}(\boldsymbol{k}\to 0) \approx 5.8$ meV, and $v_{az} \approx 3.9$ meV (here, the units of spin-wave velocity are indicated in meV, because we use for momenta dimensionless units). By fitting these data using Eqs. (3.39), an optimal set of the extracted parameters is found to be $J_{\parallel} \approx -4.27$ meV, $J_{\perp} \approx 0.59$ meV, $\zeta \approx 0.02$, and $\eta \approx 0.97$, which is very close to the best fitting parameters suggested in Ref. [38]. This confirms the legitimacy of the XY Hamiltonian of the described system.

3.5 Spin Dynamics in the Presence of Lattice Deformations

The successful description of the acousticlike magnon excitations by the two different methods encourages us to extend the scheme developed in Section 3.1 to a system with a deformation of the lattice. Lattice deformations change the equations of motion Eqs. (3.11) and (3.12) obtained in Section 3.1. The point is that deformations change distances between spins that in turn modify exchange coupling constants $J_{\|}$ and $J_{\perp}$ in Eq. (3.2). The changes of $J_{\|}$ and $J_{\perp}$ along $\boldsymbol{\delta}_1$ and $\boldsymbol{\delta}_2$ directions, denoted accordingly as $\delta J_{\|}^{\delta_1}$ and $\delta J_{\perp}^{\delta_2}$, are connected with the deformation as follolws: $\delta J_{\|}^{\delta_1} \sim (1/a)(\partial J_{\|}/\partial a)\boldsymbol{\delta}_1 \cdot (\boldsymbol{\delta}_1 \cdot \boldsymbol{\nabla u})$ and $\delta J_{\perp}^{\delta_2} \sim (1/c)(\partial J_{\perp}/\partial c)\boldsymbol{\delta}_2 \cdot (\boldsymbol{\delta}_2 \cdot \boldsymbol{\nabla u})$. Here, a and c are the dimensionless intra- and inter-layer distances, and $\boldsymbol{u}$ is the lattice displacement. As a result, for the in-plane exchange couplings describing an action on a spin located on the A sublattice by those on the B sublattice, i.e., $B \to A$, we have

$$\begin{aligned}
&\delta J_{\|}^{\delta_{1,1}} \sim g_1 \epsilon_{xx}, \\
&\delta J_{\|}^{\delta_{1,2}} \sim g_1 (\frac{1}{4}\epsilon_{xx} + \frac{3}{4}\epsilon_{yy} - \frac{\sqrt{3}}{2}\epsilon_{xy}), \\
&\delta J_{\|}^{\delta_{1,3}} \sim g_1 (\frac{1}{4}\epsilon_{xx} + \frac{3}{4}\epsilon_{yy} + \frac{\sqrt{3}}{2}\epsilon_{xy}).
\end{aligned} \tag{3.40}$$

Here, $g_1 \equiv (1/a)(\partial J_{\|}/\partial a)$, and the strain tensor $\epsilon_{\alpha\beta} \equiv (\partial_\alpha u^\beta + \partial_\beta u^\alpha)/2$ with $\alpha, \beta = x, y, z$. For the interlayer exchange couplings, this idea works similarly, and finally, with the use of the standard parametrization, we find that in the presence of a lattice deformation the linearized equations for m_θ, m_ϕ, θ, and ϕ become (c.f. Eqs. (20) and (21), the comprehensive derivation is shown in Appendix A.3)

$$\begin{aligned}
&\dot{m}_\theta \approx (4\tilde{S}^2)(-\frac{3}{8}J_{\|}\nabla_-^2\phi + \frac{9}{8}J_{\perp}\nabla_+^2\phi), \\
&\dot{\phi} \approx (-\frac{3}{2}\tilde{J}_{\|} + 9\tilde{J}_{\perp})m_\theta;
\end{aligned} \tag{3.41}$$

and

$$\begin{aligned}
&\dot{m}_\phi \approx (4\tilde{S}^2)(-\frac{3}{2}\tilde{J}_{\|}\theta - \frac{9}{8}J_{\perp}\nabla_+^2\theta), \\
&\dot{\theta} \approx (-9\tilde{J}_{\perp} - \frac{3}{8}J_{\|}\nabla_-^2 - \frac{9}{8}J_{\perp}\nabla_+^2)m_\phi.
\end{aligned} \tag{3.42}$$

Here, exchange coefficients are modified by the strain tensor

$$\tilde{J}_{\parallel} \equiv J_{\parallel} + \frac{1}{2} g_1 (\epsilon_{xx} + \epsilon_{yy}) \tag{3.43}$$

and

$$\tilde{J}_{\perp} \equiv J_{\perp} + \frac{1}{2} g_2 (\epsilon_{xx} + \epsilon_{yy} + 2\epsilon_{zz}) \tag{3.44}$$

with $g_2 \equiv (1/c)(\partial J_{\perp}/\partial c)$ to be the out-of-plane magnetoelastic coefficient. The equations (3.41) and (3.42) are one of the main results of this chapter. In Chapter 4 we will use these equations for description of scattering of the AFM magnons in the backward direction.

3.6 Additional Remarks

In this chapter, we studied the dynamics of spins in a layered van der Waals crystal CoTiO$_3$. This system is a $3D$ quantum XY AFM, with the direction of magnetization alternating between the neighboring layers. As is well known, the XY AFMs are spin analogues of the superfluid Helium and superconductors [29, 30]. The angle of orientation of the Néel vector is equivalent to the superfluid phase. Correspondingly, the long-wavelength magnons are the Goldstone excitations in an XY AFM. We have studied the spectrum of magnons using corresponding pairs of the macroscopic quantities, which are the magnetization and the Néel vector densities of various kind. We demonstrate here that for the acousticlike excitations (i.e., for the Goldstone mode), the accuracy of the scheme is almost perfect. Besides, we have confirmed the XY type of the intralayer spin exchange in this material by comparing our macroscopic description of the all four spin-wave modes with the experimental data.

In addition to the spectrum of magnons, we considered the case when the crystal lattice of the magnetic substance is deformed by an external strain. One may expect that the spin flow could be manipulated by applying a spatially modulated strain. The description of the quantum AFM developed in this chapter provides a simple ready-to-use scheme for studying the spin superfluidity in such magnetic systems, as well as the possibility to control the spin dynamics through the lattice deformation (see Chapter 4 for the details).

We would like to emphasize that at the derivation of the equations of motion for the spin-wave excitations, i.e., Eqs. (3.5)-(3.10), the route used in this chapter is somewhat different from the one in the conventional approach (cf. Refs. [26] and [27]). Conventionally, one starts from the spin Hamiltonian, then constructs the path integral using the spin coherent states and, finally, obtains the Lagrangian density which can be recognized as the nonlinear sigma model. Eventually, the equations of motion are found by making the variation of the action to be zero. In the present chapter, the order of operations was changed. We started with the derivation of the equations of motion for the quantum spin operators directly from the Hamiltonian. Then, these equations were treated in terms of the continuous variables with a nonlinear constraint. By performing this step, we effectively executed the transition to the language of the nonlinear sigma model.

4. CONTROL OF SPIN WAVES BY SPATIALLY MODULATED STRAIN IN ANTIFERROMAGNET*

In this chapter, we discuss the possibility of using a spatially modulated strain of the lattice for the control of spin waves (magnons) propagating inside bulk AFMs through the magnetoelasticity. Actually, interaction between spin waves and mechanical excitations via magnetoelasticity has been studied for a long time, starting from the works by Kittel [42]. Both, the generation of the hypersonic waves by excitation of the spin system in FMs [43] and, conversely, the generation of spin waves by pumping microwave phonons [44, 45] were discussed. Different aspects of the magnetoacoustic resonance and parametric excitation of magnetostatic and elastic modes have been considered [46, 47, 48, 49].

In recent years, parametric pumping of spin waves by acoustic waves has been experimentally realized [50] as well as elastically driven FM resonance [51, 52]. An enormous increase in the amplitude of the magnetization precession in a FM layer embedded into a phononic resonator was observed in Ref. [53] when the frequencies of magnetization precession and phonons were equal. Next, traveling acoustic waves on the surface of a piezoelectric crystal resonantly excite traveling surface spin waves in an adjacent thin-film FM. These measurements provide a spectroscopy technique for the surface spin waves [54]. Recently, a nonreciprocal surface acoustic wave propagation due to the magneto-rotation coupling was also demonstrated experimentally [55].

Here, unlike most of the works cited above, we exploit not the dynamics of phonons but rather the *spatial* modulation of the lattice. The deformation of the lattice modulates the spin exchange between magnetic atoms, which in turn acts as a scattering potential (i.e., a *magnonic crystal*) for the spin waves. The intensity of the spin wave is assumed to be weak, so that magnons are described by linearized equations, and no interconversion between phonons and magnons [56] will be considered. The main idea looks as follows: The spin wave is a degenerate excitation, i.e.,

---

*Reprinted with permission from "Control of spin waves by spatially modulated strain" by Ankang Liu and Alexander M. Finkel'stein, 2022. Phys. Rev. B, 105, L020404, Copyright 2022 by American Physical Society.

energies of the symmetric and antisymmetric eigenmodes with wave vectors $\pm k$ are degenerate. A spatial modulation caused by either a static strain [57] or a standing acoustic wave [50] with $q = 2k$ lifts this degeneracy. In the presence of a static $2k$ modulation, the picture reminds one of a particle in a symmetric double-well potential, see e.g., Fig. 4.1. Tunneling, as is well known, lifts the degeneracy of the energy levels in the double well. If originally a particle is located in one of the wells, as a result of tunneling it starts to oscillate between the two wells with a frequency proportional to the level splitting. Here, the strain leads to a similar effect. Suppose, initially, there is a free right-moving spin wave in the magnetic system and, then, at a certain moment, a strain modulation is switched on. (For example, a spin-wave packet runs inside the magnet when a strain is switched on.) As we will show in this chapter, the originally right-moving spin wave being subjected to the deformation, after some time, will alter its motion to the left-moving propagation, and so on. Thus, a direct propagation of the spin wave changes into a *to-and-fro* motion.

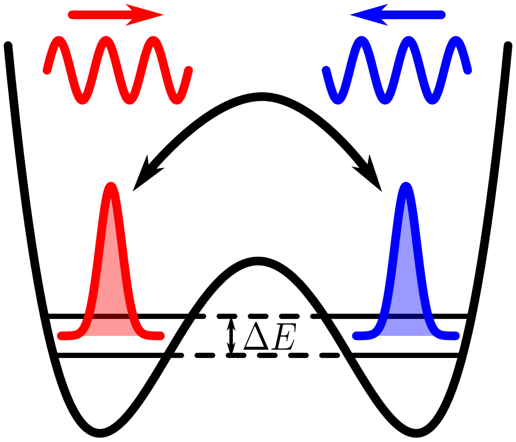

Figure 4.1: Tunneling in a symmetric double-well potential as an analogue of the to-and-fro motion of the spin wave under the strain modulation. The particle which was initially located on the left starts to tunnel to the right one, and so on. The frequency of these oscillations is given by the energy split ΔE. In the case of the spatially modulated strain, the forward- and backward-propagating spin waves correspond to the particle alternating between the left and right potential wells. The spin-wave band gap opened by the strain modulation plays the role similar to the energy splitting ΔE in the case of tunneling. Asymmetry of the potential (not shown) is equivalent to the energy mismatch of the spin wave states when $\delta k \neq 0$.

4.1 Equations of Motion under Static Strain Modulation

We are interested in a layered AFM with the spin wave propagating in the direction across the layers. For the purpose of simplicity, let us now consider a one-dimensional problem by assuming that there is a *static* deformation with only one nonzero strain tensor component $\epsilon_{zz} = \epsilon_0 \cos(qz)$ (a possible realization of the static strain modulation was proposed in Ref. [57]). Here, ϵ_0 is the magnitude of the strain tensor, and the wave vector q describes its spatial modulation along the z direction. We first explain the idea behind the calculation. The deformation induced by the strain modulates the spin exchange between magnetic atoms, which in turn acts as a scattering potential for spin waves. This simple geometry allows to illustrate the main idea. Note, however, that the method of controlling the propagation of the spin waves proposed in this chapter is general and applicable to any magnetic system. To be concrete, let us study the dynamics of the low-energy acousticlike spin waves in the van der Waals layered magnetic systems CoTiO$_3$ in the presence of the strain modulation $\epsilon_{zz} = \epsilon_0 \cos(qz)$. The equations of motion for the pair (m_θ, ϕ) now take the form (cf. Eqs. (3.41) and (3.44))

$$\begin{aligned}
\dot{m}_\theta &= J\frac{d^2}{dz^2}\phi, \\
\dot{\phi} &= [G_1 + G_2\cos(qz)]m_\theta, \qquad (4.1)
\end{aligned}$$

where $G_1 = -3J_\parallel/2 + 9J_\perp$. In the discussed geometry, with the strain applied along the direction perpendicular to the layers, there is a very clear separation of the roles of $J_\parallel$ and $J_\perp$. Namely, in the above pair of equations, $J = 9\tilde{S}^2 J_\perp$ and $G_2 = 9g_2\epsilon_0$. Here, the magnetoelastic coefficient $g_2 \equiv (1/c)(\partial J_\perp/\partial c)$ describes the sensitivity of $J_\perp$ to a modulation of the dimensionless interlayer distance c.

We proceed with Eqs. (4.1) by taking another time derivative in each of them:

$$\begin{aligned}
\ddot{m}_\theta &= (D_m + D_m^{(2)})m_\theta, \\
\ddot{\phi} &= (D_\phi + D_\phi^{(2)})\phi. \qquad (4.2)
\end{aligned}$$

Here, we defined the operators $D_{m/\phi} \equiv JG_1 d^2/dz^2$, $D_m^{(2)} \equiv JG_2 \cos(qz) d^2/dz^2 - 2JG_2 q \sin(qz) \times d/dz - JG_2 q^2 \cos(qz)$, and $D_\phi^{(2)} \equiv JG_2 \cos(qz) d^2/dz^2$. Note that m_θ and ϕ are not decoupled, because they are connected through the relation $\dot{m}_\theta = J d^2\phi/dz^2$.

4.2 Solutions of Spin Wave under Static Strain Modulation

To find eigenstate solutions for ϕ in the presence of the static strain modulation, we assume that ϕ has a form $\phi(z,t) = e^{\pm i\omega t}\varphi(z)$, substitute this ansatz into the second line of Eq. (4.2), and finally, obtain a time-independent equation for φ:

$$-\omega^2 \varphi = (D_\phi + D_\phi^{(2)})\varphi. \tag{4.3}$$

To solve this eigenvalue problem, we look for the solution

$$\varphi(z) = \sum_{k \geq 0} [\mathcal{S}_k \sin(kz) + \mathcal{C}_k \cos(kz)]. \tag{4.4}$$

In order to find the expansion coefficients $\mathcal{S}_k$ and $\mathcal{C}_k$, we calculate the matrix elements

$$\begin{aligned}
[D_\phi]_{k',k}(\chi) &\equiv \frac{1}{L}\int \sin(k'z+\chi) D_\phi \sin(kz+\chi) dz, \\
[D_\phi^{(2)}]_{k',k}(\chi) &\equiv \frac{1}{L}\int \sin(k'z+\chi) D_\phi^{(2)} \sin(kz+\chi) dz.
\end{aligned} \tag{4.5}$$

Here, χ is either 0 or $\pi/2$ (introduced for compactness), and L is the size of the system. The reason to consider only these matrix elements is that $\int \sin(k'z) D_\phi \cos(kz) dz = \int \cos(k'z) D_\phi \sin(kz) dz = 0$ and similarly for $D_\phi^{(2)}$, i.e., there is no mixture between the basis functions $\sin(kz)$ and $\cos(kz)$. After straightforward calculations, we find (recall that both k and $k' \geq 0$):

$$\begin{aligned}
[D_\phi]_{k',k}(\chi) &= -\frac{1}{2} JG_1 k^2 (\delta_{k',k} - \cos(2\chi)\delta_{k',-k}) = -\frac{1}{2} JG_1 k^2 \delta_{k',k}, \\
[D_\phi^{(2)}]_{k',k}(\chi) &= -\frac{1}{4} JG_2 k^2 [\delta_{k',k-q} + \delta_{k',k+q} - \cos(2\chi)(\delta_{k',-k-q} + \delta_{k',-k+q})]
\end{aligned}$$

$$= -\frac{1}{4}JG_2k^2 \times \begin{cases} \delta_{k',k+q} - \cos(2\chi)\delta_{k',-k+q}, & 0 \le k < q, \\ \delta_{k',0} + \delta_{k',2q} - \cos(2\chi)\delta_{k',0}, & k = q, \\ \delta_{k',k-q} + \delta_{k',k+q}, & k > q. \end{cases} \tag{4.6}$$

Here, $\delta_{k',k}$ is the Kronecker delta. As a result, we obtain a set of equations for the coefficients $\mathcal{S}_k$ and $\mathcal{C}_k$:

$$\begin{aligned} \frac{\omega^2}{2}\mathcal{S}_{k'} &= -\sum_k \Big\{[D_\phi]_{k',k}(\chi = 0) + [D_\phi^{(2)}]_{k',k}(\chi = 0)\Big\}\mathcal{S}_k, \\ \frac{\omega^2}{2}\mathcal{C}_{k'} &= -\sum_k \Big\{[D_\phi]_{k',k}(\chi = \frac{\pi}{2}) + [D_\phi^{(2)}]_{k',k}(\chi = \frac{\pi}{2})\Big\}\mathcal{C}_k. \end{aligned} \tag{4.7}$$

As a simple check, in the absence of the perturbation, $D_\phi^{(2)} = 0$, i.e., without the deformation in the system, we have

$$\omega^2 \begin{pmatrix} \mathcal{S}_{k_1} \\ \mathcal{S}_{k_2} \\ \vdots \\ \mathcal{C}_{k_1} \\ \mathcal{C}_{k_2} \\ \vdots \end{pmatrix} = JG_1 \begin{pmatrix} k_1^2 & & & & & \\ & k_2^2 & & & \mathbf{0} & \\ & & \ddots & & & \\ & & & k_1^2 & & \\ & \mathbf{0} & & & k_2^2 & \\ & & & & & \ddots \end{pmatrix} \begin{pmatrix} \mathcal{S}_{k_1} \\ \mathcal{S}_{k_2} \\ \vdots \\ \mathcal{C}_{k_1} \\ \mathcal{C}_{k_2} \\ \vdots \end{pmatrix}. \tag{4.8}$$

We find from Eq. (4.8), $\omega_k^2 = JG_1k^2$. The corresponding eigenstates are either $\mathcal{S}_k = 1$ or $\mathcal{C}_k = 1$, i.e., the solutions are $\varphi = \sin(kz)$ or $\varphi = \cos(kz)$. This is nothing but the solutions for free spin waves.

Next, we study the solutions of φ in the presence of the lattice modulation when the external perturbation $D_\phi^{(2)} \neq 0$. Under the condition $0 \le k < q$ and $k \neq q/2$, instead of a chain of coupled equations, we get a finite system of equations, and we have two systems of approximated equations for finding $\mathcal{S}_k$ and $\mathcal{C}_k$:

$$\omega^2 \begin{pmatrix} \mathcal{S}_k \\ \mathcal{S}_{k+q} \\ \mathcal{S}_{-k+q} \end{pmatrix} = M_- \begin{pmatrix} \mathcal{S}_k \\ \mathcal{S}_{k+q} \\ \mathcal{S}_{-k+q} \end{pmatrix}, \tag{4.9}$$

and

$$\omega^2 \begin{pmatrix} \mathcal{C}_k \\ \mathcal{C}_{k+q} \\ \mathcal{C}_{-k+q} \end{pmatrix} = M_+ \begin{pmatrix} \mathcal{C}_k \\ \mathcal{C}_{k+q} \\ \mathcal{C}_{-k+q} \end{pmatrix}, \tag{4.10}$$

where

$$M_\pm = JG_1 \begin{pmatrix} k^2 & \frac{1}{2}(\frac{G_2}{G_1})(k+q)^2 & \pm\frac{1}{2}(\frac{G_2}{G_1})(-k+q)^2 \\ \frac{1}{2}(\frac{G_2}{G_1})k^2 & (k+q)^2 & 0 \\ \pm\frac{1}{2}(\frac{G_2}{G_1})k^2 & 0 & (-k+q)^2 \end{pmatrix}. \tag{4.11}$$

Here, we neglected the terms which couple the coefficients of interest with higher harmonics: $\mathcal{S}_{\pm k+q} \leftrightarrow \mathcal{S}_{\pm k+2q}$, $\mathcal{S}_{\pm k+2q} \leftrightarrow \mathcal{S}_{\pm k+3q}$, $\cdots$, and $\mathcal{C}_{\pm k+q} \leftrightarrow \mathcal{C}_{\pm k+2q}$, $\mathcal{C}_{\pm k+2q} \leftrightarrow \mathcal{C}_{\pm k+3q}$, $\cdots$. The arguments to neglect the higher order harmonics are comprehensively discussed in Appendix B.1.

A special case is when $k = q/2$, which we will define it as the "*spatial resonance*". In this case, after further neglecting the higher harmonics such as $\mathcal{S}_{3q/2}$ and $\mathcal{C}_{3q/2}$, one can treat the z-coordinate dependencies in the spirit of the parametric resonance theory (however, the resonance discussed here is for the wave vectors rather than frequencies). As a result, Eqs. (4.9) and (4.10) are reduced to a pair of decoupled equations:

$$\omega^2 \mathcal{S}_{\frac{q}{2}} = JG_1[1 - \frac{1}{2}(\frac{G_2}{G_1})](\frac{q}{2})^2 \mathcal{S}_{\frac{q}{2}} \tag{4.12}$$

and

$$\omega^2 \mathcal{C}_{\frac{q}{2}} = JG_1[1 + \frac{1}{2}(\frac{G_2}{G_1})](\frac{q}{2})^2 \mathcal{C}_{\frac{q}{2}}. \tag{4.13}$$

The above equations lead to the split frequencies $\omega^2_{\mathcal{S},q/2} = JG_1[1 - (G_2/2G_1)](q/2)^2$ and $\omega^2_{\mathcal{C},q/2} = JG_1[1 + (G_2/2G_1)](q/2)^2$ for the modes $\sin(qz/2)$ and $\cos(qz/2)$, respectively.

Now let us focus on a more general case in which the wave vector k deviates from the exact resonance condition, but remains not too far from it. Namely, $k = q/2 + \delta k$ with $|\delta k| \ll q/2$. In this situation, the components $\mathcal{S}_{k+q}$ and $\mathcal{C}_{k+q}$ are excessive, and neglecting them we get the equations with the components $q/2 + \delta k$ and $q/2 - \delta k$ appeared to be mixed:

$$\omega^2 \begin{pmatrix} \mathcal{S}_{\frac{q}{2}+\delta k} \\ \mathcal{S}_{\frac{q}{2}-\delta k} \end{pmatrix} = JG_1 \begin{pmatrix} (\frac{q}{2}+\delta k)^2 & -\frac{1}{2}(\frac{G_2}{G_1})(\frac{q}{2}-\delta k)^2 \\ -\frac{1}{2}(\frac{G_2}{G_1})(\frac{q}{2}+\delta k)^2 & (\frac{q}{2}-\delta k)^2 \end{pmatrix} \begin{pmatrix} \mathcal{S}_{\frac{q}{2}+\delta k} \\ \mathcal{S}_{\frac{q}{2}-\delta k} \end{pmatrix}, \tag{4.14}$$

and

$$\omega^2 \begin{pmatrix} \mathcal{C}_{\frac{q}{2}+\delta k} \\ \mathcal{C}_{\frac{q}{2}-\delta k} \end{pmatrix} = JG_1 \begin{pmatrix} (\frac{q}{2}+\delta k)^2 & \frac{1}{2}(\frac{G_2}{G_1})(\frac{q}{2}-\delta k)^2 \\ \frac{1}{2}(\frac{G_2}{G_1})(\frac{q}{2}+\delta k)^2 & (\frac{q}{2}-\delta k)^2 \end{pmatrix} \begin{pmatrix} \mathcal{C}_{\frac{q}{2}+\delta k} \\ \mathcal{C}_{\frac{q}{2}-\delta k} \end{pmatrix}. \tag{4.15}$$

Eqs. (4.14) and (4.15) lead to the eigenvalues

$$\begin{aligned} \omega^2_{\pm}(\delta k) =& \frac{1}{2}\Big\{ JG_1[(\frac{q}{2}+\delta k)^2 + (\frac{q}{2}-\delta k)^2] \\ & \pm \sqrt{J^2G_1^2[(\frac{q}{2}+\delta k)^2 - (\frac{q}{2}-\delta k)^2]^2 + J^2G_2^2(\frac{q}{2}+\delta k)^2(\frac{q}{2}-\delta k)^2} \Big\}. \end{aligned} \tag{4.16}$$

The corresponding eigenvectors are $u^{\mathcal{S}}_{\pm} = \{1, A_{\mp}(\delta k)\}^T$ for $\{\mathcal{S}_{q/2+\delta k}, \mathcal{S}_{q/2-\delta k}\}^T$, and $u^{\mathcal{C}}_{\pm} = \{1, -A_{\mp}(\delta k)\}^T$ for $\{\mathcal{C}_{q/2+\delta k}, \mathcal{C}_{q/2-\delta k}\}^T$, with $A_{\mp}(\delta k)$ are defined to be

$$\begin{aligned} A_{\mp}(\delta k) \equiv& \frac{1}{JG_2(\frac{q}{2}-\delta k)^2}\Big\{ JG_1[(\frac{q}{2}+\delta k)^2 - (\frac{q}{2}-\delta k)^2] \\ & \mp \sqrt{J^2G_1^2[(\frac{q}{2}+\delta k)^2 - (\frac{q}{2}-\delta k)^2]^2 + J^2G_2^2(\frac{q}{2}+\delta k)^2(\frac{q}{2}-\delta k)^2} \Big\}. \end{aligned} \tag{4.17}$$

As a result of the described manipulations, one obtains for the solutions of φ

$$\varphi^{\mathcal{S}}_{\pm}(z)\big|_{\delta k} \propto \big(\sin[(\frac{q}{2}+\delta k)z] + A_{\mp}(\delta k)\sin[(\frac{q}{2}-\delta k)z]\big), \tag{4.18}$$

and

$$\varphi^{\mathcal{C}}_{\pm}(z)\big|_{\delta k} \propto \big(\cos[(\frac{q}{2}+\delta k)z] - A_{\mp}(\delta k)\cos[(\frac{q}{2}-\delta k)z]\big). \tag{4.19}$$

Note that $A_{\mp}(\delta k \to 0) = \mp 1$, so that non-vanishing solutions become $\varphi^{\mathcal{S}}_{-} \sim \sin(qz/2)$ and $\varphi^{\mathcal{C}}_{+} \sim \cos(qz/2)$, respectively. The corresponding frequencies $\omega_{\mp}(\delta k \to 0)$ are given by Eqs. (4.12) and (4.13). In this way, we recovered the results for $k = q/2$, i.e., at the exact resonance.

With the ansatz $\phi = e^{-i\omega t}\varphi$, and keeping in mind the relation $\dot{m}_\theta = Jd^2\phi/dz^2$, we get eight pairs of the linearly independent solutions (ϕ, m_θ) for $k = q/2 + \delta k$.

$$\begin{aligned}
\phi^{\mathcal{S}}_{1\pm} =& \Big\{\sin[(\frac{q}{2}+\delta k)z] + A_{\mp}\sin[(\frac{q}{2}-\delta k)z]\Big\}\cos(\omega_{\pm}t),\\
m^{\mathcal{S}}_{\theta 1\pm} =& -\frac{1}{\omega_{\pm}}\Big\{J(\frac{q}{2}+\delta k)^2\sin[(\frac{q}{2}+\delta k)z] + A_{\mp}J(\frac{q}{2}-\delta k)^2\sin[(\frac{q}{2}-\delta k)z]\Big\}\sin(\omega_{\pm}t);
\end{aligned} \tag{4.20}$$

$$\begin{aligned}
\phi^{\mathcal{S}}_{2\pm} =& \Big\{\sin[(\frac{q}{2}+\delta k)z] + A_{\mp}\sin[(\frac{q}{2}-\delta k)z]\Big\}\sin(\omega_{\pm}t),\\
m^{\mathcal{S}}_{\theta 2\pm} =& \frac{1}{\omega_{\pm}}\Big\{J(\frac{q}{2}+\delta k)^2\sin[(\frac{q}{2}+\delta k)z] + A_{\mp}J(\frac{q}{2}-\delta k)^2\sin[(\frac{q}{2}-\delta k)z]\Big\}\cos(\omega_{\pm}t);
\end{aligned} \tag{4.21}$$

$$\begin{aligned}
\phi^{\mathcal{C}}_{1\pm} =& \Big\{\cos[(\frac{q}{2}+\delta k)z] - A_{\mp}\cos[(\frac{q}{2}-\delta k)z]\Big\}\cos(\omega_{\pm}t),\\
m^{\mathcal{C}}_{\theta 1\pm} =& -\frac{1}{\omega_{\pm}}\Big\{J(\frac{q}{2}+\delta k)^2\cos[(\frac{q}{2}+\delta k)z] - A_{\mp}J(\frac{q}{2}-\delta k)^2\cos[(\frac{q}{2}-\delta k)z]\Big\}\sin(\omega_{\pm}t);
\end{aligned} \tag{4.22}$$

and

$$\phi^{\mathcal{C}}_{2\pm} = \Big\{\cos[(\frac{q}{2}+\delta k)z] - A_{\mp}\cos[(\frac{q}{2}-\delta k)z]\Big\}\sin(\omega_{\pm}t),$$

$$m^{\mathcal{C}}_{\theta 2\pm} = \frac{1}{\omega_\pm}\Big\{J(\frac{q}{2}+\delta k)^2\cos[(\frac{q}{2}+\delta k)z] - A_\mp J(\frac{q}{2}-\delta k)^2\cos[(\frac{q}{2}-\delta k)z]\Big\}\cos(\omega_\pm t). \quad (4.23)$$

4.3 To-and-fro Motion at the Resonance

Let us assume that initially there is a freely propagating spin wave with $\phi(z,t) = \phi_0\sin[(qz/2) - \Omega t + \varphi_1]$, where in the absence of the strain $\Omega = \sqrt{JG_1}(q/2) \equiv v_s(q/2)$. Next, at a moment $t = 0$, the strain modulation with the wave vector q switches on. In this sense, φ_1 is defined as the phase differences of the freely propagating spin wave and the strain modulation at the moment of switching on the deformation. The modulation splits the energy of the initially degenerate states. We demonstrate now that the difference between $\omega_{\mathcal{C},q/2}$ and $\omega_{\mathcal{S},q/2}$ leads to a *to-and-fro* motion for the $q/2$-spin wave, exactly like in the case of a particle in the double-well with the energy levels split by tunneling. In the following part of this section we discuss this to-and-fro motion in detail.

By matching the spin-wave solutions under the static strain modulation with the initial conditions $\phi(z,t=0) = \phi_0\sin[(qz/2)+\varphi_1]$ and $m_\theta(z,t=0) = -[J(q/2)^2\phi_0/\Omega]\cos[(qz/2)+\varphi_1]$, and after neglecting all the small terms, one obtains

$$\begin{aligned}\phi \approx{}& \phi_0\Big\{(+1)\cos\left(\frac{\omega_{\downarrow\uparrow}t}{2}\right)\sin[(\frac{q}{2})z - \Omega t + \varphi_1]\\ &+ (-1)\sin\left(\frac{\omega_{\downarrow\uparrow}t}{2}\right)\cos[(\frac{q}{2})z + \Omega t - \varphi_1]\Big\}. \quad (4.24)\end{aligned}$$

The resulting combination describes alternation between the two components propagating in the opposite directions. It works as follows: When $|\cos(\omega_{\downarrow\uparrow}t/2)| > |\sin(\omega_{\downarrow\uparrow}t/2)|$, see Fig 4.2, the right-propagating component dominates, and thus the superposition of the right- and left-propagating waves is moving toward the right, and vice versa. For an *observer* focused on a certain point of the wave it will look like *to-and-fro* motion of the spin wave. (In the case of the wave packet of spin waves centered around the wave vector $k = q/2$, the packet will exhibit an alternating motion in the opposite directions, see Appendix B.2 for the result of simulations.) As follows from Eq. (4.24) and Fig. 4.2, the propagation direction of the spin wave alters with the frequency $\omega_{\downarrow\uparrow} \equiv \omega_{\mathcal{C},q/2} - \omega_{\mathcal{S},q/2} \approx (G_2/2G_1)\sqrt{JG_1}(q/2) = (G_2/2G_1)\Omega$. For illustration, we plot

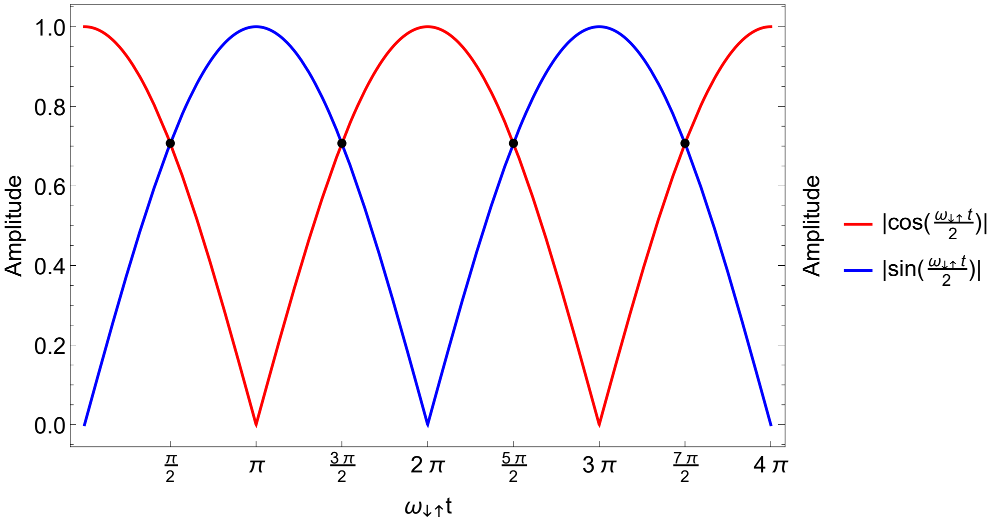

Figure 4.2: The time dependence of the coefficients of the right- and left-propagating wave components according to Eq. (4.24).

in Fig. 4.3 the “position of the wave" as a function of time at different G_2 by tracking the profile (e.g., the zero crossing) of the propagating wave. We observe a number of zigzag curves describing the to-and-fro motion with slopes corresponding to the velocity of free spin waves. The propagation direction alters with a frequency, which is proportional to the magnitude of the deformation of the lattice induced by the strain. (From Fig. 4.3 we observe that at $G_1 = 2$ the picture works qualitatively well up to $G_2 \lesssim 0.9$ confirming the generality of the explanation.)

4.4 Out-of-resonance Motion of the Spin Wave

When it comes to a slightly-out-of-resonance situation, i.e., $k = q/2 + \delta k$ with $\delta k \neq 0$ and $|\delta k| \ll q/2$, the eight solutions given by Eqs. (4.20) - (4.23) allow to look for the general solution (ϕ, m_θ) in the form $\phi = \alpha^{\mathcal{S}}_{1+}\phi^{\mathcal{S}}_{1+} + \alpha^{\mathcal{S}}_{1-}\phi^{\mathcal{S}}_{1-} + \alpha^{\mathcal{S}}_{2+}\phi^{\mathcal{S}}_{2+} + \alpha^{\mathcal{S}}_{2-}\phi^{\mathcal{S}}_{2-} + \alpha^{\mathcal{C}}_{1+}\phi^{\mathcal{C}}_{1+} + \alpha^{\mathcal{C}}_{1-}\phi^{\mathcal{C}}_{1-} + \alpha^{\mathcal{C}}_{2+}\phi^{\mathcal{C}}_{2+} + \alpha^{\mathcal{C}}_{2-}\phi^{\mathcal{C}}_{2-}$ and $m_\theta = \alpha^{\mathcal{S}}_{1+}m^{\mathcal{S}}_{\theta 1+} + \alpha^{\mathcal{S}}_{1-}m^{\mathcal{S}}_{\theta 1-} + \alpha^{\mathcal{S}}_{2+}m^{\mathcal{S}}_{\theta 2+} + \alpha^{\mathcal{S}}_{2-}m^{\mathcal{S}}_{\theta 2-} + \alpha^{\mathcal{C}}_{1+}m^{\mathcal{C}}_{\theta 1+} + \alpha^{\mathcal{C}}_{1-}m^{\mathcal{C}}_{\theta 1-} + \alpha^{\mathcal{C}}_{2+}m^{\mathcal{C}}_{\theta 2+} + \alpha^{\mathcal{C}}_{2-}m^{\mathcal{C}}_{\theta 2-}$.

The coefficients $\alpha^{S/C}_{1\pm}$ and $\alpha^{S/C}_{2\pm}$ have to be determined from the initial conditions. Suppose that initially, in the absence of the external perturbation, i.e., in the region where $D^{(2)}_{m/\phi} = 0$, a free spin wave with a wave vector $q/2 + \delta k$ is running in the system. This free spin wave is

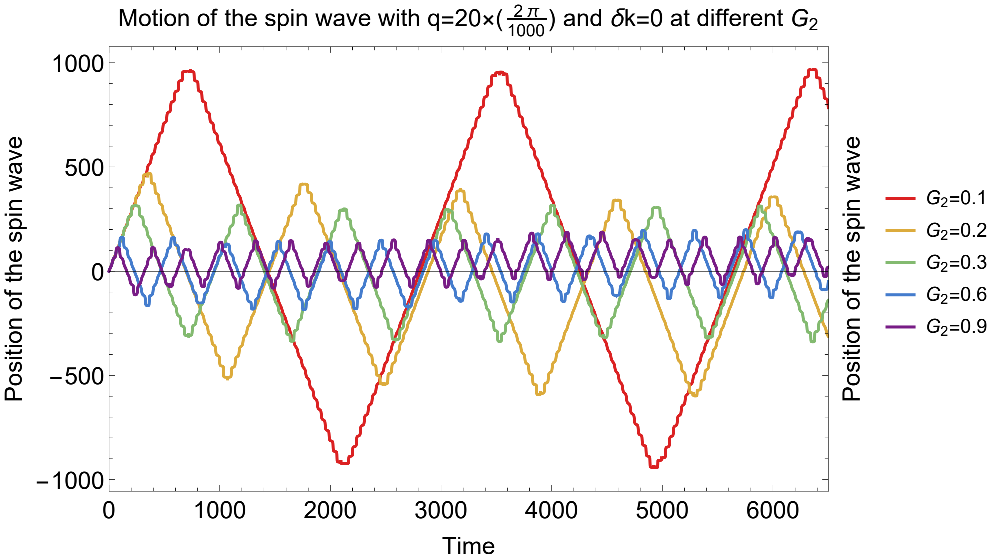

Figure 4.3: Position of spin waves at the spatial resonance condition, $k = q/2$, as a function of time for different G_2. Wave vector $q = 20 \times (2\pi/1000)$; other parameters are $J = 1$, $G_1 = 2$, and $\varphi_1 = 0$.

described by the pair solution $\phi(z,t) = \phi_0 \sin[(q/2+\delta k)z - \omega_0 t + \varphi_1]$ and $m_\theta(z,t) = -[J(q/2+\delta k)^2\phi_0/\omega_0]\cos[(q/2+\delta k)z - \omega_0 t + \varphi_1]$ with ϕ_0 to be the amplitude of ϕ. The frequency of this wave is $\omega_0 \equiv \omega_0(k = q/2+\delta k) = \sqrt{JG_1}(q/2+\delta k)$, and φ_1 is an arbitrary phase. Now, at $t = 0$, the perturbation term $D_\phi^{(2)} \neq 0$ is switched on. We are interested in the effect of the *static* modulation of the lattice on the propagation of the spin wave. Taking the general solution in the presence of the external perturbation, and matching the initial conditions, i.e., $\phi(z,t=0) = \phi_0 \sin[(q/2+\delta k)z + \varphi_1]$ and $m_\theta(z,t=0) = -[J(q/2+\delta k)^2\phi_0/\omega_0]\cos[(q/2+\delta k)z+\varphi_1]$, we find the coefficients

$$\begin{aligned}
\alpha_{1\pm}^{\mathcal{S}} &= \pm\frac{A_\pm(\delta k)}{A_+(\delta k)-A_-(\delta k)}\phi_0\cos(\varphi_1),\\
\alpha_{2\pm}^{\mathcal{S}} &= \pm\frac{A_\pm(\delta k)}{A_+(\delta k)-A_-(\delta k)}\frac{\omega_\pm}{\omega_0}\phi_0\sin(\varphi_1),\\
\alpha_{1\pm}^{\mathcal{C}} &= \pm\frac{A_\pm(\delta k)}{A_+(\delta k)-A_-(\delta k)}\phi_0\sin(\varphi_1),\\
\alpha_{2\pm}^{\mathcal{C}} &= \mp\frac{A_\pm(\delta k)}{A_+(\delta k)-A_-(\delta k)}\frac{\omega_\pm}{\omega_0}\phi_0\cos(\varphi_1).
\end{aligned}\tag{4.25}$$

After some tedious but straightforward calculations, we arrange the solution ϕ in the form

$$\begin{aligned}\phi =&\phi_0\Big\{\beta_1 \cos\left(\frac{\omega_{\downarrow\uparrow}t}{2}\right)\sin[(\frac{q}{2}+\delta k)z+\Omega t+\varphi_1]+\beta_2\sin\left(\frac{\omega_{\downarrow\uparrow}t}{2}\right)\cos[(\frac{q}{2}+\delta k)z+\Omega t+\varphi_1]\\ &+\beta_3 \cos\left(\frac{\omega_{\downarrow\uparrow}t}{2}\right)\sin[(\frac{q}{2}+\delta k)z-\Omega t+\varphi_1]+\beta_4\sin\left(\frac{\omega_{\downarrow\uparrow}t}{2}\right)\cos[(\frac{q}{2}+\delta k)z-\Omega t+\varphi_1]\\ &+\beta_5 \cos\left(\frac{\omega_{\downarrow\uparrow}t}{2}\right)\sin[(\frac{q}{2}-\delta k)z+\Omega t-\varphi_1]+\beta_6\sin\left(\frac{\omega_{\downarrow\uparrow}t}{2}\right)\cos[(\frac{q}{2}-\delta k)z+\Omega t-\varphi_1]\\ &+\beta_7 \cos\left(\frac{\omega_{\downarrow\uparrow}t}{2}\right)\sin[(\frac{q}{2}-\delta k)z-\Omega t-\varphi_1]+\beta_8\sin\left(\frac{\omega_{\downarrow\uparrow}t}{2}\right)\cos[(\frac{q}{2}-\delta k)z-\Omega t-\varphi_1]\Big\}\end{aligned} \tag{4.26}$$

with $\Omega \equiv (\omega_+ + \omega_-)/2$, $\omega_{\downarrow\uparrow} \equiv \omega_+ - \omega_-$, and the coefficients

$$\begin{aligned}\beta_1 =&\frac{1}{2}[\frac{A_+}{A_+-A_-}(1-\frac{\omega_+}{\omega_0})-\frac{A_-}{A_+-A_-}(1-\frac{\omega_-}{\omega_0})],\\ \beta_2 =&\frac{1}{2}[\frac{A_+}{A_+-A_-}(1-\frac{\omega_+}{\omega_0})+\frac{A_-}{A_+-A_-}(1-\frac{\omega_-}{\omega_0})],\\ \beta_3 =&\frac{1}{2}[\frac{A_+}{A_+-A_-}(1+\frac{\omega_+}{\omega_0})-\frac{A_-}{A_+-A_-}(1+\frac{\omega_-}{\omega_0})],\\ \beta_4 =&-\frac{1}{2}[\frac{A_+}{A_+-A_-}(1+\frac{\omega_+}{\omega_0})+\frac{A_-}{A_+-A_-}(1+\frac{\omega_-}{\omega_0})],\\ \beta_5 =&\frac{1}{2}[\frac{A_+A_-}{A_+-A_-}(1+\frac{\omega_+}{\omega_0})-\frac{A_+A_-}{A_+-A_-}(1+\frac{\omega_-}{\omega_0})],\\ \beta_6 =&\frac{1}{2}[\frac{A_+A_-}{A_+-A_-}(1+\frac{\omega_+}{\omega_0})+\frac{A_+A_-}{A_+-A_-}(1+\frac{\omega_-}{\omega_0})],\\ \beta_7 =&\frac{1}{2}[\frac{A_+A_-}{A_+-A_-}(1-\frac{\omega_+}{\omega_0})-\frac{A_+A_-}{A_+-A_-}(1-\frac{\omega_-}{\omega_0})],\\ \beta_8 =&-\frac{1}{2}[\frac{A_+A_-}{A_+-A_-}(1-\frac{\omega_+}{\omega_0})+\frac{A_+A_-}{A_+-A_-}(1-\frac{\omega_-}{\omega_0})].\end{aligned} \tag{4.27}$$

We point out that, unlike in the previous section, all parameters presented here as well as in the remaining part of this chapter, e.g., Ω and $\omega_{\downarrow\uparrow}$, are defined at a finite δk, rather than at $\delta k = 0$. When $\delta k \to 0$, one can observe that $\beta_1, \beta_8 \to 0$, $|\beta_2|, |\beta_4|, |\beta_5|, |\beta_7| \to |G_2/8G_1| \ll 1$, while $\beta_3 \to 1$, and $\beta_6 \to -1$. After neglecting all the small terms, i.e., keeping only the β_3 and β_6 terms, Eq. (4.26) becomes the approximated solution given by Eq. (4.24) in the previous section.

The approximated ϕ-solution (4.26) contains 8 time-dependent components (which consist of two different quasimomenta $q/2 \pm \delta k$, two opposite propagating directions, and two basis functions). The resulting motions are presented in Fig. 4.4. First of all, one may notice that the durations of motion in the opposite directions are not equal anymore. Furthermore, there is a critical value δk_c, so that for $|\delta k| > \delta k_c$, the to-and-fro motion of the spin wave ceases to exist. For the discussed choice of the parameters, $\delta k_c \approx 0.38 \times (2\pi/1000)$.

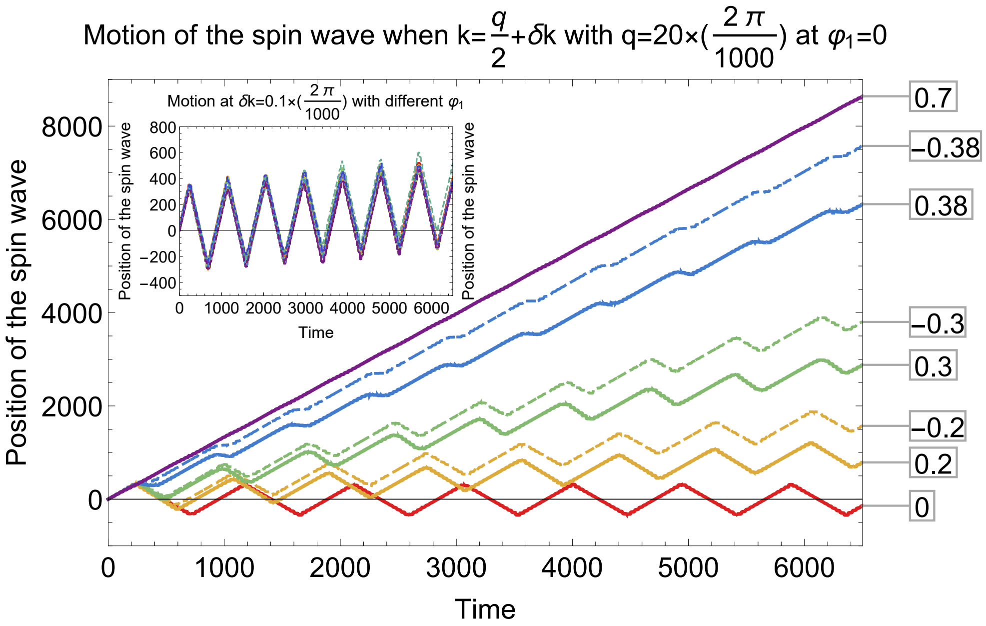

Figure 4.4: Propagation of spin waves with various δk given in the unit $(2\pi/1000)$ (see boxes on the right). The parameters used for this simulation are $q = 20 \times (2\pi/1000)$, and $J = 1$, $G_1 = 2$, $G_2 = 0.3$, $\varphi_1 = 0$. Inset is plotted for the wave at $\delta k = 0.1 \times (2\pi/1000)$ with different phases φ_1, which range from $-\pi$ to π.

The critical value δk_c can be determined by comparing the energy difference of the two spin waves connected through the external perturbation term $G_2 \cos(qz)$, with the splitting energy $\omega_{\downarrow\uparrow}$. At $\delta k = \delta k_c$ the energy difference $2v_s\delta k$ meets the splitting energy $\omega_{\downarrow\uparrow}$; see Fig. 4.5 (cf. tunneling in the slightly asymmetric double-well potential).

Next, in the inset of Fig. 4.4, we study the effect of the phase φ_1 in the initial conditions, which appears to be negligible. This can be explained as follows: As one can notice from Eq. (4.24), the

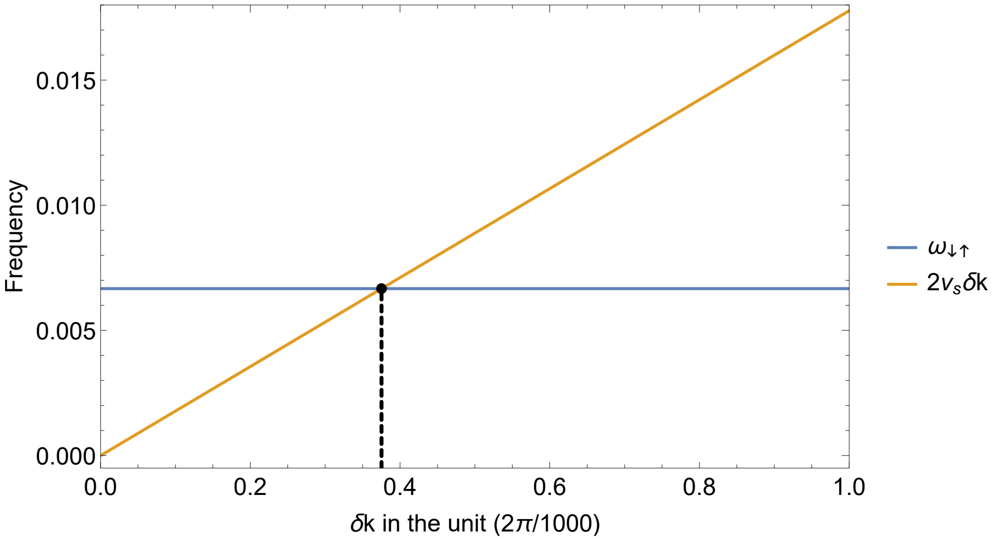

Figure 4.5: The energy splitting of the free spin waves with $k = q/2 \pm \delta k$, which are connected through the perturbation term $G_2 \cos(qz)$. The orange line is the energy splitting, while the blue line is $\omega_{\downarrow\uparrow}$.

right- and left-propagating wave components contain φ_1 only in the combination $\pm(\Omega t - \varphi_1)$. By shifting the time with $t_0 = \varphi_1/\Omega$, the phase is transferred to the arguments in the time-dependent coefficients. As a result, from $\omega_{\downarrow\uparrow}t/2$ they change to $\omega_{\downarrow\uparrow}(t + t_0)/2$, and therefore the effect of the shift leads only to a change in the moment of the turn of the propagating wave; cf. Fig. 4.2. The same argument works for $\delta k \neq 0$ as well; see Eq. (4.26). Furthermore, because of the smallness of $\omega_{\downarrow\uparrow}/2\Omega$, the effect appears to be negligible. Hence φ_1 practically does not affect the propagation of the spin wave.

This observation is of upmost importance. The absence of sensitivity to φ_1 implies that meeting of a spin-wave packet with the induced strain modulation can be considered instantaneous. In other words, the deformation effectively switches on for the whole wave packet simultaneously.

4.5 Evolution of the Coefficients $\beta_1, \beta_2, \beta_3, \beta_4, \beta_5, \beta_6, \beta_7$, and β_8 with δk

To have a better understanding of the dynamics of the scattered spin wave, we plot in Fig. 4.6 the dependence of the coefficients β_1-β_8 on δk. First, we have checked that at $\delta k = 0$ only $\beta_3 = 1$ and $\beta_6 = -1$ are the only relevant terms, while all other β-coefficients are negligible.

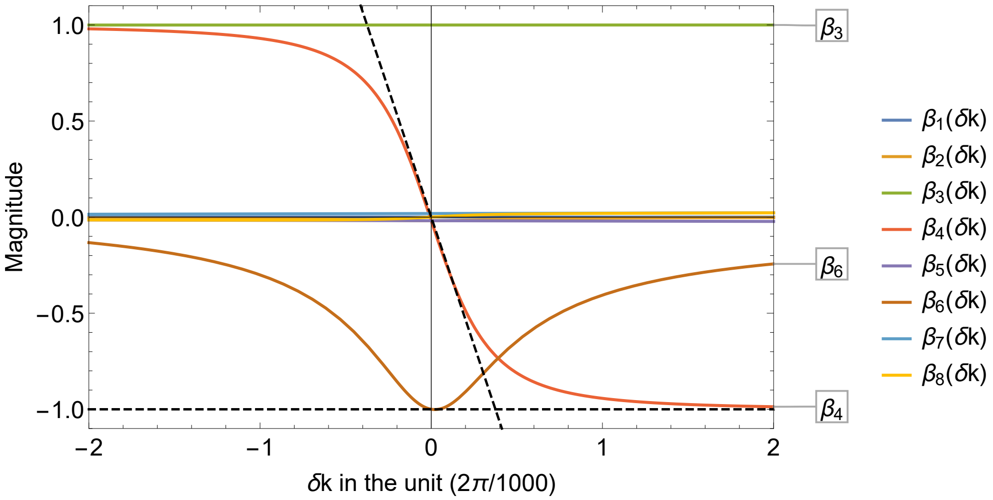

Figure 4.6: δk-dependence of the eight coefficients β_1-β_8 for $q = 20 \times (2\pi/1000)$. Parameters of the system are $J = 1$, $G_1 = 2$, $G_2 = 0.3$. The two dashed black lines intersect at $\delta k_c = G_2 q/8G_1$, which is the critical value of δk determined through the criterion $2v_s\delta k_c = \omega_{\downarrow\uparrow}(\delta k = 0)$. For $k > \delta k_c$, propagation of a spin wave is unidirectional.

Next, with $\delta k \neq 0$, the magnitude of β_6 starts to decrease. As a result, the balance between the right- and left-propagating components shifts in favor of the β_3-term, which is not sensitive to δk (i.e., remains unchanged). In Eq. (4.26), the time intervals when β_3-term dominates over β_6-term exceed the other ones when β_6 takes over. As a result we observe the imbalance between the wave propagating in the two opposite directions presented by a number of curves in Fig. 4.4.

At the same time, the magnitude of β_4 grows with δk, while other five β-coefficients remain to be negligible. At $\delta k_c \approx G_2 q/8G_1$, the magnitude of β_4 becomes comparable with β_6. Consequently, according to Eq. (4.26), when $\delta k > \delta k_c$, β_4-term surpasses β_6-term. For a spin wave this leads to ceasing of motion in the backward direction, and as a result the propagation becomes unidirectional. This observation is consistent with the criterion $2v_s\delta k_c \approx \omega_{\downarrow\uparrow}(\delta k = 0)$ for the vanishing of the to-and-fro motion (see Fig. 4.5 for illustration of this point). Finally, as $\delta k \to \infty$, $\beta_3 \to 1$, $\beta_4 \to -1$, and $\beta_6 \to 0$, so the leading terms in Eq. (4.26) become β_3- and β_4-term. As a consequence, the sum of these two terms, $\phi \approx \phi_0\{\cos(\omega_{\downarrow\uparrow}t/2)\sin[(q/2 + \delta k)z - \Omega t + \varphi_1] - \sin(\omega_{\downarrow\uparrow}t/2)\cos[(q/2 + \delta k)z - \Omega t + \varphi_1]\} = \phi_0 \sin[(q/2 + \delta k)z - (\Omega + \omega_{\downarrow\uparrow}/2)t + \varphi_1] \to \phi_0 \sin[(q/2 + \delta k)z - \omega_0 t + \varphi_1]$, which is the freely propagating spin wave with $k = q/2 + \delta k$. This result indicates that the spatially modulated strain essentially does not affect the propagation of the spin waves which are far from the spatial resonance.

Thus, the evolution of the dynamics is fully determined by the interplay of only three terms with the coefficients β_3, β_4, and β_6, while the other terms are non-essential. In particular, the change of the alternating motion to a straight propagation of the spin wave becomes very clear.

4.6 Additional Remarks

To demonstrate the generality of the idea, we also considered an oblique incidence when the initial spin wave has a finite momentum component perpendicular to the direction of strain modulation. We observed that in this case the modulated strain acts like a waveguide; see Appendix B.3 for the details. Namely, the to-and-fro motion develops along the direction of modulation, while in the direction perpendicular to the strain modulation the wave propagates freely.

For the sake of completeness, we further investigated the dynamics of spin wave (see Appendix B.4) in the presence of a time-dependent strain modulation $\epsilon_{zz} = \epsilon_0 \cos(qz) \cos(\omega_{ph} t + \varphi_2)$. This can be achieved by a standing acoustic wave $\boldsymbol{u} = A \sin(qz) \cos(\omega_{ph} t + \varphi_2) \hat{z}$; see, e.g., Ref. [50]. Under the spatial resonance condition, we have observed that the to-and-fro motion can develop but is limited to the frequencies $\omega_{ph} \lesssim \omega_{\downarrow\uparrow}$, and its dynamics strongly depend on the phase φ_2.

In this chapter, we discussed propagation of spin waves across the layered AFM material in the presence of a static spatially modulated strain. We have found an alternating to-and-fro motion of the spin wave when its momentum is about half of the wave vector of the strain modulation, i.e., $k \approx q/2$ (we call it the *spatial resonance* condition). The frequency of this to-and-fro motion $\omega_{\downarrow\uparrow}$ is proportional to the amplitude of the deformation.

As a practical application, this phenomenon can be used for controlling the spin-wave packets. Suppose a packet of spin waves centered around the wave vector $q/2$ is traveling freely across the layered magnetic system. Then, at a certain moment, one activates the modulated strain along the transverse direction with the quasi-momentum q. (Alternatively, perhaps more realistically for experimental realization, the wave packet runs inside the magnet when the deformation is switched on.) As follows from the discussion of Fig. 4.4, the Fourier components in the packet, which are closest to $q/2$, perform the to-and-fro motion, while the components that are more distant from $q/2$ pass through the sample. In this regard, the spatial modulation can work as a spin-wave filter and a delay line element.

5. SPIN-WAVE DYNAMICS CONTROLLED BY TUNABLE AC MAGNONIC CRYSTAL IN FERROMAGNET*

As an efficient way to control spin waves, magnonic crystals have been studied extensively [39, 40, 41, 58]. One of the most effective ways to control the spin-wave propagation in a FM, as it was demonstrated experimentally, is through a current-induced magnonic crystal [39, 40]. A

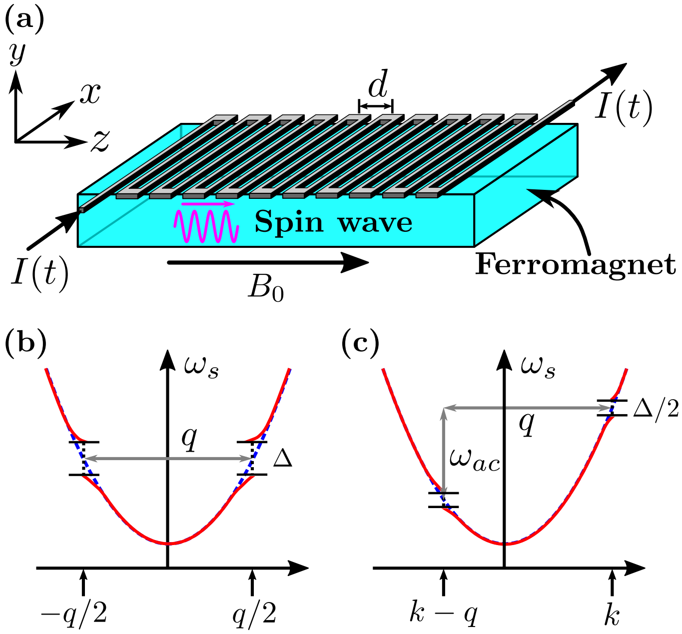

Figure 5.1: (a) A schematic setup of the current-induced magnonic crystal, which was used for studying the spin-wave dynamics in experiments [39] and [40]. The meander structure at the top of the FM creates a spatially modulated magnetic field, which is $\propto I(t)\cos(qz)\hat{z}$, along the z direction. Here, $q = 2\pi/d$. In the second row, we sketch the spin-wave spectrum when the magnonic crystal is switched on (the solid red curves) and when it is not effective (the dashed blue curves). Subfigure (b) is for the DC magnonic crystal while (c) is for the AC case (the gaps around the wave vectors $q-k$ and $-k$ are not shown). The band gap $\Delta \propto I_0$. Note that the band gap caused by the AC magnonic crystal is the half of the one created by the DC with the same amplitude I_0.

---

[*] Reprinted with permission from "Spin-wave dynamics controlled by tunable ac magnonic crystal" by Ankang Liu and Alexander M. Finkel'stein, 2023. Phys. Rev. B (to be published), Copyright 2023 by American Physical Society.

prototypical current-induced magnonic crystal for FM is schematically depicted in Fig. 5.1(a). If a DC current, $I(t) = I_0$, is supplied through a metallic meander structure with a period d, a spatially modulated static magnetic field generates a magnonic crystal for the spin waves propagating along the direction of the modulation. The key advantage of the current-induced magnonic crystal is its ability to be easily switched on and off, which provides a highly controllable manner for manipulating the propagation of spin waves. For the spin waves with a symmetric spectrum, the DC magnonic crystal resonantly couples the spin waves with wave vectors around $\pm q/2$, where $q = 2\pi/d$ is determined by the period of the spatial modulation. As shown in Fig. 5.1(b), the coupling of the two degenerate waves opens a band gap Δ, which is $\propto I_0$ [39, 40]. In practice, for an incident spin-wave packet, after switching on the DC magnonic crystal, the spin-wave components that are under the resonant scattering conditions start to alternate between the forward- and backward-propagating states; while the out-of-resonance spectral components are unaffected by the perturbation and propagate unidirectionally.

In this chapter, we consider the same experimental setup as was exploited in Ref. [39] or [40], but extend the discussion to an AC modulated magnonic crystal, i.e., when the current $I(t) = I_0 \cos(\omega_{ac} t + \varphi_{ac})$. We show that under the limit $\omega_{ac} \gg \Delta$ a spin-wave pair with wave vectors k and $k - q$ can be controlled by a *tunable* AC magnonic crystal that satisfies the *shifted resonance* condition $|\omega_s(k) - \omega_s(k - q)| = \omega_{ac}$ (cf. Fig. 5.1(c)).

5.1 Spin-wave Scattering Induced by Magnonic Crystals

Suppose that, initially (i.e., at $t < 0$), there was a free spin wave with wave vector $\boldsymbol{k} = k\hat{z}$ propagating inside the FM sample. We consider a device fabricated from a FM with all spins located on a cubic lattice. To present the idea we will restrict ourselves to the spin-wave excitations originating from the short-range exchange couplings. This is sufficient for illustrating the concept of the shifted resonance. Note that the scheme proposed in this chapter is general and applicable to all types of spin waves (e.g., the dipolar spin-wave modes). In the continuum limit, the spin operators become a space- and time-dependent variable $\boldsymbol{S}(\boldsymbol{r}, t)$ (cf. Chapter 2). Before the magnonic crystal is switched on, the constant external magnetic field $\boldsymbol{B} = B_0 \boldsymbol{e}_z$ aligns all spins along the

z direction in the ground state. In the case of a spin-wave excitation, $\boldsymbol{S}(\boldsymbol{r},t)$ deviates from the equilibrium and acquires small $S^{x,y}(\boldsymbol{r},t)$. The linearized equation in $S^{x,y}(\boldsymbol{r},t)$ can be solved by a plane wave $S^{+}(\boldsymbol{r},t) \equiv S^{x}(\boldsymbol{r},t) + iS^{y}(\boldsymbol{r},t) = (\Delta S)e^{i[\boldsymbol{k}\cdot\boldsymbol{r}-\omega_s(\boldsymbol{k})t+\varphi_s]}$, where ΔS is the amplitude of the spin wave, φ_s is its initial phase, and $\omega_s(\boldsymbol{k}) = Ak^2 + \gamma B_0$ gives the spin-wave dispersion. The second term in the dispersion is due to the constant external magnetic field, $A > 0$ is determined by the FM exchange coupling between the nearest neighboring spins, and γ is the gyromagnetic ratio of the spin.

Next, at $t = 0$, one switches on the AC modulated magnonic crystal, which for $t > 0$ is described by $\Delta B_0 \cos(\omega_{ac}t + \varphi_{ac})\cos(qz)\hat{z}$. Here, ΔB_0 is the intensity of the magnonic crystal controlled by I_0, the frequency of the AC modulation is given by ω_{ac}, while φ_{ac} is the initial phase determined at the moment $t = 0$. In the discussed geometry, the spin-wave propagation is effectively one-dimensional. To find what will be the dynamics of the spin wave after $t = 0$, one needs to solve $S^{+}(z,t)$ from the equation

$$\frac{dS^{+}}{dt} = iA\nabla^2 S^{+} - i\gamma[B_0 + \Delta B_0\cos(\omega_{ac}t + \varphi_{ac})\cos(qz)]S^{+}, \tag{5.1}$$

by matching the solution for $t > 0$ with the free spin-wave solution for $t < 0$. Equation 5.1, which describes the spin-wave dynamics under the magnonic crystal, is simply obtained by adding the magnetic filed terms to Eq. (2.5).

The magnonic crystal term in Eq. (5.1) couples the spin-wave state k to the state $k - q$ as long as $|\omega_s(k) - \omega_s(k-q)| \approx \omega_{ac}$. To better understand the spin-wave dynamics under the AC magnonic crystal, we look for the solution of Eq. (5.1) in the form

$$S^{+}(z,t) = (\Delta S)\big[\mathcal{S}_p(t)\sin(k_+z) + \mathcal{S}_m(t)\sin(k_-z) + \mathcal{C}_p(t)\cos(k_+z) + \mathcal{C}_m(t)\cos(k_-z)\big]. \tag{5.2}$$

Here, we introduced four complex time-dependent coefficients $\mathcal{S}_{p/m}(t)$ and $\mathcal{C}_{p/m}(t)$ in front of the basis functions $\sin(k_\pm z)$ and $\cos(k_\pm z)$, respectively. Solution (5.2) describes the mutual scatterings between a pair of the spin waves with the wave vectors $k = k_+ = q/2 + \delta k$ and $k - q = -k_- =$

$-q/2 + \delta k$. Although the scattering occurs between the spin waves with the oppositely directed wave vectors, the wave vectors $k_\pm$ are defined here as their absolute values and, therefore, are positive (we assume that $-q/2 < \delta k < q/2$). Note that, in Eq. (5.2), the contributions from the spin waves with wave vectors $\pm 3q/2 + \delta k$ and higher are neglected. This is well justified in the situations we will be interested in (see the discussion on this point later).

5.2 Spin-wave Solution under DC and AC Magnonic Crystals

Here we find explicitly the spin-wave solution after switching on the current-induced magnonic crystal. To proceed, we substitute the ansatz (5.2) back into Eq. (5.1), and neglecting the higher harmonics, we obtain for the four complex coefficients:

$$\begin{aligned}
\dot{\mathcal{S}}_p(t) =& - i\omega_s(k_+)\mathcal{S}_p(t) + i\left(\frac{\gamma\Delta B_0}{2}\right)\cos(\omega_{ac}t + \varphi_{ac})\mathcal{S}_m(t),\\
\dot{\mathcal{S}}_m(t) =& - i\omega_s(k_-)\mathcal{S}_m(t) + i\left(\frac{\gamma\Delta B_0}{2}\right)\cos(\omega_{ac}t + \varphi_{ac})\mathcal{S}_p(t),\\
\dot{\mathcal{C}}_p(t) =& - i\omega_s(k_+)\mathcal{C}_p(t) - i\left(\frac{\gamma\Delta B_0}{2}\right)\cos(\omega_{ac}t + \varphi_{ac})\mathcal{C}_m(t),\\
\dot{\mathcal{C}}_m(t) =& - i\omega_s(k_-)\mathcal{C}_m(t) - i\left(\frac{\gamma\Delta B_0}{2}\right)\cos(\omega_{ac}t + \varphi_{ac})\mathcal{C}_p(t).
\end{aligned} \tag{5.3}$$

By matching Eq. (5.2) with the free spin-wave solution at $t = 0$, we find the corresponding initial conditions are

$$\mathcal{S}_p(t=0) = ie^{i\varphi_s},\ \mathcal{S}_m(t=0) = 0,\ \mathcal{C}_p(t=0) = e^{i\varphi_s},\ \mathcal{C}_m(t=0) = 0. \tag{5.4}$$

We further proceed with the equations of motion for the pair $\mathcal{S}_{p/m}(t)$ in Eq. (5.3) by rewriting them as $i\frac{d}{dt}\left|\psi_{\mathcal{S}}(t)\right\rangle = \hat{H}_{\mathcal{S}}(t)\left|\psi_{\mathcal{S}}(t)\right\rangle$ with $\left|\psi_{\mathcal{S}}(t)\right\rangle \equiv (\mathcal{S}_p(t), \mathcal{S}_m(t))^T$ and

$$\hat{H}_{\mathcal{S}}(t) \equiv \Omega\hat{\sigma}_0 + \frac{\Delta\omega_s}{2}\hat{\sigma}_3 - \left(\frac{\gamma\Delta B_0}{2}\right)\cos(\omega_{ac}t + \varphi_{ac})\hat{\sigma}_1. \tag{5.5}$$

Here, $\hat{\sigma}_0 \equiv \mathbb{1}_{2\times 2}$ is the 2×2 identity matrix, while $\hat{\sigma}_i$ with $i = 1, 2, 3$ are the standard Pauli matrices. Recall that $\Omega \equiv [\omega_s(k_+) + \omega_s(k_-)]/2$ and $\Delta\omega_s \equiv \omega_s(k_+) - \omega_s(k_-)$. Note that the

Hamiltonian (5.5) describes a system that is an analogue of the two-level atom perturbed by a linearly polarized light. The Hamiltonian that governs the time evolution of the pair $\mathcal{C}_{p/m}(t)$ is the same as Eq. (5.5) but with $\Delta B_0 \to -\Delta B_0$.

The general forms of the time-dependent solution pairs $\mathcal{S}_{p/m}(t)$ and $\mathcal{C}_{p/m}(t)$ are govern by Floquet theorem [59, 60]. Notice, however, the important difference between the problem discussed here and the ones associated with the so-called "Floquet engineering" (cf. Refs. [61] and [62]). The Floquet engineering utilizes a time-dependent-only perturbation to tailor the effective Hamiltonian, which in turn modifies the physical properties of a given system, while in the discussed AC magnonic crystal the external perturbation is periodic both in time and *space*. Moreover, we are interested in the dynamics of the excitation (i.e., the spin wave) driven by the external signal, rather than how the magnetic system acquires a modified state.

5.2.1 DC magnonic crystal

At $\omega_{ac} = 0$ and $\varphi_{ac} = 0$, the Hamiltonian (5.5) is time-independent and can be diagonalized by its eigenstates

$$\left|\psi_{\mathcal{S}}^{\pm}\right\rangle = \frac{1}{\sqrt{1 + f_{\mp}^2(\xi)}} \begin{pmatrix} 1 \\ f_{\mp}(\xi) \end{pmatrix}. \tag{5.6}$$

Here, $f_{\pm}(\xi) \equiv \xi \pm \sqrt{1+\xi^2}$ and $\xi \equiv \Delta\omega_s / \gamma\Delta B_0$. After diagonalization, the Hamiltonian (5.5) becomes

$$\hat{H}_{\mathcal{S}} = \omega_+ \left|\psi_{\mathcal{S}}^{+}\right\rangle \left\langle\psi_{\mathcal{S}}^{+}\right| + \omega_- \left|\psi_{\mathcal{S}}^{-}\right\rangle \left\langle\psi_{\mathcal{S}}^{-}\right|, \tag{5.7}$$

where

$$\omega_{\pm} = \Omega \pm \left(\frac{\gamma\Delta B_0}{2}\right)\sqrt{1+\xi^2}. \tag{5.8}$$

Therefore, the time-dependent solution of $\hat{H}_{\mathcal{S}}$ can be written as

$$|\psi_{\mathcal{S}}(t)\rangle = e^{-i\omega_+ t}\left|\psi_{\mathcal{S}}^+\right\rangle\left\langle\psi_{\mathcal{S}}^+\middle|\psi_{\mathcal{S}}(t=0)\right\rangle + e^{-i\omega_- t}\left|\psi_{\mathcal{S}}^-\right\rangle\left\langle\psi_{\mathcal{S}}^-\middle|\psi_{\mathcal{S}}(t=0)\right\rangle \tag{5.9}$$

with $|\psi_{\mathcal{S}}(t=0)\rangle$ to be the initial state. After substituting the initial condition $|\psi_{\mathcal{S}}(t=0)\rangle = (ie^{i\varphi_s}, 0)^T$, we find

$$\begin{pmatrix} \mathcal{S}_p(t) \\ \mathcal{S}_m(t) \end{pmatrix} = \frac{ie^{-i(\omega_+ t-\varphi_s)}}{1+f_-^2(\xi)}\begin{pmatrix} 1 \\ f_-(\xi) \end{pmatrix} + \frac{ie^{-i(\omega_- t-\varphi_s)}}{1+f_+^2(\xi)}\begin{pmatrix} 1 \\ f_+(\xi) \end{pmatrix}. \tag{5.10}$$

Similarly, for the pair $\mathcal{C}_{p/m}(t)$, one gets

$$\begin{pmatrix} \mathcal{C}_p(t) \\ \mathcal{C}_m(t) \end{pmatrix} = \frac{e^{-i(\omega_+ t-\varphi_s)}}{1+f_-^2(\xi)}\begin{pmatrix} 1 \\ -f_-(\xi) \end{pmatrix} + \frac{e^{-i(\omega_- t-\varphi_s)}}{1+f_+^2(\xi)}\begin{pmatrix} 1 \\ -f_+(\xi) \end{pmatrix}. \tag{5.11}$$

Finally, we plug the solutions (5.10) and (5.11) back into Eq. (5.2), and take its real and imaginary parts. After the straightforward calculations we obtain

$$\begin{aligned} S^x(z,t) = \mathrm{Re}[S^+(z,t)] =& \Delta S\Bigg[(1)\cos\left(\frac{\omega_{\downarrow\uparrow}t}{2}\right)\cos\left(k_+z-\Omega t+\varphi_s\right) \\ &+ \rho_1(\xi)\sin\left(\frac{\omega_{\downarrow\uparrow}t}{2}\right)\sin\left(k_+z-\Omega t+\varphi_s\right) \\ &- \rho_2(\xi)\sin\left(\frac{\omega_{\downarrow\uparrow}t}{2}\right)\sin\left(k_-z+\Omega t-\varphi_s\right)\Bigg] \end{aligned} \tag{5.12}$$

from the real part of Eq. (5.2). As for the imaginary part, we find

$$\begin{aligned} S^y(z,t) = \mathrm{Im}[S^+(z,t)] =& \Delta S\Bigg[(1)\cos\left(\frac{\omega_{\downarrow\uparrow}t}{2}\right)\sin\left(k_+z-\Omega t+\varphi_s\right) \\ &- \rho_1(\xi)\sin\left(\frac{\omega_{\downarrow\uparrow}t}{2}\right)\cos\left(k_+z-\Omega t+\varphi_s\right) \\ &- \rho_2(\xi)\sin\left(\frac{\omega_{\downarrow\uparrow}t}{2}\right)\cos\left(k_-z+\Omega t-\varphi_s\right)\Bigg]. \end{aligned} \tag{5.13}$$

Here, two ρ functions are

$$\rho_1(\xi) = \frac{\xi}{\sqrt{1+\xi^2}},\ \rho_2(\xi) = \frac{1}{\sqrt{1+\xi^2}}. \tag{5.14}$$

In Eqs. (5.12) and (5.13), $\omega_{\downarrow\uparrow} \equiv \omega_{\downarrow\uparrow}(\xi) = (\gamma\Delta B_0)\sqrt{1+\xi^2}$. Here ξ is a dimensionless variable defined as $\xi(\delta k) \equiv \Delta\omega_s(\delta k)/\gamma\Delta B_0$ with $\Delta\omega_s(\delta k) \equiv \omega_s(k_+) - \omega_s(k_-)$; note that $\Delta\omega_s$ depends on δk critically. The parameter ξ describes the level of the energy mismatch of the two spin waves participating in the scattering induced by the DC magnonic crystal; $\Omega \equiv \Omega(\delta k) \equiv [\omega_s(k_+) + \omega_s(k_-)]/2$ is a sort of "central frequency" which depends on δk non-critically. We would like to emphasize that $\omega_{\downarrow\uparrow}$ and Ω introduced here as well as $\omega_\pm$ in Eq. (5.8) are very different from those defined in Chapter 4.

A further insight for understanding the spin-wave dynamics can be obtained by noticing that $[\cos(\omega_{\downarrow\uparrow}t/2)]^2 + [\rho_1(\xi)\sin(\omega_{\downarrow\uparrow}t/2)]^2 = |\mathcal{S}_p(t)|^2 = |\mathcal{C}_p(t)|^2$ and $[\rho_2(\xi)\sin(\omega_{\downarrow\uparrow}t/2)]^2 = |\mathcal{S}_m(t)|^2 = |\mathcal{C}_m(t)|^2$. $|\mathcal{S}_m(t)|^2$ alternates between 0 and $|\rho_2(\xi)|^2$, while $|\mathcal{S}_p(t)|^2$ is between 1 and $|\rho_1(\xi)|^2$. Let us now interpret $|\mathcal{S}_m(t)|^2$ (or $|\mathcal{C}_m(t)|^2$) as the "probability" of finding the spin wave in the reflected state (i.e., the left-propagating component), while $|\mathcal{S}_p(t)|^2$ (or $|\mathcal{C}_p(t)|^2$) to be the "probability" for the wave to propagate in the original right direction. Then, the whole picture becomes a wave version of the Rabi oscillations [63] with the Rabi frequency $\omega_{\downarrow\uparrow}(\xi)$. Note that $|\mathcal{S}_p(t)|^2+|\mathcal{S}_m(t)|^2 = 1$, which is guaranteed by the unitarity of this system. When $|\delta k| > \delta k_c$ (this corresponds to $|\xi| > 1$), $|\rho_1(\xi)|$ surpasses $|\rho_2(\xi)|$ and the right-propagating wave component starts to fully dominate over the left-propagating one. As a result, the to-and-fro motion ceases to exist; see Appendix C.1 for further details.

At large δk when $\xi \gg 1$, $\rho_1 \to 1$ and $\rho_2 \to 0$, so that $S^y(z,t)$ converts into $(\Delta S)\sin[(q/2 + \delta k)z - \omega_s^+ t + \varphi_s]$ and, in this way, the free propagation of the spin wave recovers. In other words, the two spin-wave states, k and $k-q$, are essentially disconnected when their energy difference is much greater than $\gamma\Delta B_0$. In a similar way, one can safely ignore the spin-wave components with higher wave vectors in Eq. (2) as long as $|\omega_s\left(\pm 3q/2+\delta k\right) - \omega_s\left(\pm q/2+\delta k\right)| \gg \gamma\Delta B_0$ hold, which is indeed true in our case.

5.2.2 AC magnonic crystal

Now, we turn to the AC modulated magnonic crystal. As it was pointed out previously, when $\omega_{ac} \neq 0$, the general form of the solution pairs $\mathcal{S}_{p/m}(t)$ and $\mathcal{C}_{p/m}(t)$ is governed by Floquet theorem, and the time dependence of the spin-wave dynamics is determined by the quasi-energies of the system. Here we focus only on an important limit when $\omega_{ac} \approx \Delta\omega_s \gg \gamma\Delta B_0$. In this limit, one can implement the rotating wave approximation (RWA) [59]. To demonstrate how the RWA works, we first transform the pair $\mathcal{S}_{p/m}(t)$ to a rotating frame through the unitary transformation $\hat{R}(t)$:

$$\begin{pmatrix} \mathcal{S}_p(t) \\ \mathcal{S}_m(t) \end{pmatrix} = \hat{R}(t) \begin{pmatrix} \bar{\mathcal{S}}_p(t) \\ \bar{\mathcal{S}}_m(t) \end{pmatrix} \equiv e^{-i\left[(\Omega t)\hat{\sigma}_0 + \left(\frac{\omega_{ac}t+\varphi_{ac}}{2}\right)\hat{\sigma}_3\right]} \begin{pmatrix} \bar{\mathcal{S}}_p(t) \\ \bar{\mathcal{S}}_m(t) \end{pmatrix}. \tag{5.15}$$

Then, using $i\frac{d}{dt}\left|\psi_{\mathcal{S}}(t)\right\rangle = \hat{H}_{\mathcal{S}}(t)\left|\psi_{\mathcal{S}}(t)\right\rangle$, one finds in the rotating frame, the equation of motion for $\bar{\mathcal{S}}_{p/m}(t)$ becomes

$$\begin{aligned} i\frac{d}{dt}\begin{pmatrix} \bar{\mathcal{S}}_p(t) \\ \bar{\mathcal{S}}_m(t) \end{pmatrix} =& \Bigg[\left(\frac{\Delta\omega_s - \omega_{ac}}{2}\right)\hat{\sigma}_3 - \frac{\gamma\Delta B_0}{4}\hat{\sigma}_1 - \frac{\gamma\Delta B_0}{4}\Big(\cos[2(\omega_{ac}t + \varphi_{ac})]\hat{\sigma}_1 \\ & - \sin[2(\omega_{ac}t + \varphi_{ac})]\hat{\sigma}_2 \Big) \Bigg] \begin{pmatrix} \bar{\mathcal{S}}_p(t) \\ \bar{\mathcal{S}}_m(t) \end{pmatrix} \\ \approx& \left[\left(\frac{\Delta\omega_s - \omega_{ac}}{2}\right)\hat{\sigma}_3 - \frac{\gamma\Delta B_0}{4}\hat{\sigma}_1 \right] \begin{pmatrix} \bar{\mathcal{S}}_p(t) \\ \bar{\mathcal{S}}_m(t) \end{pmatrix}. \end{aligned} \tag{5.16}$$

In the last line of Eq. (5.16) we dropped the counter-rotating part of the Hamiltonian, which has a frequency $2\omega_{ac}$. This is justified as long as the condition $\omega_{ac} \approx \Delta\omega_s \gg \gamma\Delta B_0$ is fulfilled.

After neglecting the counter-rotating part in Eq. (5.16), one can analytically solve it to get the RWA solution. We first diagonalize the time-independent Hamiltonian given in the last line of Eq. (5.16) by finding its eigenvalues and eigenvectors. Then we construct the solution for $\bar{\mathcal{S}}_{p/m}(t)$

using a proper initial condition (similar to the steps from Eq. (5.6) to (5.10)). Finally, we transform $\bar{\mathcal{S}}_{p/m}(t)$ back to $\mathcal{S}_{p/m}(t)$, and get

$$\begin{aligned}
\mathcal{S}_p(t) \approx & ie^{-i\left[\left(\Omega+\frac{\omega_{ac}}{2}\right)t-\varphi_s\right]}\left[\frac{e^{-i\omega_{R+}t}}{1+f_-^2(\tilde{\xi})}+\frac{e^{-i\omega_{R-}t}}{1+f_+^2(\tilde{\xi})}\right], \\
\mathcal{S}_m(t) \approx & ie^{-i\left[\left(\Omega-\frac{\omega_{ac}}{2}\right)t-\varphi_s-\varphi_{ac}\right]}\left[\frac{f_-(\tilde{\xi})e^{-i\omega_{R+}t}}{1+f_-^2(\tilde{\xi})}+\frac{f_+(\tilde{\xi})e^{-i\omega_{R-}t}}{1+f_+^2(\tilde{\xi})}\right].
\end{aligned} \tag{5.17}$$

Similarly, for the pair $\mathcal{C}_{p/m}(t)$, we have

$$\begin{aligned}
\mathcal{C}_p(t) \approx & e^{-i\left[\left(\Omega+\frac{\omega_{ac}}{2}\right)t-\varphi_s\right]}\left[\frac{e^{-i\omega_{R+}t}}{1+f_-^2(\tilde{\xi})}+\frac{e^{-i\omega_{R-}t}}{1+f_+^2(\tilde{\xi})}\right], \\
\mathcal{C}_m(t) \approx & -e^{-i\left[\left(\Omega-\frac{\omega_{ac}}{2}\right)t-\varphi_s-\varphi_{ac}\right]}\left[\frac{f_-(\tilde{\xi})e^{-i\omega_{R+}t}}{1+f_-^2(\tilde{\xi})}+\frac{f_+(\tilde{\xi})e^{-i\omega_{R-}t}}{1+f_+^2(\tilde{\xi})}\right].
\end{aligned} \tag{5.18}$$

Here, $\omega_{R\pm} \equiv \pm(\gamma\Delta B_0/4)\sqrt{1+\tilde{\xi}^2}$ and again, $f_\pm(\tilde{\xi}) \equiv \tilde{\xi} \pm \sqrt{1+\tilde{\xi}^2}$, but with $\tilde{\xi} \equiv 2(\Delta\omega_s - \omega_{ac})/\gamma\Delta B_0$. Eventually, by putting the above results into the Eq. (5.2), and after simplifications we find

$$\begin{aligned}
S^x(z,t) = \mathrm{Re}[S^+(z,t)] \approx & \Delta S\Bigg\{(1)\cos\left(\frac{\omega_R t}{2}\right)\cos\left[k_+z-\left(\Omega+\frac{\omega_{ac}}{2}\right)t+\varphi_s\right] \\
& +\rho_1(\tilde{\xi})\sin\left(\frac{\omega_R t}{2}\right)\sin\left[k_+z-\left(\Omega+\frac{\omega_{ac}}{2}\right)t+\varphi_s\right] \\
& -\rho_2(\tilde{\xi})\sin\left(\frac{\omega_R t}{2}\right)\sin\left[k_-z+\left(\Omega-\frac{\omega_{ac}}{2}\right)t-\varphi_s-\varphi_{ac}\right]\Bigg\}
\end{aligned} \tag{5.19}$$

for the real part, while the imaginary part yields

$$\begin{aligned}
S^y(z,t) = \mathrm{Im}[S^+(z,t)] \approx & \Delta S\Bigg\{(1)\cos\left(\frac{\omega_R t}{2}\right)\sin\left[k_+z-\left(\Omega+\frac{\omega_{ac}}{2}\right)t+\varphi_s\right] \\
& -\rho_1(\tilde{\xi})\sin\left(\frac{\omega_R t}{2}\right)\cos\left[k_+z-\left(\Omega+\frac{\omega_{ac}}{2}\right)t+\varphi_s\right] \\
& -\rho_2(\tilde{\xi})\sin\left(\frac{\omega_R t}{2}\right)\cos\left[k_-z+\left(\Omega-\frac{\omega_{ac}}{2}\right)t-\varphi_s-\varphi_{ac}\right]\Bigg\}.
\end{aligned} \tag{5.20}$$

Here, $\omega_R \equiv \omega_R(\tilde{\xi}) = (\gamma\Delta B_0/2)\sqrt{1+\tilde{\xi}^2}$ while functions $\rho_1(\tilde{\xi})$ and $\rho_2(\tilde{\xi})$ have the same form as in Eq. (5.14). However, $\tilde{\xi}$ is defined differently; $\tilde{\xi}(\delta k) \equiv 2[\Delta\omega_s(\delta k) - \omega_{ac}]/\gamma\Delta B_0$. Note that, besides the shift of $\Delta\omega_s$ on the frequency ω_{ac}, there is a factor 2 in $\tilde{\xi}$. The reason why we have $\gamma\Delta B_0/2$ in ω_R (instead of $\gamma\Delta B_0$ as in $\omega_{\downarrow\uparrow}$ for the DC case) is that the AC modulation splits into the rotating and counter-rotating parts, and only the contribution from the rotating component has to be taken into account within the RWA.

Note that the spin-wave solutions in both DC and AC cases (cf. Eqs. (5.13) and (5.20)) possess the same structure, which contain three time-oscillating terms. The existence of only three terms can be understood by observing that the time evolution described by the two-level Hamiltonian (5.5) is equivalent to the rotation of a spin solely around its first and third axes.

5.3 To-and-fro Motion and Shifted Resonance

To better understand the spin-wave dynamics under both DC and AC magnonic crystals, in Fig. 5.2(a) we plot a momentary "position" of the spin wave with wave vector $q/2 + \delta k$ as a function of time for different δk after the DC magnonic crystal is switched on at $t = 0$. The "position" was determined by tracking numerically the most left zero-crossing point of the imaginary part of the spin-wave solution (5.2) within a sufficiently large spatial interval (this is similar to how we tracked the spin-wave position in Fig. 4.3). As one can see from Fig. 5.2(a), at $\delta k = 0$, the dependence of spin-wave position on time is a zigzag curve around the horizontal axis which indicates the resulting to-and-fro propagation of the spin wave. The period of this zigzag curve is extracted to be $T_{\downarrow\uparrow} \approx 6283 \approx 2\pi/\gamma\Delta B_0$, which indicates that the gap Δ induced by the DC magnonic crystal is equal to $\gamma\Delta B_0$ (cf. Fig. 5.1(b)). Moreover, from Fig. 5.2(a), one may conclude that the to-and-fro motion exists only for a limited interval of δk when $|\delta k| < \delta k_c \approx 0.33$ in units of $(2\pi/1000)$. The critical value δk_c is roughly determined by the criterion $\Delta\omega_s(\delta k_c) = \gamma\Delta B_0$. For the chosen parameters, we get $\Delta\omega_s(0.33) \approx 0.00104$ while $\gamma\Delta B_0 = 0.001$.

By properly tuning ω_{ac}, the resonant spin-wave wave vector can be *noticeably* shifted from $q/2$. As one may observe from Fig. 5.2(b), if ω_{ac} is set to be 0.00316, only the spin waves around $k = 11$ perform the to-and-fro motion accurately enough. For the chosen parameters, namely,

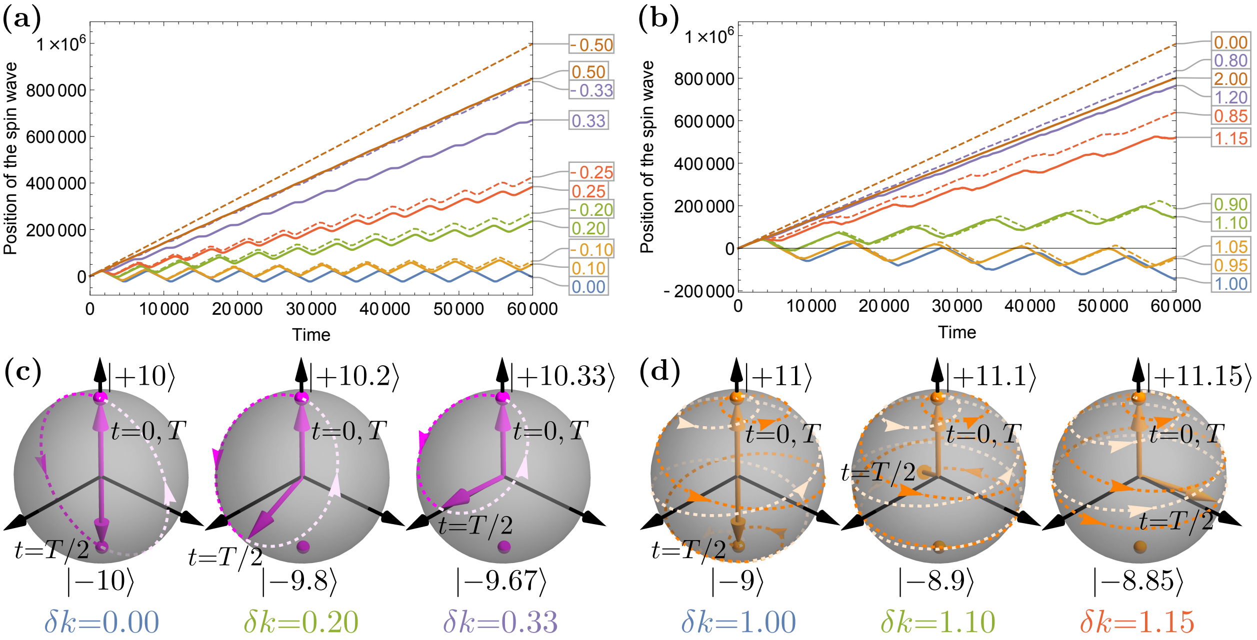

Figure 5.2: Time-dependent position of the spin waves with wave vectors $q/2 + \delta k$ after (a) the DC magnonic crystal and (b) the AC magnonic crystal ($\omega_{ac} = 0.00316$) is switched on at $t = 0$. On the panels (a) and (b), different δk (in units of $(2\pi/1000)$) are indicated by the number in the rectangular boxes. Other parameters are $A = 2$, $q = 20 \times (2\pi/1000)$, $\gamma B_0 = 1$, $\Delta = \gamma\Delta B_0 = 0.001$, and $\varphi_s = \varphi_{ac} = 0$. In our plots, the length on the vertical axis is in units of the lattice constant, which is taken to be 1, while the time on the horizontal axis is measured in units $1/\gamma B_0$. The connection between the scales of the spin-wave dynamics in a real physical system and those shown in the figures is discussed in Section 5.6 below. (c) and (d) show the Bloch-sphere trajectories of the spin waves with three different δk. The trajectories (dashed magenta and orange curves with arrowheads on the surface of the sphere) are plotted only for the first period of the to-and-fro motions; the paths of the second half period are indicated by the light colors. The intermediate positions of each of the waves are shown by the colored 3D arrows at $t = 0$, $T/2$, and T, where T is the period of the to-and-fro motions.

$A = 2$ and $q = 20$, one has $\Delta\omega_s(\delta k = 1) \approx 0.00316$ and, therefore, the *shifted resonance* (cf. Fig. 5.1(b)) indeed happens at $\tilde{\xi} \approx 0$. Furthermore, in Fig. 5.2(b), the period of the zigzag curves around the horizontal axis is doubled as compared with the one in Fig. 5.2(a). In addition, the width of the δk intervals at which the to-and-fro motion develops becomes approximately half of the one in the DC case. For example, in Fig. 5.2(b), the to-and-fro motion can be observed within the interval $10.85 \lesssim k \lesssim 11.15$, while for the DC magnonic crystal presented in Fig. 5.2(a) it develops when the spin-wave wave vectors are within $9.67 \lesssim k \lesssim 10.33$. All these observations are consistent with our understanding based on the solutions presented by Eqs. (5.12) and (5.19).

The DC or AC magnonic crystal created by a metallic meander structure (which is the "hardware" part of the magnonic crystal) with a fixed period $d = 2\pi/q$ can be utilized for the control of the spin waves around $k = q/2$ or where k satisfies the shifted resonance condition $|\omega_s(k) - \omega_s(k-q)| = \omega_{ac}$. As it was presented in Figs. 5.2(a) and 5.2(b), the spin waves, which are at the resonances (the regular or shifted ones), perform the to-and-fro motion, while the out-of-resonance spin waves are almost unaffected. The to-and-fro frequency is determined by the band gap, which is controlled by the amplitude of the supplied DC or AC current. The band gap is $\gamma\Delta B_0$ or $\gamma\Delta B_0/2$ (notice the factor $1/2$ here) in the DC or AC case. The DC spin-wave dynamics has been demonstrated in Ref. [40] as the oscillatory energy exchange between the wave and its counter-propagating reflection. However, the AC dynamics still remains to be investigated experimentally.

5.4 Bloch-sphere Representation

The spin-wave solutions, e.g., the RWA solution (5.19) in the AC case can be written as

$$\begin{aligned} |SW\rangle \equiv S^+(z,t) \equiv & e^{-i\varphi_g(t)} \Bigg\{ \left[\cos\left(\frac{\omega_R t}{2}\right) - i\rho_1(\tilde{\xi}) \sin\left(\frac{\omega_R t}{2}\right) \right] |k\rangle \\ & + \rho_2(\tilde{\xi}) \sin\left(\frac{\omega_R t}{2}\right) e^{i(\omega_{ac} t + \varphi_{ac} - \pi/2)} |k-q\rangle \Bigg\}. \end{aligned} \tag{5.21}$$

Here, $|k\rangle \equiv (\Delta S) e^{i(k_+ z)}$ and $|k-q\rangle \equiv (\Delta S) e^{i(-k_- z)}$ are two states associated with the wave vectors $k = k_+$ and $k - q = -k_-$. In the second line, the global phase is given with $\varphi_g(t) \equiv$

$\omega_{ac}t/2 + \Omega t - \varphi_s$. (For the DC case, one can obtain the same result as in Eq. (5.21) by replacing ω_R with $\omega_{\downarrow\uparrow}$ and taking both ω_{ac} and φ_{ac} to be 0.)

The state $|SW\rangle$ described by Eq. (5.21) can be represented by a vector, whose ending point is moving on the surface of a Bloch sphere with $|k\rangle$ and $|k-q\rangle$ to be its north and south poles. The motion of the states with different initial wave vectors k on the Bloch spheres, after turning on the DC and AC magnonic crystal, are shown in Figs. 5.2(c) and 5.2(d), respectively. As demonstrated by Fig. 5.2(c), at the resonance (i.e., when $\delta k = 0$), during the first period of the to-and-fro motion, the spin-wave state, which is initially located at the north pole, starts to move to the south pole, and then, after passing the south pole, returns to the north pole. Note that, the spin wave is propagating forward when the state is on the north hemisphere, and vice versa. However, at $\delta k = 0.2$, the trajectory does not pass through the south pole, and its portion below the equator becomes less than the one above the equator. Finally, when $\delta k = \delta k_c \approx 0.33$, the full trajectory is on the north hemisphere only, which indicates the disappearance of the to-and-fro motion.

Figure 5.2(d), plotted for an AC magnonic crystal with $\omega_{ac} = 0.00316$, shows a more complicated behavior, which includes a non-trivial precession of the states on the Bloch spheres. In the presented case, the resonant spin-wave wave vector is shifted to $k \approx 11$ (and 9).

5.5 Spin-wave Computing via AC Magnonic Crystal

At the exact shifted resonance (i.e., $\tilde{\xi} = 0$), Eq. (5.21) is reduced to $|SW\rangle = e^{-i\varphi_g(t)} \left\{\cos[\theta(t)/2]\,|k\rangle + \sin[\theta(t)/2]\, e^{i\phi(t)}\,|k-q\rangle\right\}$. Here, $\theta(t) \equiv \omega_R t$ and $\phi(t) \equiv \omega_{ac}t + \varphi_{ac} - \pi/2$. This state can be considered as a spin-wave "qubit", which is characterized by the polar angle $\theta(t)$ and azimuthal angle $\phi(t)$. Recall that $\omega_R(\tilde{\xi} = 0) = \gamma\Delta B_0/2 \propto I_0$; therefore, the time evolution of this "qubit" (i.e., $\theta(t)$ and $\phi(t)$) is fully controlled by the intensity and the AC modulation of the magnonic crystal. Consequently, one can manipulate this spin-wave based macroscopical "qubit" using a properly designed AC pulse. For example, Fig. 5.3(a) demonstrates that one can bring the state from the north pole to the equator on the Bloch sphere utilizing a $\pi/2$-pulse shown in Fig. 5.3(b). It is also possible to flip the spin-wave "qubit" by the π-pulse, see, e.g., Figs. 5.3(c) and 5.3(d), and more discussions in Appendix. C.3. Note that the spin-wave "qubit" controlled by the

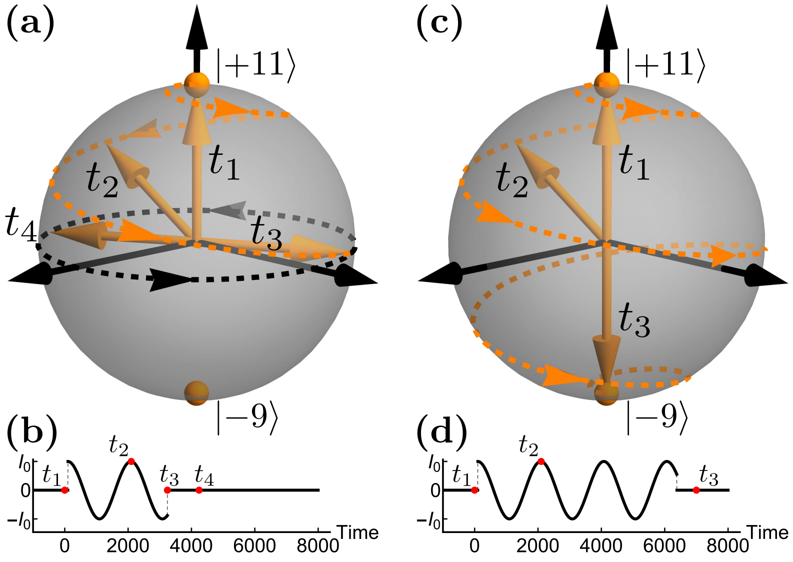

Figure 5.3: (a) Motion of the spin wave with the initial wave vector $k = 11$ on the Bloch sphere when sending (b) the AC $\pi/2$-pulse with $\omega_{ac} = 0.00316$. The dashed orange curve with arrowheads is the trajectory during the activation of the $\pi/2$-pulse, while the dashed black curve on the equator indicates the motion after t_3. Subfigure (c) shows the motion when sending (d) the π-pulse. The widths of the $\pi/2$- and π-pulse are $\pi/2\omega_R$ and π/ω_R, which are determined by the intensity of the pulse.

AC magnonic crystal has a nonzero energy mismatch $\Delta\omega_s = \omega_{ac}$. This leads to a time-dependent $\phi(t)$ and, thereby, opens a way to manipulate the azimuthal angle of this "qubit" and makes all single-qubit operations possible [64].

In principle, any N-qubit state without entanglement can be expressed as

$$\begin{aligned} |\Psi\rangle =& |\psi\rangle_1 \otimes |\psi\rangle_2 \otimes \cdots \otimes |\psi\rangle_N \\ =& \left(p_1^+|0\rangle_1 + p_1^-|1\rangle_1\right) \otimes \left(p_2^+|0\rangle_2 + p_2^-|1\rangle_2\right) \otimes \cdots \otimes \left(p_N^+|0\rangle_N + p_N^-|1\rangle_N\right); \end{aligned} \tag{5.22}$$

and in principle, one can encode it as a spin-wave state

$$|SW\rangle = \left(p_1^+|k_1\rangle + p_1^-|k_1 - q\rangle\right) + \left(p_2^+|k_2\rangle + p_2^-|k_2 - q\rangle\right) + \cdots + \left(p_N^+|k_N\rangle + p_N^-|k_N - q\rangle\right), \tag{5.23}$$

which contains N pairs of waves with different wave vectors. As long as the frequency differences of individual pairs are well separated in the frequency domain, each spin-wave pair $(|k_i\rangle, |k_i - q\rangle)$ will be controlled only by an AC pulse with the proper frequency $\omega_{ac,i}$, which satisfies the shifted resonance $\omega_{ac,i} = |\omega_s(k_i) - \omega_s(k_i - q)|$. Specifically, the time evolution of the i-th spin wave pair $p_i^+(0)|k_i\rangle + p_i^-(0)|k_i - q\rangle \rightarrow p_i^+(t)|k_i\rangle + p_i^-(t)|k_i - q\rangle$ under the AC modulation $I_{0,i}\cos(\omega_{ac,i}t + \varphi_{ac,i})$ is described by

$$\begin{pmatrix} p_i^+(t) \\ p_i^-(t) \end{pmatrix} = e^{i\varphi_{C,i}(t)} \begin{pmatrix} \cos\left[\frac{\theta_i(t)}{2}\right] e^{i\varphi_{A,i}(t)} & \sin\left[\frac{\theta_i(t)}{2}\right] e^{i\varphi_{B,i}(t)} \\ -\sin\left[\frac{\theta_i(t)}{2}\right] e^{-i\varphi_{B,i}(t)} & \cos\left[\frac{\theta_i(t)}{2}\right] e^{-i\varphi_{A,i}(t)} \end{pmatrix} \begin{pmatrix} p_i^+(0) \\ p_i^-(0) \end{pmatrix} \tag{5.24}$$

with

$$\begin{aligned} \theta_i(t) =& (\frac{\gamma \Delta B_{0,i}}{2})t \propto I_{0,i}t, \\ \varphi_{A,i}(t) =& -(\frac{\omega_{ac,i}}{2})t, \\ \varphi_{B,i}(t) =& -(\frac{\omega_{ac,i}}{2})t - \varphi_{ac,i} - \frac{\pi}{2}, \\ \varphi_{C,i}(t) =& -\Omega_i t + \varphi_{s,i}, \end{aligned} \tag{5.25}$$

and $\Omega_i = [\omega_s(k_i) + \omega_s(k_i - q)]/2$. Hence, one may anticipate that multiple spin-wave “qubits” constituted of distinct wave pairs can be manipulated simultaneously by sending the proper AC pulses with different ω_{ac} through a meander structure; one can employ this scheme to do spin-wave computing by implementing some quantum algorithms that do not require entanglement, e.g., the sophisticated quantum search discussed in Ref. [3].

5.6 Additional Remarks

Finally, we discuss the feasibility of the proposed scheme. To make the RWA valid, ω_{ac} has to be much greater than $\gamma\Delta B_0$. In addition, to minimize the higher-order effects from the spin-wave states with wave vectors $k + q$, $k \pm 2q$, $\cdots$, the inequalities of the kind $\big||\omega_s(k+q) - \omega_s(k)| - \omega_{ac}\big| \gg \gamma\Delta B_0/2$ need to be fulfilled. In particular, one may require $|\omega_s(q) - \omega_s(0)| - \omega_{ac} \gg \gamma\Delta B_0/2$. Let us take the experimental parameters in Ref. [40] as an example. In this measurement, the value of $\gamma\Delta B_0$ was $2\pi\times 11$ MHz, while $|\omega_s(q)-\omega_s(0)|$ was roughly $2\pi\times 100$ MHz. In this case, an AC modulation with ω_{ac} around $2\pi \times 50$ MHz would be suitable for the experimental studies of the shifted resonance. Spin-wave attenuation and decoherence are the two other factors that need to be considered. Let us estimate the operation time required to bring the spin-wave state from the north to the south pole. Using the same value of $\gamma\Delta B_0$, we find this time to be $2\pi/\gamma\Delta B_0 \approx 91$ ns, which is shorter than both lifetime and coherence time of spin waves in YIG (cf. Refs. [9], [10], and [11]). In the end, we estimate the length of the device. In practice, the slopes of the curves plotted in Figs. 5.2(a) and 5.2(b) are determined by the group velocities of the incident and reflected spin-wave packets, which may vary dramatically for different magnetic material and geometries. In the case of the magnetostatic spin waves studied in Ref. [40], the spin-wave group velocity $|v_g|$ was found to be about 27404 m/s. Such a spin-wave packet would perform to-and-fro motion with maximum displacement $|v_g| \times 2\pi/\gamma\Delta B_0 \approx 2.5$ mm, and therefore, the meander structure must have a size of at least 2.5 mm in order to confine this bouncing packet. In principle, the operating range of ω_{ac} can be enlarged to GHz range by fabricating a meander structure with a shorter period d, and the operation time can be further reduced by applying a bigger I_0.

We expect that, with the use of the techniques accessible nowadays, the *tunable* AC magnonic crystal can be exploited for controlling spin waves with different wave vectors. One can excite and detect many spin waves with different frequencies in a magnetic sample at the same time through one antenna setup. The tunability of the AC magnonic crystal allows one to use a single hardware (the metallic meander pattern) to simultaneously manipulate multiple spin-wave pairs in one waveguide. Each pair formed by waves with different frequencies is independently operated by a suitable AC pulse that satisfies the *shifted resonance*. As a result, the *tunable* AC magnonic crystal can serve as a new building block of the computing device studied in Ref. [13] and improve its scalability. This opens new possibilities for the spin-wave computing.

6. SUMMARY AND OUTLOOKS

To summarize, we developed a spin-wave model for van der Waals layered magnetic material $\mathrm{CoTiO_3}$ using a formalism based on the continuous macroscopic variables, i.e., the total magnetization and the Néel vector. The established semimacroscopic spin-wave description gives all four spin-wave branches in this material and agrees quantitatively well with the experimental measurement at long-wavelength limit. The developed formalism can be easily extended to a deformed magnetic system and is applicable to a generic quantum XY AFM, which provides a read-to-use model for studying the spin superfluidity transport in this type of magnetic materials. Then, we studied the spin-wave dynamics in an AFM while a spatially modulated strain is suddenly switched on for the system. We demonstrated that the periodic strain, after switching it on, acts like a *magnonic crystal* on spin waves propagating along the same direction of the modulation. The strain-induced magnonic crystal causes a continuous spin-wave scattering and leads to a *to-and-fro* motion of the spin waves that satisfy the *spatial* resonance condition. Finally, we turned our focus to a current-induced magnonic crystal in FM systems. The key advantages of the current-induced magnonic crystal include its ability to be easily switched on and off as well as its tunability, which provide a highly controllable manner for manipulating the propagation of spin waves. We explored the possibility of using a tunable AC modulated magnonic crystal for the purpose of spin-wave computing. We proposed to utilize what we called the *shifted resonance* to manipulate multiple spin-wave pairs simultaneously through a fixed hardware, namely, the metallic meander structure. We believe that this study has the potential to open up new avenues in spin-wave computing and to establish a boundary between wave computing and true quantum computation.

In future, we need to explore practical ways of implementing the proposed scheme for real computations. In addition, we anticipate that the proposed scheme will work similarly for spin-wave modes originating from the long-range magnetic dipole-dipole interactions. Therefore, we need to investigate the possibilities of pushing the limits of classical wave computing, e.g., to what extent one can use the coupled spin waves in multiple FM films to simulate an entangled qubit state.

REFERENCES

[1] S. Lloyd, “Quantum search without entanglement,” *Phys. Rev. A*, vol. 61, p. 010301, 1999.

[2] P. Knight, “Quantum information processing without entanglement,” *Science*, vol. 287, no. 5452, pp. 441–442, 2000.

[3] D. A. Meyer, “Sophisticated quantum search without entanglement,” *Phys. Rev. Lett.*, vol. 85, pp. 2014–2017, 2000.

[4] D. Ferry, R. Akis, and J. Harris, “Quantum wave processing,” *Superlattices and Microstructures*, vol. 30, no. 2, pp. 81–94, 2001.

[5] A. Patel, “Optimal database search: Waves and catalysis,” *International Journal of Quantum Information*, vol. 4, no. 05, pp. 815–825, 2006.

[6] A. Khitun, R. Ostroumov, and K. L. Wang, “Spin-wave utilization in a quantum computer,” *Phys. Rev. A*, vol. 64, p. 062304, 2001.

[7] A. V. Chumak, V. I. Vasyuchka, A. A. Serga, and B. Hillebrands, “Magnon spintronics,” *Nature Physics*, vol. 11, no. 6, pp. 453–461, 2015.

[8] H. Yuan, Y. Cao, A. Kamra, R. A. Duine, and P. Yan, “Quantum magnonics: When magnon spintronics meets quantum information science,” *Physics Reports*, vol. 965, pp. 1–74, 2022.

[9] A. A. Serga, A. V. Chumak, and B. Hillebrands, “YIG magnonics,” *Journal of Physics D: Applied Physics*, vol. 43, no. 26, p. 264002, 2010.

[10] M. Collet, O. Gladii, M. Evelt, V. Bessonov, L. Soumah, P. Bortolotti, S. O. Demokritov, Y. Henry, V. Cros, M. Bailleul, V. E. Demidov, and A. Anane, “Spin-wave propagation in ultra-thin YIG based waveguides,” *Applied Physics Letters*, vol. 110, no. 9, p. 092408, 2017.

[11] A. Mahmoud, F. Ciubotaru, F. Vanderveken, A. V. Chumak, S. Hamdioui, C. Adelmann, and S. Cotofana, “Introduction to spin wave computing,” *Journal of Applied Physics*, vol. 128, no. 16, p. 161101, 2020.

[12] G. Csaba, Ádám Papp, and W. Porod, “Perspectives of using spin waves for computing and signal processing,” *Physics Letters A*, vol. 381, no. 17, pp. 1471–1476, 2017.

[13] M. Balynsky, H. Chiang, D. Gutierrez, A. Kozhevnikov, Y. Filimonov, and A. Khitun, “Quantum computing without quantum computers: Database search and data processing using classical wave superposition,” *Journal of Applied Physics*, vol. 130, no. 16, p. 164903, 2021.

[14] P. Pirro, V. I. Vasyuchka, A. A. Serga, and B. Hillebrands, “Advances in coherent magnonics,” *Nature Reviews Materials*, vol. 6, no. 12, pp. 1114–1135, 2021.

[15] A. V. Chumak, P. Kabos, M. Wu, C. Abert, C. Adelmann, A. O. Adeyeye, J. Åkerman, F. G. Aliev, A. Anane, A. Awad, C. H. Back, A. Barman, G. E. W. Bauer, M. Becherer, E. N. Beginin, *et al.*, “Advances in magnetics roadmap on spin-wave computing,” *IEEE Transactions on Magnetics*, vol. 58, no. 6, pp. 1–72, 2022.

[16] P. Che, K. Baumgaertl, A. Kúkol’ová, C. Dubs, and D. Grundler, “Efficient wavelength conversion of exchange magnons below 100 nm by magnetic coplanar waveguides,” *Nature Communications*, vol. 11, no. 1, p. 1445, 2020.

[17] Q. Wang, R. Verba, B. Heinz, M. Schneider, O. Wojewoda, K. Davídková, K. Levchenko, C. Dubs, N. J. Mauser, M. Urbánek, P. Pirro, and A. V. Chumak, “Deeply nonlinear excitation of self-normalised exchange spin waves,” *arXiv:2207.01121*, 2022.

[18] A. Liu and A. M. Finkel’stein, “Control of spin waves by spatially modulated strain,” *Phys. Rev. B*, vol. 105, p. L020404, 2022.

[19] A. Liu and A. M. Finkel’stein, “Spin waves in layered antiferromagnets with honeycomb structure,” *Phys. Rev. B*, vol. 105, p. 214409, 2022.

[20] A. Liu and A. M. Finkel’stein, “Spin-wave dynamics controlled by tunable ac magnonic crystal,” *Phys. Rev. B (to be published).*

[21] A. Prabhakar and D. D. Stancil, *Spin Waves: Theory and Applications*, vol. 5. Springer, New York, 2009.

[22] E. B. Sonin, “Spin superfluidity and spin waves in YIG films,” *Phys. Rev. B*, vol. 95, p. 144432, 2017.

[23] G. Li, C. Sun, T. Nattermann, and V. L. Pokrovsky, “Long-wave magnons in a ferromagnetic film,” *Phys. Rev. B*, vol. 98, p. 014436, 2018.

[24] D. C. Mattis, *The Theory of Magnetism I: Statics and Dynamics*. Springer Series in Solid-State Sciences Vol. 17, Springer, New York, 2012.

[25] S. Maekawa, S. O. Valenzuela, E. Saitoh, and T. Kimura, *Spin Current*, vol. 22. Oxford University Press, Oxford, 2017.

[26] F. D. M. Haldane, “Nonlinear field theory of large-spin Heisenberg antiferromagnets: Semi-classically quantized solitons of the one-dimensional easy-axis Néel state,” *Phys. Rev. Lett.*, vol. 50, pp. 1153–1156, 1983.

[27] A. Auerbach, *Interacting Electrons and Quantum Magnetism*. Springer, New York, 2012.

[28] S. Takei, B. I. Halperin, A. Yacoby, and Y. Tserkovnyak, “Superfluid spin transport through antiferromagnetic insulators,” *Phys. Rev. B*, vol. 90, p. 094408, 2014.

[29] P. C. Hohenberg and B. I. Halperin, “Theory of dynamic critical phenomena,” *Reviews of Modern Physics*, vol. 49, no. 3, p. 435, 1977.

[30] E. Sonin, “Spin currents and spin superfluidity,” *Advances in Physics*, vol. 59, no. 3, pp. 181–255, 2010.

[31] A. Oleaga, A. Salazar, and Y. M. Bunkov, “3D-XY critical behavior of $\mathrm{CsMnF_3}$ from static and dynamic thermal properties,” *Journal of Physics: Condensed Matter*, vol. 26, no. 9, p. 096001, 2014.

[32] P. A. Joy and S. Vasudevan, “Magnetism in the layered transition-metal thiophosphates $M\mathrm{PS_3}$ ($M=$ Mn, Fe, and Ni),” *Phys. Rev. B*, vol. 46, pp. 5425–5433, 1992.

[33] A. Wildes, V. Simonet, E. Ressouche, R. Ballou, and G. McIntyre, “The magnetic properties and structure of the quasi-two-dimensional antiferromagnet $\mathrm{CoPS_3}$,” *Journal of Physics: Condensed Matter*, vol. 29, no. 45, p. 455801, 2017.

[34] P. Wadley, V. Hills, M. Shahedkhah, K. Edmonds, R. Campion, V. Novák, B. Ouladdiaf, D. Khalyavin, S. Langridge, V. Saidl, *et al.*, “Antiferromagnetic structure in tetragonal CuMnAs thin films,” *Scientific reports*, vol. 5, no. 1, pp. 1–6, 2015.

[35] D. R. Klein, D. MacNeill, Q. Song, D. T. Larson, S. Fang, M. Xu, R. A. Ribeiro, P. C. Canfield, E. Kaxiras, R. Comin, *et al.*, “Enhancement of interlayer exchange in an ultrathin two-dimensional magnet,” *Nature Physics*, vol. 15, no. 12, pp. 1255–1260, 2019.

[36] X. Cai, T. Song, N. P. Wilson, G. Clark, M. He, X. Zhang, T. Taniguchi, K. Watanabe, W. Yao, D. Xiao, *et al.*, “Atomically thin $\mathrm{CrCl_3}$: An in-plane layered antiferromagnetic insulator,” *Nano letters*, vol. 19, no. 6, pp. 3993–3998, 2019.

[37] H. H. Kim, B. Yang, S. Li, S. Jiang, C. Jin, Z. Tao, G. Nichols, F. Sfigakis, S. Zhong, C. Li, *et al.*, “Evolution of interlayer and intralayer magnetism in three atomically thin chromium trihalides,” *Proceedings of the National Academy of Sciences*, vol. 116, no. 23, pp. 11131–11136, 2019.

[38] B. Yuan, I. Khait, G.-J. Shu, F. C. Chou, M. B. Stone, J. P. Clancy, A. Paramekanti, and Y.-J. Kim, “Dirac magnons in a honeycomb lattice quantum XY magnet $\mathrm{CoTiO_3}$,” *Phys. Rev. X*, vol. 10, p. 011062, 2020.

[39] A. V. Chumak, V. S. Tiberkevich, A. D. Karenowska, A. A. Serga, J. F. Gregg, A. N. Slavin, and B. Hillebrands, “All-linear time reversal by a dynamic artificial crystal,” *Nature Communications*, vol. 1, no. 1, p. 141, 2010.

[40] A. D. Karenowska, J. F. Gregg, V. S. Tiberkevich, A. N. Slavin, A. V. Chumak, A. A. Serga, and B. Hillebrands, “Oscillatory energy exchange between waves coupled by a dynamic artificial crystal,” *Phys. Rev. Lett.*, vol. 108, p. 015505, 2012.

[41] A. V. Chumak, A. A. Serga, and B. Hillebrands, “Magnonic crystals for data processing,” *Journal of Physics D: Applied Physics*, vol. 50, no. 24, p. 244001, 2017.

[42] C. Kittel, “Interaction of spin waves and ultrasonic waves in ferromagnetic crystals,” *Phys. Rev.*, vol. 110, pp. 836–841, 1958.

[43] H. Bömmel and K. Dransfeld, “Excitation of hypersonic waves by ferromagnetic resonance,” *Phys. Rev. Lett.*, vol. 3, pp. 83–84, 1959.

[44] M. Pomerantz, “Excitation of spin-wave resonance by microwave phonons,” *Phys. Rev. Lett.*, vol. 7, pp. 312–313, 1961.

[45] H. Matthews and F. R. Morgenthaler, “Phonon-pumped spin-wave instabilities,” *Phys. Rev. Lett.*, vol. 13, pp. 614–616, 1964.

[46] E. G. Spencer and R. C. LeCraw, “Magnetoacoustic resonance in yttrium iron garnet,” *Phys. Rev. Lett.*, vol. 1, pp. 241–243, 1958.

[47] R. L. Comstock and B. A. Auld, “Parametric coupling of the magnetization and strain in a ferrimagnet. I. Parametric excitation of magnetostatic and elastic modes,” *Journal of Applied Physics*, vol. 34, no. 5, pp. 1461–1464, 1963.

[48] R. L. Comstock, “Parametric coupling of the magnetization and strain in a ferrimagnet. II. Parametric excitation of magnetic and elastic plane waves,” *Journal of Applied Physics*, vol. 34, no. 5, pp. 1465–1468, 1963.

[49] R. I. Joseph and E. Schlömann, “Dependence of the phonon-instability threshold for parallel pumping on crystal orientation and magnetic fieldstrength,” *Journal of Applied Physics*, vol. 41, no. 6, pp. 2513–2520, 1970.

[50] P. Chowdhury, A. Jander, and P. Dhagat, “Nondegenerate parametric pumping of spin waves by acoustic waves,” *IEEE Magnetics Letters*, vol. 8, pp. 1–4, 2017.

[51] M. Weiler, L. Dreher, C. Heeg, H. Huebl, R. Gross, M. S. Brandt, and S. T. B. Goennenwein, "Elastically driven ferromagnetic resonance in nickel thin films," *Phys. Rev. Lett.*, vol. 106, p. 117601, 2011.

[52] L. Dreher, M. Weiler, M. Pernpeintner, H. Huebl, R. Gross, M. S. Brandt, and S. T. B. Goennenwein, "Surface acoustic wave driven ferromagnetic resonance in nickel thin films: Theory and experiment," *Phys. Rev. B*, vol. 86, p. 134415, 2012.

[53] J. V. Jäger, A. V. Scherbakov, B. A. Glavin, A. S. Salasyuk, R. P. Campion, A. W. Rushforth, D. R. Yakovlev, A. V. Akimov, and M. Bayer, "Resonant driving of magnetization precession in a ferromagnetic layer by coherent monochromatic phonons," *Phys. Rev. B*, vol. 92, p. 020404, 2015.

[54] P. G. Gowtham, T. Moriyama, D. C. Ralph, and R. A. Buhrman, "Traveling surface spin-wave resonance spectroscopy using surface acoustic waves," *Journal of Applied Physics*, vol. 118, no. 23, p. 233910, 2015.

[55] M. Xu, K. Yamamoto, J. Puebla, K. Baumgaertl, B. Rana, K. Miura, H. Takahashi, D. Grundler, S. Maekawa, and Y. Otani, "Nonreciprocal surface acoustic wave propagation via magneto-rotation coupling," *Science Advances*, vol. 6, no. 32, p. eabb1724, 2020.

[56] Y. Li, C. Zhao, W. Zhang, A. Hoffmann, and V. Novosad, "Advances in coherent coupling between magnons and acoustic phonons," *APL Materials*, vol. 9, no. 6, p. 060902, 2021.

[57] F. Chen, X. Ge, W. Luo, R. Xing, S. Liang, X. Yang, L. You, R. Xiong, Y. Otani, and Y. Zhang, "Strain-induced megahertz oscillation and stable velocity of an antiferromagnetic domain wall," *Phys. Rev. Applied*, vol. 15, p. 014030, 2021.

[58] A. V. Chumak, P. Dhagat, A. Jander, A. A. Serga, and B. Hillebrands, "Reverse doppler effect of magnons with negative group velocity scattered from a moving bragg grating," *Phys. Rev. B*, vol. 81, p. 140404, 2010.

[59] M. Grifoni and P. Hänggi, "Driven quantum tunneling," *Physics Reports*, vol. 304, no. 5, pp. 229–354, 1998.

[60] M. Bukov, L. D'Alessio, and A. Polkovnikov, "Universal high-frequency behavior of periodically driven systems: from dynamical stabilization to Floquet engineering," *Advances in Physics*, vol. 64, no. 2, pp. 139–226, 2015.

[61] M. Holthaus, "Floquet engineering with quasienergy bands of periodically driven optical lattices," *Journal of Physics B: Atomic, Molecular and Optical Physics*, vol. 49, no. 1, p. 013001, 2015.

[62] T. Oka and S. Kitamura, "Floquet engineering of quantum materials," *Annual Review of Condensed Matter Physics*, vol. 10, no. 1, pp. 387–408, 2019.

[63] C. Cohen-Tannoudji, B. Diu, and F. Laloë, *Quantum Mechanics, Volume 1: Basic Concepts, Tools, and Applications*. Wiley-VCH, Hoboken, 2020.

[64] M. A. Nielsen and I. Chuang, *Quantum Computation and Quantum Information*. Cambridge University Press, Cambridge, 2010.

[65] R. Nicklow, N. Wakabayashi, and H. G. Smith, "Lattice dynamics of pyrolytic graphite," *Phys. Rev. B*, vol. 5, pp. 4951–4962, 1972.

[66] N. Wakabayashi, H. G. Smith, and R. M. Nicklow, "Lattice dynamics of hexagonal $\mathrm{MoS_2}$ studied by neutron scattering," *Phys. Rev. B*, vol. 12, pp. 659–663, 1975.

[67] E. W. Weisstein, Mathieu Function, in *MathWorld–A Wolfram Web Resource*, `https://mathworld.wolfram.com/MathieuFunction.html`.

[68] Wolfram Research, NDSolve, Wolfram Language function, `https://reference.wolfram.com/language/ref/NDSolve.html`.

[69] P. B. Visscher, "A fast explicit algorithm for the time-dependent Schrödinger equation," *Computers in Physics*, vol. 5, no. 6, pp. 596–598, 1991.

APPENDIX A

SUPPLEMENTAL INFORMATION FOR CHAPTER 3[*]

This appendix is dedicated to providing readers with the additional mathematical details that were not included in Chapter 3. Here you will find the step-by-step derivations of equations of motion for $\boldsymbol{m}$ and $\boldsymbol{l}$ with and without a lattice deformation as well as the detailed calculations to get the solutions (3.32) and (3.33).

A.1 Derivation of Equations of Motion for m and l Without Deformation

In this appendix, we show how to derive Eqs. (3.5)-(3.10) and (3.17)-(3.22) in Chapter 3. Similar to what were discussed in Chapter 3, for the case when site i is on the B sublattice, Eqs. (3.3) and (3.4) are modified as follows: (i) $A \leftrightarrow B$; (ii) $\frac{\partial}{\partial z} \to -\frac{\partial}{\partial z}$. Finally, incorporating the gradient expansion terms in Eq. (3.2), one obtains the equations of motion for the spin components $\boldsymbol{S}_{A/B}$:

$$\begin{aligned}\frac{dS^x_{A/B}}{dt} \approx & 3J_\parallel S^z_{A/B} S^y_{B/A} + 3J_\perp [S^z_{A/B}(\bar{S}^y_{B/A} + 2\bar{S}^y_{A/B}) - S^y_{A/B}(\bar{S}^z_{B/A} + 2\bar{S}^z_{A/B})] \\ & + \frac{3}{4} J_\parallel S^z_{A/B} \nabla^2_- S^y_{B/A} + 3J_\perp \Big\{ S^z_{A/B}[\pm \frac{\partial \bar{S}^y_{B/A}}{\partial z} + \frac{1}{4}\nabla^2_+(\bar{S}^y_{B/A} + 2\bar{S}^y_{A/B})] \\ & - S^y_{A/B}[\pm \frac{\partial \bar{S}^z_{B/A}}{\partial z} + \frac{1}{4}\nabla^2_+(\bar{S}^z_{B/A} + 2\bar{S}^z_{A/B})]\Big\}, \end{aligned} \tag{A.1}$$

$$\begin{aligned}\frac{dS^y_{A/B}}{dt} \approx & -3J_\parallel S^z_{A/B} S^x_{B/A} + 3J_\perp [S^x_{A/B}(\bar{S}^z_{B/A} + 2\bar{S}^z_{A/B}) - S^z_{A/B}(\bar{S}^x_{B/A} + 2\bar{S}^x_{A/B})] \\ & - \frac{3}{4} J_\parallel S^z_{A/B} \nabla^2_- S^x_{B/A} + 3J_\perp \Big\{ S^x_{A/B}[\pm \frac{\partial \bar{S}^z_{B/A}}{\partial z} + \frac{1}{4}\nabla^2_+(\bar{S}^z_{B/A} + 2\bar{S}^z_{A/B})] \\ & - S^z_{A/B}[\pm \frac{\partial \bar{S}^x_{B/A}}{\partial z} + \frac{1}{4}\nabla^2_+(\bar{S}^x_{B/A} + 2\bar{S}^x_{A/B})]\Big\}, \end{aligned} \tag{A.2}$$

---

[*] Reprinted with permission from “Spin waves in layered antiferromagnets with honeycomb structure” by Ankang Liu and Alexander M. Finkel’stein, 2022. Phys. Rev. B, 105, 214409, Copyright 2022 by American Physical Society.

and

$$\begin{aligned}\frac{dS^z_{A/B}}{dt} \approx & 3J_\parallel(S^y_{A/B}S^x_{B/A} - S^x_{A/B}S^y_{B/A}) + 3J_\perp[S^y_{A/B}(\bar{S}^x_{B/A} + 2\bar{S}^x_{A/B}) - S^x_{A/B}(\bar{S}^y_{B/A} + 2\bar{S}^y_{A/B})] \\ & + \frac{3}{4}J_\parallel(S^y_{A/B}\nabla^2_- S^x_{B/A} - S^x_{A/B}\nabla^2_- S^y_{B/A}) + 3J_\perp\Big\{S^y_{A/B}[\pm\frac{\partial\bar{S}^x_{B/A}}{\partial z} + \frac{1}{4}\nabla^2_+(\bar{S}^x_{B/A} + 2\bar{S}^x_{A/B})] \\ & - S^x_{A/B}[\frac{\pm\partial\bar{S}^y_{B/A}}{\partial z} + \frac{1}{4}\nabla^2_+(\bar{S}^y_{B/A} + 2\bar{S}^y_{A/B})]\Big\}. \end{aligned} \tag{A.3}$$

Here, we eventually dropped the site index i in the spin operators, assuming from now on that $\boldsymbol{S}_{A/B}$ are space- and time-dependent variables $\boldsymbol{S}_{A/B}(\boldsymbol{r}, t)$. For the spatial derivatives, we have also introduced a short notation, $\nabla^2_\pm \equiv \nabla^2 \pm \frac{\partial^2}{\partial z^2}$. The equations of motion for $\bar{\boldsymbol{S}}_{A/B}$ could be obtained through the exchange $\boldsymbol{S}_{A/B} \leftrightarrow \bar{\boldsymbol{S}}_{A/B}$ in the above equations.

Next, we define the total magnetization $\boldsymbol{m}_{A/B} \equiv \boldsymbol{S}_{A/B} + \bar{\boldsymbol{S}}_{A/B}$ and the Néel vector $\boldsymbol{l}_{A/B} \equiv \boldsymbol{S}_{A/B} - \bar{\boldsymbol{S}}_{A/B}$ for the A/B sublattices, see e.g., Ref. [27]. Note that in a simple Néel AFM the vectors $\boldsymbol{m}$ and $\boldsymbol{l}$ are orthogonal, $\boldsymbol{m}_{A/B} \cdot \boldsymbol{l}_{A/B} = 0$. In the following part of this appendix, $\boldsymbol{m}_{A/B}$ and $\boldsymbol{l}_{A/B}$ will be considered as classical variables rather than the quantum operators. The resulting equations of motion for $\boldsymbol{m}_A$ and $\boldsymbol{l}_A$ are

$$\begin{aligned}\frac{dm^x_A}{dt} \approx & \frac{3}{2}J_\parallel(m^z_A m^y_B + \underline{l^z_A l^y_B}) + \frac{3}{2}J_\perp[(m^z_A m^y_B - m^y_A m^z_B) - (\underline{l^z_A l^y_B - l^y_A l^z_B})] \\ & + \frac{3}{8}J_\parallel(m^z_A \nabla^2_- m^y_B + l^z_A \nabla^2_- l^y_B) + \frac{3}{8}J_\perp\Big\{[m^z_A(\nabla^2_+ + 4\frac{\partial}{\partial z})m^y_B - l^z_A(\nabla^2_+ + 4\frac{\partial}{\partial z})l^y_B \\ & + 2m^z_A\nabla^2_+ m^y_A - 2l^z_A\nabla^2_+ l^y_A] - [m^y_A(\nabla^2_+ + 4\frac{\partial}{\partial z})m^z_B - \underline{l^y_A(\nabla^2_+ + 4\frac{\partial}{\partial z})l^z_B} \\ & + 2m^y_A\nabla^2_+ m^z_A - \underline{2l^y_A\nabla^2_+ l^z_A}]\Big\}, \end{aligned} \tag{A.4}$$

$$\begin{aligned}\frac{dm^y_A}{dt} \approx & -\frac{3}{2}J_\parallel(m^z_A m^x_B + \underline{l^z_A l^x_B}) + \frac{3}{2}J_\perp[(m^x_A m^z_B - m^z_A m^x_B) - (\underline{l^x_A l^z_B - l^z_A l^x_B})] \\ & - \frac{3}{8}J_\parallel(m^z_A \nabla^2_- m^x_B + l^z_A \nabla^2_- l^x_B) + \frac{3}{8}J_\perp\Big\{[m^x_A(\nabla^2_+ + 4\frac{\partial}{\partial z})m^z_B - \underline{l^x_A(\nabla^2_+ + 4\frac{\partial}{\partial z})l^z_B} \\ & + 2m^x_A\nabla^2_+ m^z_A - \underline{2l^x_A\nabla^2_+ l^z_A}] - [m^z_A(\nabla^2_+ + 4\frac{\partial}{\partial z})m^x_B - l^z_A(\nabla^2_+ + 4\frac{\partial}{\partial z})l^x_B \\ & + 2m^z_A\nabla^2_+ m^x_A - 2l^z_A\nabla^2_+ l^x_A]\Big\}, \end{aligned} \tag{A.5}$$

$$
\begin{aligned}
\frac{dm^z_A}{dt} \approx & \frac{3}{2}J_\parallel[(m^y_A m^x_B + \underline{l^y_A l^x_B}) - (m^x_A m^y_B + \underline{l^x_A l^y_B})] + \frac{3}{2}J_\perp[(m^y_A m^x_B - m^x_A m^y_B) - (\underline{l^y_A l^x_B - l^x_A l^y_B})] \\
& + \frac{3}{8}J_\parallel[(m^y_A \nabla^2_- m^x_B + \underline{l^y_A \nabla^2_- l^x_B}) - (m^x_A \nabla^2_- m^y_B + \underline{l^x_A \nabla^2_- l^y_B})] + \frac{3}{8}J_\perp\Big\{[m^y_A(\nabla^2_+ + 4\frac{\partial}{\partial z})m^x_B \\
& - \underline{l^y_A(\nabla^2_+ + 4\frac{\partial}{\partial z})l^x_B} + 2m^y_A\nabla^2_+ m^x_A - \underline{2l^y_A\nabla^2_+ l^x_A}] - [m^x_A(\nabla^2_+ + 4\frac{\partial}{\partial z})m^y_B \\
& - \underline{l^x_A(\nabla^2_+ + 4\frac{\partial}{\partial z})l^y_B} + 2m^x_A\nabla^2_+ m^y_A - \underline{2l^x_A\nabla^2_+ l^y_A}]\Big\},
\end{aligned}
\tag{A.6}
$$

$$
\begin{aligned}
\frac{dl^x_A}{dt} \approx & \frac{3}{2}J_\parallel(\underline{m^z_A l^y_B} + l^z_A m^y_B) + \frac{3}{2}J_\perp[(l^z_A m^y_B - \underline{l^y_A m^z_B}) + (l^z_B m^y_A - \underline{l^y_B m^z_A}) + 4(l^z_A m^y_A - \underline{l^y_A m^z_A})] \\
& + \frac{3}{8}J_\parallel(m^z_A\nabla^2_- l^y_B + l^z_A\nabla^2_- m^y_B) + \frac{3}{8}J_\perp\Big\{[l^z_A(\nabla^2_+ + 4\frac{\partial}{\partial z})m^y_B - m^z_A(\nabla^2_+ + 4\frac{\partial}{\partial z})l^y_B \\
& + 2l^z_A\nabla^2_+ m^y_A - 2m^z_A\nabla^2_+ l^y_A] - [\underline{l^y_A(\nabla^2_+ + 4\frac{\partial}{\partial z})m^z_B} - m^y_A(\nabla^2_+ + 4\frac{\partial}{\partial z})l^z_B + \underline{2l^y_A\nabla^2_+ m^z_A} \\
& - 2m^y_A\nabla^2_+ l^z_A]\Big\},
\end{aligned}
\tag{A.7}
$$

$$
\begin{aligned}
\frac{dl^y_A}{dt} \approx & -\frac{3}{2}J_\parallel(\underline{m^z_A l^x_B} + l^z_A m^x_B) + \frac{3}{2}J_\perp[(\underline{l^x_A m^z_B} - l^z_A m^x_B) + (\underline{l^x_B m^z_A} - l^z_B m^x_A) + 4(\underline{l^x_A m^z_A} - l^z_A m^x_A)] \\
& - \frac{3}{8}J_\parallel(m^z_A\nabla^2_- l^x_B + l^z_A\nabla^2_- m^x_B) + \frac{3}{8}J_\perp\Big\{\underline{[l^x_A(\nabla^2_+ + 4\frac{\partial}{\partial z})m^z_B} - m^x_A(\nabla^2_+ + 4\frac{\partial}{\partial z})l^z_B \\
& + \underline{2l^x_A\nabla^2_+ m^z_A} - 2m^x_A\nabla^2_+ l^z_A] - [l^z_A(\nabla^2_+ + 4\frac{\partial}{\partial z})m^x_B - m^z_A(\nabla^2_+ + 4\frac{\partial}{\partial z})l^x_B + 2l^z_A\nabla^2_+ m^x_A \\
& - 2m^z_A\nabla^2_+ l^x_A]\Big\},
\end{aligned}
\tag{A.8}
$$

and

$$
\begin{aligned}
\frac{dl^z_A}{dt} \approx & \underline{\frac{3}{2}J_\parallel[(m^y_A l^x_B + l^y_A m^x_B) - (m^x_A l^y_B + l^x_A m^y_B)] + \frac{3}{2}J_\perp[(l^y_A m^x_B - l^x_A m^y_B) + (l^y_B m^x_A - l^x_B m^y_A)} \\
& + \underline{4(l^y_A m^x_A - l^x_A m^y_A)]} + \frac{3}{8}J_\parallel[(m^y_A\nabla^2_- l^x_B + \underline{l^y_A\nabla^2_- m^x_B}) - (m^x_A\nabla^2_- l^y_B + \underline{l^x_A\nabla^2_- m^y_B})] \\
& + \frac{3}{8}J_\perp\Big\{[\underline{l^y_A(\nabla^2_+ + 4\frac{\partial}{\partial z})m^x_B} - m^y_A(\nabla^2_+ + 4\frac{\partial}{\partial z})l^x_B + \underline{2l^y_A\nabla^2_+ m^x_A} - 2m^y_A\nabla^2_+ l^x_A] \\
& - [\underline{l^x_A(\nabla^2_+ + 4\frac{\partial}{\partial z})m^y_B} - m^x_A(\nabla^2_+ + 4\frac{\partial}{\partial z})l^y_B + \underline{2l^x_A\nabla^2_+ m^y_A} - 2m^x_A\nabla^2_+ l^y_A]\Big\}.
\end{aligned}
\tag{A.9}
$$

To get the equations of motion for $\boldsymbol{m}_B$ and $\boldsymbol{l}_B$, one just needs to apply (i) $A \leftrightarrow B$ and (ii) $\frac{\partial}{\partial z} \rightarrow$

$-\frac{\partial}{\partial z}$ in Eqs. (A.4)-(A.9).

At this stage, one could argue that only the *underlined* terms in Eqs. (A.4)-(A.9) have to be kept when discussing the *linearized* dynamics of this system. The reason is that in the equilibrium $\boldsymbol{m}_A = \boldsymbol{m}_B = 0$. Hence all terms quadratic in m have to be ignored. Furthermore, the equilibrium positions of vectors $\boldsymbol{l}_A$ and $\boldsymbol{l}_B$ are limited to the xy plane, i.e., $l^z_A = l^z_B = 0$. Therefore, all terms containing a product of l^z and any component of $\boldsymbol{m}$ have to be ignored. Finally, terms containing derivatives may coexist only with $l^{x,y}$, but not with l^z or components of $\boldsymbol{m}$. All this limits the linearized dynamics to the underlined terms only.

Next, one could notice that the equations of motion for vectors in the sublattices A and B differ only by the terms containing $\pm\frac{\partial}{\partial z}$. To derive the equations which describe the two low-energy branches of magnons, we ignore the difference in the dynamics of the A and B sublattices, and will proceed with the approximation when $\boldsymbol{m}_A = \boldsymbol{m}_B = \boldsymbol{m}$ and $\boldsymbol{l}_A = \boldsymbol{l}_B = \boldsymbol{l}$. In result, Eqs. (3.5)-(3.10) are obtained.

To derive the equations of motion for the two opticlike branches, we perturb the spins on A and B lattices oppositely with respect to each other. With this in mind, we adopt the expansions $\boldsymbol{m}_{A/B} = \pm(\delta m^x \hat{x} + \delta m^y \hat{y} + \delta m^z \hat{z})$ and $\boldsymbol{l}_{A/B} = 2\tilde{S}\hat{x} \pm (\delta l^x \hat{x} + \delta l^y \hat{y} + \delta l^z \hat{z})$, where $2\tilde{S}\hat{x}$ is the equilibrium Néel vector. Next, we substitute the expansions in $\delta m^{x,y,x}$ and $\delta l^{x,y,x}$ into Eqs. (A.4) - (A.9), and keep there only the linear terms. We again neglected $\pm\frac{\partial}{\partial z}$-terms in Eqs. (A.4)-(A.9) and, eventually, arrive to Eqs. (3.17)-(3.22).

A.2 Equations for E, a, and χ_{a,b_1,b_2}

The procedure here is rather straightforward. We substitute the ansatz Eq. (3.31) into the eigenvalue equation $H^+\tilde{\psi}_1 = E\tilde{\sigma}_3\tilde{\psi}_1$, expand χ_a, χ_{b_1}, and χ_{b_2} around 0, and take the real parts of the equation. As a result, we get

$$\begin{aligned} &a\Big\{[\mathrm{Im}(B_k) + \mathrm{Re}(B_k)(\chi_{b_1} - \chi_a)] - C_k\chi_a + [\mathrm{Im}(G^+_k) + \mathrm{Re}(G^+_k)(\chi_{b_2} - \chi_a)]\Big\} \\ &+ \frac{1}{8a}\Big\{[\mathrm{Im}(B_k) + \mathrm{Re}(B_k)(\chi_{b_1} - \chi_a)] + C_k\chi_a - [\mathrm{Im}(G^+_k) + \mathrm{Re}(G^+_k)(\chi_{b_2} - \chi_a)]\Big\} \approx 0, \end{aligned}$$

$$
\begin{aligned}
&a\Big\{[\mathrm{Im}(B_k)+\mathrm{Re}(B_k)\chi_{b_2}]+C_k\chi_a+[\mathrm{Im}(G_k^+)+\mathrm{Re}(G_k^+)\chi_{b_1}]\Big\}\\
&+\frac{1}{8a}\Big\{-[\mathrm{Im}(B_k)+\mathrm{Re}(B_k)\chi_{b_2}]+C_k\chi_a+[\mathrm{Im}(G_k^+)+\mathrm{Re}(G_k^+)\chi_{b_1}]\Big\}\approx 0,\\
&a\Big\{-[\mathrm{Im}(B_k)+\mathrm{Re}(B_k)(\chi_{b_1}-\chi_a)]+C_k(\chi_{b_2}-\chi_{b_1})-[\mathrm{Im}(G_k^+)+\mathrm{Re}(G_k^+)\chi_{b_1}]\Big\}\\
&+\frac{1}{8a}\Big\{-[\mathrm{Im}(B_k)+\mathrm{Re}(B_k)(\chi_{b_1}-\chi_a)]-C_k(\chi_{b_2}-\chi_{b_1})+[\mathrm{Im}(G_k^+)+\mathrm{Re}(G_k^+)\chi_{b_1}]\Big\}\approx 0,\\
&a\Big\{-[\mathrm{Im}(B_k)+\mathrm{Re}(B_k)\chi_{b_2}]-C_k(\chi_{b_2}-\chi_{b_1})-[\mathrm{Im}(G_k^+)+\mathrm{Re}(G_k^+)(\chi_{b_2}-\chi a)]\Big\}\\
&+\frac{1}{8a}\Big\{[\mathrm{Im}(B_k)+\mathrm{Re}(B_k)\chi_{b_2}]-C_k(\chi_{b_2}-\chi_{b_1})-[\mathrm{Im}(G_k^+)+\mathrm{Re}(G_k^+)(\chi_{b_2}-\chi a)]\Big\}\approx 0.
\end{aligned}
\tag{A.10}
$$

As for the imaginary parts, we find

$$
\begin{aligned}
&a[A_k+\mathrm{Re}(B_k)+C_k+\mathrm{Re}(G_k^+)]+\frac{1}{8a}[A_k+\mathrm{Re}(B_k)-C_k-\mathrm{Re}(G_k^+)]\approx E(a+\frac{1}{8a}),\\
&a[A_k+\mathrm{Re}(B_k)+C_k+\mathrm{Re}(G_k^+)]-\frac{1}{8a}[A_k+\mathrm{Re}(B_k)-C_k-\mathrm{Re}(G_k^+)]\approx E(-a+\frac{1}{8a}).
\end{aligned}
\tag{A.11}
$$

Finally, by solving Eqs. (A.10) and (A.11), we obtain the solution Eqs. (3.32) and (3.33).

A.3 Derivation of Equations of Motion for m and l in the Presence of Deformation

In this appendix, we derive Eqs. (3.41) and (3.42). Following the discussion in Section 3.5 and considering the change in the exchange coupling constants according to Eq. (3.40), the deformed term $\sum_{\delta_1}(\delta J_{\parallel}^{\delta_1})S_i^z S_{i+\delta_1}^y$ in Eq. (3.2) becomes

$$
\begin{aligned}
\sum_{\delta_1}(\delta J_{\parallel}^{\delta_1})S_i^z S_{i+\delta_1}^y =& S_{iA}^z S_{iB}^y \sum_{\delta_1}(\delta J_{\parallel}^{\delta_1}) + S_{iA}^z[\delta J_{\parallel}^{\delta_{1,1}}\frac{\partial S_{iB}^y}{\partial x}+\delta J_{\parallel}^{\delta_{1,2}}(-\frac{1}{2}\frac{\partial S_{iB}^y}{\partial x}+\frac{\sqrt{3}}{2}\frac{\partial S_{iB}^y}{\partial y})\\
&+\delta J_{\parallel}^{\delta_{1,3}}(-\frac{1}{2}\frac{\partial S_{iB}^y}{\partial x}-\frac{\sqrt{3}}{2}\frac{\partial S_{iB}^y}{\partial y})]+\cdots\\
\approx&\frac{3}{2}g_1(\epsilon_{xx}+\epsilon_{yy})S_{iA}^z S_{iB}^y+\frac{3}{4}g_1 S_{iA}^z(\boldsymbol{d}\cdot\boldsymbol{\nabla})S_{iB}^y.
\end{aligned}
\tag{A.12}
$$

Here, it was assumed that site i was located on the A sublattice. The vector $\boldsymbol{d}=(\epsilon_{xx}-\epsilon_{yy},-2\epsilon_{xy},0)$ describes the vector-type coupling of the deformed honeycomb lattice with the spin-wave excitations. For the case $A \to B$ the following changes should be made: (i) $A \leftrightarrow B$; (ii) $\boldsymbol{d} \to -\boldsymbol{d}$.

The out-of-plane exchange interactions could be considered similarly to the in-plane ones. Like g_1, there is a new coefficient $g_2 \equiv \frac{1}{c}\frac{\partial J_\perp}{\partial c}$ which describes the sensitivity to the *inter*-plane deformation. In addition, there appears a new vector $\boldsymbol{e}$ describing the vector coupling of the out-of-plane deformations with the spin waves. In terms of the strain tensor, components of $\boldsymbol{e}$ could be found as follows: $\boldsymbol{e} = \big(-(\epsilon_{xx}-\epsilon_{yy}) + 4\epsilon_{xz}, 2\epsilon_{xy} + 4\epsilon_{yz}, 2(\epsilon_{xx}+\epsilon_{yy}+2\epsilon_{zz})\big)$. Finally, we obtain a system of equations describing the spin dynamics in the presence of the lattice deformations

$$\begin{aligned}\frac{dS^x_{A/B}}{dt} \approx & (\cdots) + \frac{3}{2}g_1(\epsilon_{xx}+\epsilon_{yy})S^z_{A/B}S^y_{B/A} + \frac{3}{2}g_2(\epsilon_{xx}+\epsilon_{yy}+2\epsilon_{zz})[(S^z_{A/B}\bar{S}^y_{B/A} + 2S^z_{A/B}\bar{S}^y_{A/B}) \\ & - (S^y_{A/B}\bar{S}^z_{B/A} + 2S^y_{A/B}\bar{S}^z_{A/B})] + \frac{3}{4}g_1 S^z_{A/B}(\pm\boldsymbol{d}\cdot\boldsymbol{\nabla})S^y_{B/A} + \frac{3}{4}g_2[S^z_{A/B}(\pm\boldsymbol{e}\cdot\boldsymbol{\nabla})\bar{S}^y_{B/A} \\ & - S^y_{A/B}(\pm\boldsymbol{e}\cdot\boldsymbol{\nabla})\bar{S}^z_{B/A}],\end{aligned} \tag{A.13}$$

$$\begin{aligned}\frac{dS^y_{A/B}}{dt} \approx & (\cdots) - \frac{3}{2}g_1(\epsilon_{xx}+\epsilon_{yy})S^z_{A/B}S^x_{B/A} + \frac{3}{2}g_2(\epsilon_{xx}+\epsilon_{yy}+2\epsilon_{zz})[(S^x_{A/B}\bar{S}^z_{B/A} + 2S^x_{A/B}\bar{S}^z_{A/B}) \\ & - (S^z_{A/B}\bar{S}^x_{B/A} + 2S^z_{A/B}\bar{S}^x_{A/B})] - \frac{3}{4}g_1 S^z_{A/B}(\pm\boldsymbol{d}\cdot\boldsymbol{\nabla})S^x_{B/A} + \frac{3}{4}g_2[S^x_{A/B}(\pm\boldsymbol{e}\cdot\boldsymbol{\nabla})\bar{S}^z_{B/A} \\ & - S^z_{A/B}(\pm\boldsymbol{e}\cdot\boldsymbol{\nabla})\bar{S}^x_{B/A}],\end{aligned} \tag{A.14}$$

and

$$\begin{aligned}\frac{dS^z_{A/B}}{dt} \approx & (\cdots) + \frac{3}{2}g_1(\epsilon_{xx}+\epsilon_{yy})(S^y_{A/B}S^x_{B/A} - S^x_{A/B}S^y_{B/A}) + \frac{3}{2}g_2(\epsilon_{xx}+\epsilon_{yy}+2\epsilon_{zz})[(S^y_{A/B}\bar{S}^x_{B/A} \\ & + 2S^y_{A/B}\bar{S}^x_{A/B}) - (S^x_{A/B}\bar{S}^y_{B/A} + 2S^x_{A/B}\bar{S}^y_{A/B})] + \frac{3}{4}g_1[S^y_{A/B}(\pm\boldsymbol{d}\cdot\boldsymbol{\nabla})S^x_{B/A} \\ & - S^x_{A/B}(\pm\boldsymbol{d}\cdot\boldsymbol{\nabla})S^y_{B/A}] + \frac{3}{4}g_2[S^y_{A/B}(\pm\boldsymbol{e}\cdot\boldsymbol{\nabla})\bar{S}^x_{B/A} - S^x_{A/B}(\pm\boldsymbol{e}\cdot\boldsymbol{\nabla})\bar{S}^y_{B/A}].\end{aligned} \tag{A.15}$$

Here, $(\cdots)$ represents all the terms on the right hand side of Eqs. (A.1), (A.2), and (A.3) without considering the deformation in the system. Again, the equations of motion for $\bar{\boldsymbol{S}}_{A/B}$ could be obtained through the exchange $\boldsymbol{S}_{A/B} \leftrightarrow \bar{\boldsymbol{S}}_{A/B}$ in Eqs. (A.13)-(A.15).

In terms of the macroscopic quantities $\boldsymbol{m}_{A/B}$ and $\boldsymbol{l}_{A/B}$, the equations describing the spin dynamics are

$$\begin{aligned}\frac{dm_A^x}{dt} \approx&(\cdots) + \frac{3}{4}g_1(\epsilon_{xx}+\epsilon_{yy})(m_A^z m_B^y + \underline{l_A^z l_B^y}) + \frac{3}{4}g_2(\epsilon_{xx}+\epsilon_{yy}+2\epsilon_{zz})[(m_A^z m_B^y - m_A^y m_B^z)\\ &-(\underline{l_A^z l_B^y - l_A^y l_B^z})] + \frac{3}{8}g_1[m_A^z(\boldsymbol{d}\cdot\boldsymbol{\nabla})m_B^y + l_A^z(\boldsymbol{d}\cdot\boldsymbol{\nabla})l_B^y] + \frac{3}{8}g_2\Big\{[m_A^z(\boldsymbol{e}\cdot\boldsymbol{\nabla})m_B^y\\ &-m_A^y(\boldsymbol{e}\cdot\boldsymbol{\nabla})m_B^z] - [l_A^z(\boldsymbol{e}\cdot\boldsymbol{\nabla})l_B^y - \underline{l_A^y(\boldsymbol{e}\cdot\boldsymbol{\nabla})l_B^z}]\Big\},\end{aligned} \tag{A.16}$$

$$\begin{aligned}\frac{dm_A^y}{dt} \approx&(\cdots) - \frac{3}{4}g_1(\epsilon_{xx}+\epsilon_{yy})(m_A^z m_B^x + \underline{l_A^z l_B^x}) + \frac{3}{4}g_2(\epsilon_{xx}+\epsilon_{yy}+2\epsilon_{zz})[(m_A^x m_B^z - m_A^z m_B^x)\\ &-(\underline{l_A^x l_B^z - l_A^z l_B^x})] - \frac{3}{8}g_1[m_A^z(\boldsymbol{d}\cdot\boldsymbol{\nabla})m_B^x + l_A^z(\boldsymbol{d}\cdot\boldsymbol{\nabla})l_B^x] + \frac{3}{8}g_2\Big\{[m_A^x(\boldsymbol{e}\cdot\boldsymbol{\nabla})m_B^z\\ &-m_A^z(\boldsymbol{e}\cdot\boldsymbol{\nabla})m_B^x] - [\underline{l_A^x(\boldsymbol{e}\cdot\boldsymbol{\nabla})l_B^z} - l_A^z(\boldsymbol{e}\cdot\boldsymbol{\nabla})l_B^x]\Big\},\end{aligned} \tag{A.17}$$

$$\begin{aligned}\frac{dm_A^z}{dt} \approx&(\cdots) + \frac{3}{4}g_1(\epsilon_{xx}+\epsilon_{yy})[(m_A^y m_B^x - m_A^x m_B^y) + (\underline{l_A^y l_B^x - l_A^x l_B^y})]\\ &+\frac{3}{4}g_2(\epsilon_{xx}+\epsilon_{yy}+2\epsilon_{zz})[(m_A^y m_B^x - m_A^x m_B^y) - \underline{(l_A^y l_B^x - l_A^x l_B^y)}]\\ &+\frac{3}{8}g_1\Big\{[m_A^y(\boldsymbol{d}\cdot\boldsymbol{\nabla})m_B^x - m_A^x(\boldsymbol{d}\cdot\boldsymbol{\nabla})m_B^y] + [\underline{l_A^y(\boldsymbol{d}\cdot\boldsymbol{\nabla})l_B^x} - \underline{l_A^x(\boldsymbol{d}\cdot\boldsymbol{\nabla})l_B^y}]\Big\}\\ &+\frac{3}{8}g_2\Big\{[m_A^y(\boldsymbol{e}\cdot\boldsymbol{\nabla})m_B^x - m_A^x(\boldsymbol{e}\cdot\boldsymbol{\nabla})m_B^y] - [\underline{l_A^y(\boldsymbol{e}\cdot\boldsymbol{\nabla})l_B^x - l_A^x(\boldsymbol{e}\cdot\boldsymbol{\nabla})l_B^y}]\Big\},\end{aligned} \tag{A.18}$$

$$\begin{aligned}\frac{dl_A^x}{dt} \approx&(\cdots) + \frac{3}{4}g_1(\epsilon_{xx}+\epsilon_{yy})(\underline{m_A^z l_B^y} + l_A^z m_B^y) + \frac{3}{4}g_2(\epsilon_{xx}+\epsilon_{yy}+2\epsilon_{zz})[(l_A^z m_B^y - \underline{l_A^y m_B^z})\\ &-(\underline{m_A^z l_B^y} - m_A^y l_B^z) + 4(l_A^z m_A^y - \underline{m_A^z l_A^y})] + \frac{3}{8}g_1[m_A^z(\boldsymbol{d}\cdot\boldsymbol{\nabla})l_B^y + l_A^z(\boldsymbol{d}\cdot\boldsymbol{\nabla})m_B^y]\\ &+\frac{3}{8}g_2\Big\{[l_A^z(\boldsymbol{e}\cdot\boldsymbol{\nabla})m_B^y - \underline{l_A^y(\boldsymbol{e}\cdot\boldsymbol{\nabla})m_B^z}] - [m_A^z(\boldsymbol{e}\cdot\boldsymbol{\nabla})l_B^y - m_A^y(\boldsymbol{e}\cdot\boldsymbol{\nabla})l_B^z]\Big\},\end{aligned} \tag{A.19}$$

$$\begin{aligned}\frac{dl_A^y}{dt} \approx&(\cdots) - \frac{3}{4}g_1(\epsilon_{xx}+\epsilon_{yy})(\underline{m_A^z l_B^x} + l_A^z m_B^x) + \frac{3}{4}g_2(\epsilon_{xx}+\epsilon_{yy}+2\epsilon_{zz})[(\underline{l_A^x m_B^z} - l_A^z m_B^x)\\ &-(m_A^x l_B^z - \underline{m_A^z l_B^x}) + 4(\underline{l_A^x m_A^z} - m_A^x l_A^z)] - \frac{3}{8}g_1[m_A^z(\boldsymbol{d}\cdot\boldsymbol{\nabla})l_B^x + l_A^z(\boldsymbol{d}\cdot\boldsymbol{\nabla})m_B^x]\\ &+\frac{3}{8}g_2\Big\{[\underline{l_A^x(\boldsymbol{e}\cdot\boldsymbol{\nabla})m_B^z} - l_A^z(\boldsymbol{e}\cdot\boldsymbol{\nabla})m_B^x] - [m_A^x(\boldsymbol{e}\cdot\boldsymbol{\nabla})l_B^z - m_A^z(\boldsymbol{e}\cdot\boldsymbol{\nabla})l_B^x]\Big\},\end{aligned} \tag{A.20}$$

and

$$\begin{aligned}\frac{dl_A^z}{dt} \approx & (\cdots) + \underline{\frac{3}{4}g_1(\epsilon_{xx}+\epsilon_{yy})[(m_A^y l_B^x - m_A^x l_B^y) + (l_A^y m_B^x - l_A^x m_B^y)]} \\ & \underline{+\frac{3}{4}g_2(\epsilon_{xx}+\epsilon_{yy}+2\epsilon_{zz})[(l_A^y m_B^x - l_A^x m_B^y) - (m_A^y l_B^x - m_A^x l_B^y) + 4(l_A^y m_A^x - m_A^y l_A^x)]} \\ & + \frac{3}{8}g_1\Big\{[m_A^y(\boldsymbol{d}\cdot\boldsymbol{\nabla})l_B^x - m_A^x(\boldsymbol{d}\cdot\boldsymbol{\nabla})l_B^y] + [\underline{l_A^y(\boldsymbol{d}\cdot\boldsymbol{\nabla})m_B^x - l_A^x(\boldsymbol{d}\cdot\boldsymbol{\nabla})m_B^y}]\Big\} \\ & + \frac{3}{8}g_2\Big\{[m_A^y(\boldsymbol{e}\cdot\boldsymbol{\nabla})m_B^x - m_A^x(\boldsymbol{e}\cdot\boldsymbol{\nabla})m_B^y] - [m_A^y(\boldsymbol{e}\cdot\boldsymbol{\nabla})l_B^x - m_A^x(\boldsymbol{e}\cdot\boldsymbol{\nabla})l_B^y]\Big\}. \qquad \text{(A.21)}\end{aligned}$$

Again, $(\cdots)$ is the short notation which represents all the terms on the right hand side of the unperturbed Eqs. (A.4)-(A.9). To obtain the equations of motion for $\boldsymbol{m}_B$ and $\boldsymbol{l}_B$, one just needs to apply (i) $A \leftrightarrow B$, (ii) $\frac{\partial}{\partial z} \to -\frac{\partial}{\partial z}$, (iii) $\boldsymbol{d} \to -\boldsymbol{d}$, and (iv) $\boldsymbol{e} \to -\boldsymbol{e}$ to Eqs. (A.16)-(A.21).

For linearized dynamics, we may keep in the above equations the underlined terms only. Next, we drop all the terms containing $\pm\frac{\partial}{\partial z}$, $\boldsymbol{d}$, and $\boldsymbol{e}$. As we have argued previously, under this approximation, the equations for A and B sublattices coincide, and we will assume that $\boldsymbol{m}_A = \boldsymbol{m}_B = \boldsymbol{m}$ and $\boldsymbol{l}_A = \boldsymbol{l}_B = \boldsymbol{l}$. Finally, by applying the standard parametrization, we find the linearized equations for m_θ, m_ϕ, θ, and ϕ in the presence of a lattice deformation, i.e., Eqs. (3.41) and (3.42) written in Chapter 3.

APPENDIX B

SUPPLEMENTAL INFORMATION FOR CHAPTER 4*

In Chapter 4 we concentrated on the *to-and-fro* motion of a spin wave (magnon) in the presence of a spatially modulated static strain. The deformation induced by the strain modulates the spin exchange between magnetic atoms which in turn acts as a scattering potential for spin waves. A possible way to impose the static strain modulation was suggested in Ref. [57].

To present the idea in the simplest way, we discussed a layered van der Waals AFM which has a very clear geometry. For waves propagating in the direction transverse to the layers, it allows to reduce the problem to a one-dimensional one. Additional simplification is in the magnetic structure of the substance which consists of FM layers with the direction of magnetization alternating between the neighboring layers. This allows to use macroscopic classic variables for the description of spin waves.

We start with presenting the arguments that allowing us to neglect the higher harmonics in the process of scattering in Section B.1 of this appendix. In Chapter 4, we have studied the dynamics of the spin wave which propagates freely in the system when at a certain time the static strain is switched on. The problem has been solved by matching the initial conditions at the moment of switching on. Here, in Section B.2, we simulate a more practical scenario in which a Gaussian spin-wave packet is running inside or entering a region where the spatially modulated strain has been already imposed.

The possibility of controlling magnons by a spatially modulated deformation has a general character, and is not related neither to the specific geometry nor to the material considered in this chapter. To demonstrate the generality, we consider in Section B.3 the case of the oblique incidence of the spin wave, i.e., when the initial spin wave has a finite momentum component perpendicular to the direction of strain modulation. We showed that in the case of an oblique incidence the

---

*Reprinted with permission from "Control of spin waves by spatially modulated strain" by Ankang Liu and Alexander M. Finkel'stein, 2022. Phys. Rev. B, 105, L020404, Copyright 2022 by American Physical Society.

modulation works as a spin waveguide: the *to-and-fro* motion of a spin wave across the spatially deformed region is still preserved, whereas in the direction perpendicular to the strain modulation the wave propagates unidirectionally.

For the purpose of completeness, in Section B.4, we consider the time-dependent periodic potential, which is created by a standing acoustic wave (see, e.g., Ref. [50]). (In the case of a two-dimensional geometry, grating of the lattice can be done using the Surface Acoustic Wave (SAW) technique [54, 55].) The dynamics is most clear in the adiabatic limit, i.e., when the deformation of the lattice changes slowly compared to the spin waves. Note in this respect that in the van der Waals systems, both the speed of sound and of the magnons in the direction transverse to the layers are rather low, because of smallness of the inter-layer couplings. The widths of the acoustic and magnon bands are of the order of a few meV. The mutual relation of the speeds depends on a specific choice of the material [65, 66].

Finally, we discuss the role of the phases φ_1 and φ_2. They are the space and time phase differences of the freely propagating spin wave and the strain modulation defined at the moment of their meeting. The phase φ_2 exists, of course, only in the case of the time-dependent strain modulation. Unlike φ_1, the time phase difference affects the dynamics of spin waves very strongly.

As an application of the discussed mechanism of the control of magnons, we see *magnonics*.

B.1 Higher Harmonics

In Section 4.2, we have indicated that after dropping higher harmonics, like $\mathcal{S}_{\frac{3q}{2}}$ and $\mathcal{C}_{\frac{3q}{2}}$, one gets Eqs. (4.12) and (4.13). These equations yield the frequencies $\omega^2_{\mathcal{S},\frac{q}{2}} = JG_1[1-\frac{1}{2}(\frac{G_2}{G_1})](\frac{q}{2})^2$ and $\omega^2_{\mathcal{C},\frac{q}{2}} = JG_1[1+\frac{1}{2}(\frac{G_2}{G_1})](\frac{q}{2})^2$. The frequencies are splitted by the interaction G_2 (i.e., magnetoelasticity).

If the term $\mathcal{S}_{\frac{3q}{2}}$ is nevertheless considered, instead of Eq. (4.13), one obtains an extended equation

$$\omega^2 \begin{pmatrix} \mathcal{S}_{\frac{q}{2}} \\ \mathcal{S}_{\frac{3q}{2}} \end{pmatrix} = \begin{pmatrix} JG_1(\frac{q}{2})^2 - \frac{1}{2}JG_2(\frac{q}{2})^2 & \frac{1}{2}JG_2(\frac{3q}{2})^2 \\ \frac{1}{2}JG_2(\frac{q}{2})^2 & JG_1(\frac{3q}{2})^2 \end{pmatrix} \begin{pmatrix} \mathcal{S}_{\frac{q}{2}} \\ \mathcal{S}_{\frac{3q}{2}} \end{pmatrix} \tag{B.1}$$

which couples $\mathcal{S}_{\frac{q}{2}}$ and $\mathcal{S}_{\frac{3q}{2}}$. This matrix equation gives two eigenvalues $\omega_{\pm}^2 = \frac{1}{4}J[20G_1 - G_2 \pm (256G_1^2 + 32G_1G_2 + 37G_2^2)^{\frac{1}{2}}](\frac{q}{2})^2$. Obviously, we are interested only in the eigen-frequency, ω_-. Under the perturbative condition, i.e., $G_2 \ll G_1$, the expansion of ω_-^2 yields $\omega_-^2 = JG_1(\frac{q}{2})^2 - \frac{1}{2}JG_2(\frac{q}{2})^2 - \frac{9}{128}JG_2q^2(\frac{G2}{G1}) + \frac{9}{2048}JG_2q^2(\frac{G2}{G1})^2 + \frac{9}{4096}JG_2q^2(\frac{G2}{G1})^3 + \cdots$. Keeping only the first two terms in ω_-^2, one gets the approximated frequency $\omega_{\mathcal{S},\frac{q}{2}}^2 = JG_1[1 - \frac{1}{2}(\frac{G_2}{G_1})](\frac{q}{2})^2$. When even higher harmonics like $\mathcal{S}_{\frac{5q}{2}}$ or $\mathcal{C}_{\frac{5q}{2}}$ are taken into account, a system of the coupled equation for $\mathcal{S}_{\frac{q}{2}}$, $\mathcal{S}_{\frac{3q}{2}}$, and $\mathcal{S}_{\frac{5q}{2}}$ becomes

$$\omega^2 \begin{pmatrix} \mathcal{S}_{\frac{q}{2}} \\ \mathcal{S}_{\frac{3q}{2}} \\ \mathcal{S}_{\frac{5q}{2}} \end{pmatrix} = \begin{pmatrix} JG_1(\frac{q}{2})^2 - \frac{1}{2}JG_2(\frac{q}{2})^2 & \frac{1}{2}JG_2(\frac{3q}{2})^2 & 0 \\ \frac{1}{2}JG_2(\frac{q}{2})^2 & JG_1(\frac{3q}{2})^2 & \frac{1}{2}JG_2(\frac{5q}{2})^2 \\ 0 & \frac{1}{2}JG_2(\frac{3q}{2})^2 & JG_1(\frac{5q}{2})^2 \end{pmatrix} \begin{pmatrix} \mathcal{S}_{\frac{q}{2}} \\ \mathcal{S}_{\frac{3q}{2}} \\ \mathcal{S}_{\frac{5q}{2}} \end{pmatrix}. \tag{B.2}$$

The smallest eigen-frequency of the matrix Eq. (B.2) has the expansion $\omega_{exp}^2 = JG_1(\frac{q}{2})^2 - \frac{1}{2}JG_2(\frac{q}{2})^2 - \frac{9}{128}JG_2q^2(\frac{G2}{G1}) + \frac{9}{2048}JG_2q^2(\frac{G2}{G1})^2 - \frac{603}{32768}JG_2q^2(\frac{G2}{G1})^3 + \cdots$. To generalize the results even further, we get the matrix equation

$$\omega^2 \begin{pmatrix} \mathcal{S}_{\frac{q}{2}} \\ \mathcal{S}_{\frac{3q}{2}} \\ \mathcal{S}_{\frac{5q}{2}} \\ \mathcal{S}_{\frac{7q}{2}} \\ \vdots \end{pmatrix} = \begin{pmatrix} JG_1(\frac{q}{2})^2 - \frac{1}{2}JG_2(\frac{q}{2})^2 & \frac{1}{2}JG_2(\frac{3q}{2})^2 & 0 & 0 & \cdots \\ \frac{1}{2}JG_2(\frac{q}{2})^2 & JG_1(\frac{3q}{2})^2 & \frac{1}{2}JG_2(\frac{5q}{2})^2 & 0 & \cdots \\ 0 & \frac{1}{2}JG_2(\frac{3q}{2})^2 & JG_1(\frac{5q}{2})^2 & \frac{1}{2}JG_2(\frac{7q}{2})^2 & \cdots \\ 0 & 0 & \frac{1}{2}JG_2(\frac{5q}{2})^2 & JG_1(\frac{7q}{2})^2 & \cdots \\ \vdots & \vdots & \vdots & \vdots & \ddots \end{pmatrix} \begin{pmatrix} \mathcal{S}_{\frac{q}{2}} \\ \mathcal{S}_{\frac{3q}{2}} \\ \mathcal{S}_{\frac{5q}{2}} \\ \mathcal{S}_{\frac{7q}{2}} \\ \vdots \end{pmatrix} \tag{B.3}$$

with all harmonics $\mathcal{S}_{\frac{q}{2}}, \mathcal{S}_{\frac{3q}{2}}, \mathcal{S}_{\frac{5q}{2}}, \mathcal{S}_{\frac{7q}{2}}, \cdots$, taken into considerations. One can check that $\omega_{\mathcal{S},\frac{q}{2}}^2$ is a good approximation for the lowest eigenfrequency of this infinite system as long as $G_2 \ll G_1$. It is worth noting that numeric coefficients are in favor of this approximation; the expansion remains applicable even when $G_2 \sim G_1$.

The discussion of the harmonics $\mathcal{C}_{\frac{3q}{2}}, \mathcal{C}_{\frac{5q}{2}}, \mathcal{C}_{\frac{7q}{2}}, \cdots$ is similar.

B.2 Simulations of Spin-wave Packet

In this section, we present the results of simulations of the dynamics of a Gaussian spin-wave packet propagating inside (or entering into) the region, which is deformed by a static strain modulation along the z direction, i.e., $\epsilon_{zz} = \epsilon_0 \cos(qz)$. In Fig. B.1, we simulate the influence of the static strain modulation on the propagation of the Gaussian spin-wave packet. Suppose that, at $t = 0$, there is a Gaussian wave packet $\phi(z, t = 0) = \phi_0 e^{-\frac{(z-z_0)^2}{w^2}} \cos[\frac{q}{2}(z - z_0)]$ which consists of spin waves with momenta centered around $\frac{q}{2}$. Here, ϕ_0 is the magnitude of wave packet, z_0 indicates the initial position of the packet, while w describes the packet width. In free system, we expect the evolution of this Gaussian spin-wave packet leads to $\phi(z,t) = \phi_0 e^{-\frac{(z-z_0-v_s t)^2}{w^2}} \cos[\frac{q}{2}(z - z_0 - v_s t)]$. This is confirmed by the result shown in Fig. B.1(a) when the deformation in the system is off. As expected, we observe a straight motion of the wave packet without any change of its shape. However, when this spin-wave packet is running inside a region with deformation, we observe that, instead of propagating freely, the wave packet is spreading aside with respect to its initial position. This is because the wave components with momentum around $\frac{q}{2}$ perform the to-and-fro motion as

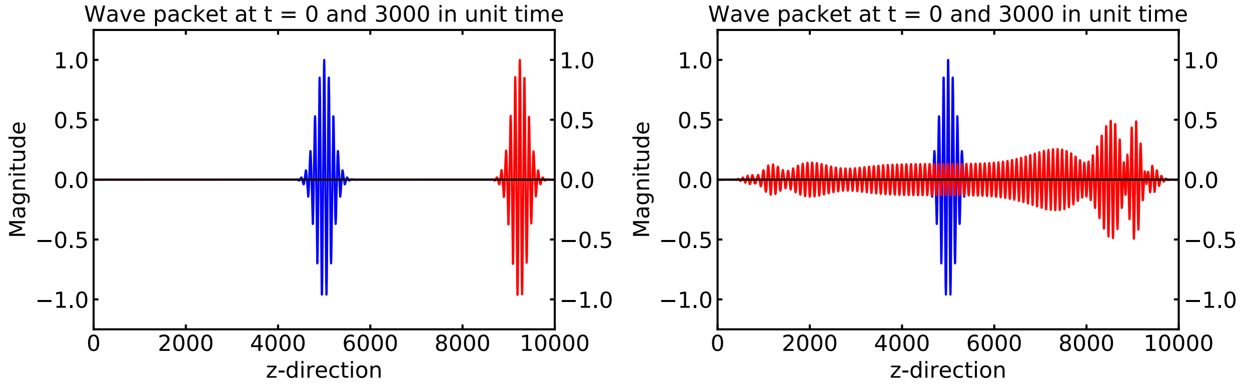

(a) Lattice deformation is off (b) Lattice deformation is on

Figure B.1: Simulations of a Gaussian wave packet propagating inside a region where the lattice deformation is (a) off and (b) on. In both figures (a) and (b), blue and red curves represent the wave packet at $t = 0$ and 3000 in unit time, respectively. In these simulations, we take $\phi_0 = 1$, $z_0 = 5000$, $w = 250$, and $q = 20 \times (2\pi/1000)$; other parameters are $J = 1$, $G_1 = 2$, and $G_2 = 0.3$.

has been discussed in Chapter 4 (see Fig. B.1(b)).

Furthermore, we have also simulated the case when a freely propagating Gaussian spin-wave packet runs on a region with preformed static deformation. From Fig. B.2, we observe that, after a certain time of evolution, there forms a number of bubble-like envelopes of the wave packet on the left (undeformed) side of the interface. The width of the bubbles is around $v_s(\frac{2\pi}{\omega_{\downarrow\uparrow}})$. We consider these bubbles as a signature of the to-and-fro motion which develops inside the deformed region. These bubbles are pumped backward by the wave-components of the packet on the right side of the interface which perform an alternating motion with the frequency $\omega_{\downarrow\uparrow}$.

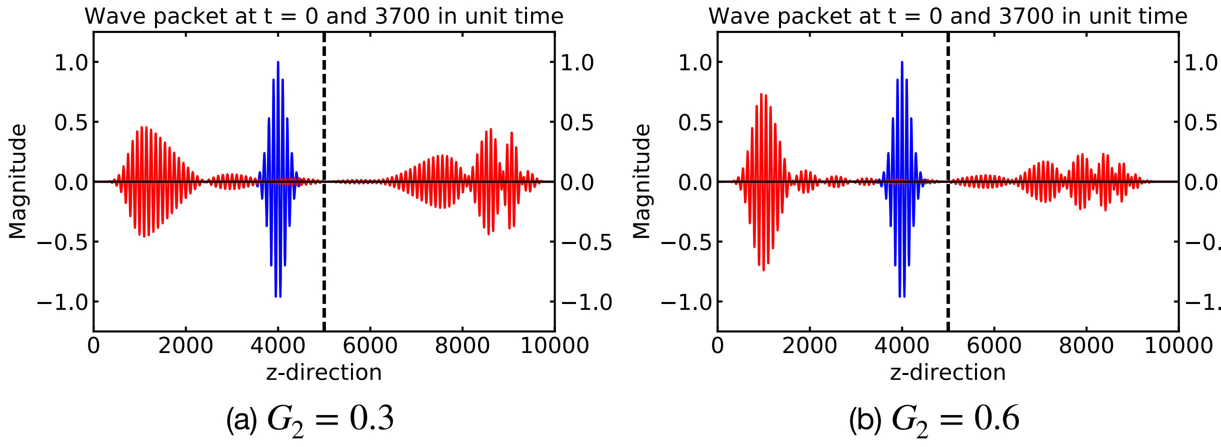

(a) $G_2 = 0.3$ (b) $G_2 = 0.6$

Figure B.2: Simulations of a Gaussian wave packet running on a deformed region with (a) $G_2 = 0.3$ and (b) $G_2 = 0.6$. In both figures (a) and (b), blue and red curves represent the wave packet at $t = 0$ and 3700 in unit time, respectively. The dashed vertical lines indicate the interface which separates the region with (on the right side of dashed line) and without (on the left side of dashed line) strain modulation. In these simulations, we take $\phi_0 = 1$, $z_0 = 4000$, $w = 250$, and $q = 20 \times (2\pi/1000)$; other parameters are $J = 1$ and $G_1 = 2$.

B.3 Oblique Incidence of the Spin Wave

Here we consider the case of an oblique incidence of a spin wave on the strain-modulated region. In other words, the initial direction of the spin wave propagation and the direction of strain modulation do not coincide. For simplicity, we restrict ourselves to a modulation along the z direction, i.e., $\epsilon_{zz} = \epsilon_0 \cos(qz)$, and will assume that the spatial resonance condition holds along this direction. Consequently, the equations of motion for (m_θ, ϕ) in three dimensions become (cf. Eqs. (3.41) and (3.44) in Chapter 3):

$$\begin{aligned}\dot{m}_\theta &\approx (4\tilde{S}^2)[(-\frac{3}{8}J_\parallel + \frac{9}{8}J_\perp)(\frac{\partial^2}{\partial x^2} + \frac{\partial^2}{\partial y^2}) + \frac{9}{4}J_\perp\frac{\partial^2}{\partial z^2}]\phi \\ &= [J_1(\frac{\partial^2}{\partial x^2} + \frac{\partial^2}{\partial y^2}) + J\frac{\partial^2}{\partial z^2}]\phi, \\ \dot{\phi} &\approx [G_1 + G_2\cos(qz)]m_\theta. \end{aligned} \tag{B.4}$$

Here, we define $J_1 \equiv (4\tilde{S}^2)(-\frac{3}{8}J_\parallel + \frac{9}{8}J_\perp)$ which describes the propagation of the spin wave in the directions not influenced by the strain (i.e., perpendicular to the direction of the applied strain modulation); the other coefficients J, G_1, and G_2 have been already introduced in Chapter 4 in connection with Eq. (4.1). From Eq. (B.4), we obtain a second time derivative equation for ϕ, namely,

$$\ddot{\phi} \approx [G_1 + G_2\cos(qz)][J_1(\frac{\partial^2}{\partial x^2} + \frac{\partial^2}{\partial y^2}) + J\frac{\partial^2}{\partial z^2}]\phi. \tag{B.5}$$

Note that, when $G_2 = 0$, it leads to a free spin wave solution $\phi(x,z,t) = \phi_0\sin[(k_\parallel x + \frac{q}{2}z) - \Omega t + \varphi_1]$ with the frequency $\Omega = \sqrt{G_1[J_1k_\parallel^2 + J(\frac{q}{2})^2]}$. Here, without losing generality, we take the in-plane component of the spin-wave momentum $k_\parallel$ to be along x direction, and φ_1 is an arbitrary initial phase of the wave. In the presence of G_2-term, we are looking for the solution which has a form of $\phi(x,z,t) = e^{\pm i\omega t}e^{\pm ik_\parallel x}\varphi(z)$. After the substitution, we get

$$-\omega^2\varphi(z) = [G_1 + G_2\cos(qz)][-J_1k_\parallel^2 + J\frac{\partial^2}{\partial z^2}]\varphi(z). \tag{B.6}$$

Following the procedure developed in Chapter 4, we write $\varphi(z) \approx \mathcal{S}_{\frac{q}{2}}\sin\left(\frac{q}{2}z\right) + \mathcal{C}_{\frac{q}{2}}\cos\left(\frac{q}{2}z\right)$. Then, neglecting the higher harmonics, we obtain two decoupled equations

$$\omega^2\mathcal{S}_{\frac{q}{2}} = G_1[1 - \frac{1}{2}(\frac{G_2}{G_1})][J_1k_\parallel^2 + J(\frac{q}{2})^2]\mathcal{S}_{\frac{q}{2}} \tag{B.7}$$

and

$$\omega^2 \mathcal{C}_{\frac{q}{2}} = G_1[1 + \frac{1}{2}(\frac{G_2}{G_1})][J_1 k_\parallel^2 + J(\frac{q}{2})^2]\mathcal{C}_{\frac{q}{2}}. \tag{B.8}$$

Now, we get two splitted frequencies $\omega_{\mathcal{S}}^2 = [1 - \frac{1}{2}(\frac{G_2}{G_1})]\Omega^2$ and $\omega_{\mathcal{C}}^2 = [1 + \frac{1}{2}(\frac{G_2}{G_1})]\Omega^2$ with Ω to be the frequency of the free spin wave with $\boldsymbol{k} = k_\parallel \hat{x} + \frac{q}{2}\hat{z}$. As a result, we can construct the general solution of $\phi(x, z, t)$, i.e.,

$$\phi(x, z, t) = \sum_{\pm\pm}[\lambda_{\pm\pm}^{\mathcal{S}} e^{\pm i\omega_{\mathcal{S}} t} e^{\pm i k_\parallel x} \sin\Big(\frac{q}{2}z\Big) + \lambda_{\pm\pm}^{\mathcal{C}} e^{\pm i\omega_{\mathcal{C}} t} e^{\pm i k_\parallel x} \sin\Big(\frac{q}{2}z\Big)]. \tag{B.9}$$

Correspondingly, the general solution of $m_\theta(x, z, t)$ is

$$\begin{aligned} m_\theta(x, z, t) = &- [J_1 k_\parallel^2 + J(\frac{q}{2})^2] \times [\frac{\lambda_{++}^{\mathcal{S}}}{i\omega_{\mathcal{S}}} e^{i\omega_{\mathcal{S}} t} e^{i k_\parallel x} \sin\Big(\frac{q}{2}z\Big) + \frac{\lambda_{+-}^{\mathcal{S}}}{i\omega_{\mathcal{S}}} e^{i\omega_{\mathcal{S}} t} e^{-i k_\parallel x} \sin\Big(\frac{q}{2}z\Big) \\ &+ \frac{\lambda_{-+}^{\mathcal{S}}}{-i\omega_{\mathcal{S}}} e^{-i\omega_{\mathcal{S}} t} e^{i k_\parallel x} \sin\Big(\frac{q}{2}z\Big) + \frac{\lambda_{--}^{\mathcal{S}}}{-i\omega_{\mathcal{S}}} e^{-i\omega_{\mathcal{S}} t} e^{-i k_\parallel x} \sin\Big(\frac{q}{2}z\Big) \\ &+ \frac{\lambda_{++}^{\mathcal{C}}}{i\omega_{\mathcal{C}}} e^{i\omega_{\mathcal{C}} t} e^{i k_\parallel x} \cos\Big(\frac{q}{2}z\Big) + \frac{\lambda_{+-}^{\mathcal{C}}}{i\omega_{\mathcal{C}}} e^{i\omega_{\mathcal{C}} t} e^{-i k_\parallel x} \cos\Big(\frac{q}{2}z\Big) \\ &+ \frac{\lambda_{-+}^{\mathcal{C}}}{-i\omega_{\mathcal{C}}} e^{-i\omega_{\mathcal{C}} t} e^{i k_\parallel x} \cos\Big(\frac{q}{2}z\Big) + \frac{\lambda_{--}^{\mathcal{C}}}{-i\omega_{\mathcal{C}}} e^{-i\omega_{\mathcal{C}} t} e^{-i k_\parallel x} \cos\Big(\frac{q}{2}z\Big)]. \end{aligned} \tag{B.10}$$

Here, the eight coefficients $\lambda_{\pm\pm}^{S/C}$ need to be determined through the properly chosen initial conditions. Similarly to Chapter 4, we assume that the static strain modulation is switched on at $t = 0$, while a free spin wave with $\boldsymbol{k} = k_\parallel \hat{x} + \frac{q}{2}\hat{z}$ is running in the system. Then, the initial conditions to be matched look as follows:

$$\begin{aligned} \phi(x, z, 0) &= \phi_0 \sin[(k_\parallel x + \frac{q}{2}z) + \varphi_1], \\ m_\theta(x, z, 0) &= -\frac{J_1 k_\parallel^2 + J(\frac{q}{2})^2}{\Omega} \phi_0 \cos[(k_\parallel x + \frac{q}{2}z) + \varphi_1]; \end{aligned} \tag{B.11}$$

By matching Eqs. (B.9)-(B.10) with Eq. (B.11), we find

$$\begin{aligned}
\lambda^{\mathcal{S}}_{++} &= \frac{1}{4}\phi_0(1-\frac{\omega_{\mathcal{S}}}{\Omega})e^{i\varphi_1},\ \lambda^{\mathcal{S}}_{-+} = \frac{1}{4}\phi_0(1+\frac{\omega_{\mathcal{S}}}{\Omega})e^{i\varphi_1},\\
\lambda^{\mathcal{S}}_{+-} &= \frac{1}{4}\phi_0(1+\frac{\omega_{\mathcal{S}}}{\Omega})e^{-i\varphi_1},\ \lambda^{\mathcal{S}}_{--} = \frac{1}{4}\phi_0(1-\frac{\omega_{\mathcal{S}}}{\Omega})e^{-i\varphi_1},\\
\lambda^{\mathcal{C}}_{++} &= -\frac{i}{4}\phi_0(1-\frac{\omega_{\mathcal{C}}}{\Omega})e^{i\varphi_1},\ \lambda^{\mathcal{C}}_{-+} = -\frac{i}{4}\phi_0(1+\frac{\omega_{\mathcal{C}}}{\Omega})e^{i\varphi_1},\\
\lambda^{\mathcal{C}}_{+-} &= \frac{i}{4}\phi_0(1+\frac{\omega_{\mathcal{C}}}{\Omega})e^{-i\varphi_1},\ \lambda^{\mathcal{C}}_{--} = \frac{i}{4}\phi_0(1-\frac{\omega_{\mathcal{C}}}{\Omega})e^{-i\varphi_1}.
\end{aligned} \tag{B.12}$$

After substituting the determined coefficients $\lambda^{S/C}_{\pm\pm}$ into Eq. (B.9), we get

$$\begin{aligned}
\phi(x,z,t) =&\phi_0\Big\{(\frac{\omega_{\downarrow\uparrow}}{4\Omega})\cos\left(\frac{\omega_{\downarrow\uparrow}t}{2}\right)\sin[(k_\parallel x-\frac{q}{2}z)-\Omega t+\varphi_1]\\
&-(1)\sin\left(\frac{\omega_{\downarrow\uparrow}t}{2}\right)\cos[(k_\parallel x-\frac{q}{2}z)-\Omega t+\varphi_1]\\
&+(1)\cos\left(\frac{\omega_{\downarrow\uparrow}t}{2}\right)\sin[(k_\parallel x+\frac{q}{2}z)-\Omega t+\varphi_1]\\
&-(\frac{\omega_{\downarrow\uparrow}}{4\Omega})\sin\left(\frac{\omega_{\downarrow\uparrow}t}{2}\right)\cos[(k_\parallel x+\frac{q}{2}z)-\Omega t+\varphi_1]\\
&-(\frac{\omega_{\downarrow\uparrow}}{4\Omega})\cos\left(\frac{\omega_{\downarrow\uparrow}t}{2}\right)\sin[(k_\parallel x-\frac{q}{2}z)+\Omega t+\varphi_1]\\
&+(0)\sin\left(\frac{\omega_{\downarrow\uparrow}t}{2}\right)\cos[(k_\parallel x-\frac{q}{2}z)+\Omega t+\varphi_1]\\
&+(0)\cos\left(\frac{\omega_{\downarrow\uparrow}t}{2}\right)\sin[(k_\parallel x+\frac{q}{2}z)+\Omega t+\varphi_1]\\
&-(\frac{\omega_{\downarrow\uparrow}}{4\Omega})\sin\left(\frac{\omega_{\downarrow\uparrow}t}{2}\right)\cos[(k_\parallel x+\frac{q}{2}z)+\Omega t+\varphi_1]\Big\}.
\end{aligned} \tag{B.13}$$

And, finally,

$$\begin{aligned}
\phi(x,z,t) \approx&\phi_0\Big\{\cos\left(\frac{\omega_{\downarrow\uparrow}t}{2}\right)\sin[(k_\parallel x+\frac{q}{2}z)-\Omega t+\varphi_1]\\
&-\sin\left(\frac{\omega_{\downarrow\uparrow}t}{2}\right)\cos[(k_\parallel x-\frac{q}{2}z)-\Omega t+\varphi_1]\Big\}.
\end{aligned} \tag{B.14}$$

Here, we defined $\omega_{\downarrow\uparrow} \equiv \omega_{\mathcal{C}} - \omega_{\mathcal{S}}$. As a result, the solution $\phi(x,z,t)$ describes the alternation between two spin wave states with $\boldsymbol{k} = k_\parallel\hat{x} + \frac{q}{2}\hat{z}$ and $\boldsymbol{k} = k_\parallel\hat{x} - \frac{q}{2}\hat{z}$ with an alternating frequency

$\omega_{\downarrow\uparrow}$, provided that $\omega_{\downarrow\uparrow} \ll \Omega$, i.e., $G_2 \ll G_1$. In this sense, the strain modulation serves as a spin waveguide when the propagating direction of the initial wave is not parallel to the one induced by the strain.

B.4 Solutions of (m_θ, ϕ) and Dynamics at Time-dependent Strain Modulation

In this section, we discuss the dynamics of m_θ and ϕ when the lattice deformation is not only spatial- but also time-dependent. We restrict ourselves to the conditions of the spatial resonance, i.e., $k = \frac{q}{2}$, and assume that there is a standing acoustic wave along the z direction, namely, $\boldsymbol{u} = A\sin(qz)\cos(\omega_{ph}t + \varphi_2)\hat{z}$., where the unit vector $\hat{z}$ indicates the polarization of this wave. Then, the nonzero component of the strain tensor is $\epsilon_{zz} = \epsilon_0 \cos(qz)\cos(\omega_{ph}t + \varphi_2)$ with the magnitude $\epsilon_0 = Aq$. Here, A is the amplitude of the wave, $\omega_{ph} = v_{ph}q$ is the frequency of the longitudinal acoustic wave, while v_{ph} is the speed of sound along the z direction (a brief discussion of v_{ph} versus v_s was given in Sec. S1). Recall in connection with the phase φ_2 that $t = 0$ is defined as the moment of meeting of the spin wave with the acoustic deformation. Correspondingly, the phase φ_2 (as well as φ_1; see the discussion of the inset in Fig. 4.4 in Chapter 4) are determined with respect to this moment. In the discussed case, one needs to solve the time-dependent version of Eqs. (4.1), i.e.,

$$\begin{aligned} \dot{m}_\theta &= J\frac{d^2}{dz^2}\phi, \\ \dot{\phi} &= [G_1 + G_2\cos(qz)\cos(\omega_{ph}t + \varphi_2)]m_\theta. \end{aligned} \tag{B.15}$$

Next, neglecting the higher harmonics and using the ansatz

$$m_\theta(z,t) = \mathcal{S}_{m_\theta,\frac{q}{2}}(t)\sin\Big(\frac{q}{2}z\Big) + \mathcal{C}_{m_\theta,\frac{q}{2}}(t)\cos\Big(\frac{q}{2}z\Big) \tag{B.16}$$

and

$$\phi(z,t) = \mathcal{S}_{\phi,\frac{q}{2}}(t)\sin\Big(\frac{q}{2}z\Big) + \mathcal{C}_{\phi,\frac{q}{2}}(t)\cos\Big(\frac{q}{2}z\Big), \tag{B.17}$$

we obtain a set of equations for the time-dependent coefficients $\mathcal{S}_{m_\theta,\frac{q}{2}}(t)$, $\mathcal{S}_{\phi,\frac{q}{2}}(t)$, $\mathcal{C}_{m_\theta,\frac{q}{2}}(t)$, and $\mathcal{C}_{\phi,\frac{q}{2}}(t)$:

$$\begin{aligned}\dot{\mathcal{S}}_{m_\theta,\frac{q}{2}}(t) =& - J(\frac{q}{2})^2\mathcal{S}_{\phi,\frac{q}{2}}(t),\\ \dot{\mathcal{S}}_{\phi,\frac{q}{2}}(t) =& G_1\mathcal{S}_{m_\theta,\frac{q}{2}}(t) - \frac{1}{2}G_2\cos(\omega_{ph}t + \varphi_2)\mathcal{S}_{m_\theta,\frac{q}{2}}(t);\end{aligned} \tag{B.18}$$

and

$$\begin{aligned}\dot{\mathcal{C}}_{m_\theta,\frac{q}{2}}(t) =& - J(\frac{q}{2})^2\mathcal{C}_{\phi,\frac{q}{2}}(t),\\ \dot{\mathcal{C}}_{\phi,\frac{q}{2}}(t) =& G_1\mathcal{C}_{m_\theta,\frac{q}{2}}(t) + \frac{1}{2}G_2\cos(\omega_{ph}t + \varphi_2)\mathcal{C}_{m_\theta,\frac{q}{2}}(t).\end{aligned} \tag{B.19}$$

Thus, $\mathcal{S}_{\phi,\frac{q}{2}}$ accelerates $\mathcal{S}_{m_\theta,\frac{q}{2}}$, while the time-dependent combination of $\mathcal{S}_{m_\theta,\frac{q}{2}}$ terms pushes $\mathcal{S}_{\phi,\frac{q}{2}}$. The same happens with the other pair $\mathcal{C}_{\phi,\frac{q}{2}}$ and $\mathcal{C}_{m_\theta,\frac{q}{2}}$. We differentiate the first equation in each of the pairs, and use the second ones to close the equations for $\mathcal{S}_{m_\theta,\frac{q}{2}}$ and $\mathcal{C}_{m_\theta,\frac{q}{2}}$. Eventually, instead of Eqs. (7) and (8) in Chapter 4, we get a pair of the Floquet equations:

$$\ddot{\mathcal{S}}_{m_\theta,\frac{q}{2}}(t) = -JG_1(\frac{q}{2})^2[1 - (\frac{G_2}{2G_1})\cos(\omega_{ph}t + \varphi_2)]\mathcal{S}_{m_\theta,\frac{q}{2}}(t) \tag{B.20}$$

and

$$\ddot{\mathcal{C}}_{m_\theta,\frac{q}{2}}(t) = -JG_1(\frac{q}{2})^2[1 + (\frac{G_2}{2G_1})\cos(\omega_{ph}t + \varphi_2)]\mathcal{C}_{m_\theta,\frac{q}{2}}(t). \tag{B.21}$$

The solutions of $\mathcal{S}_{m_\theta,\frac{q}{2}}(t)$ and $\mathcal{C}_{m_\theta,\frac{q}{2}}(t)$ can be found in terms of the Mathieu functions:

$$\mathcal{S}_{m_\theta,\frac{q}{2}}(t) = Q_S ¢\Big(\frac{JG_1q^2}{\omega_{ph}^2}, \frac{JG_2q^2}{4\omega_{ph}^2}, \frac{\omega_{ph}t + \varphi_2}{2}\Big) + R_S \$\Big(\frac{JG_1q^2}{\omega_{ph}^2}, \frac{JG_2q^2}{4\omega_{ph}^2}, \frac{\omega_{ph}t + \varphi_2}{2}\Big) \tag{B.22}$$

and

$$\mathcal{C}_{m_\theta,\frac{q}{2}}(t) = Q_C \text{₵}\Big(\frac{JG_1q^2}{\omega_{ph}^2}, -\frac{JG_2q^2}{4\omega_{ph}^2}, \frac{\omega_{ph}t+\varphi_2}{2}\Big) + R_C \$\Big(\frac{JG_1q^2}{\omega_{ph}^2}, -\frac{JG_2q^2}{4\omega_{ph}^2}, \frac{\omega_{ph}t+\varphi_2}{2}\Big). \tag{B.23}$$

Here, $\text{₵}(a,q,v)$ and $\$(a,q,v)$ are the even and odd solutions to the Mathieu differential equation [67]. The coefficients $Q_{S/C}$ and $R_{S/C}$ are determined by the initial conditions. We take the same initial conditions as in the static case, namely, $m_\theta(z,t=0) = -\frac{J(\frac{q}{2})^2}{\Omega}\phi_0\cos\big(\frac{q}{2}z+\varphi_1\big)$ and $\phi(z,t=0) = \phi_0\sin\big(\frac{q}{2}z+\varphi_1\big)$. For arbitrary φ_1 and φ_2, by matching this initial conditions, one obtains a system of relations for the coefficients $Q_{S/C}$ and $R_{S/C}$:

$$\begin{aligned}
&Q_S\text{₵}\Big(\tilde{G}_1,\tilde{G}_2,\frac{\omega_{ph}t+\varphi_2}{2}\Big)\Big|_{t=0} + R_S\$\Big(\tilde{G}_1,\tilde{G}_2,\frac{\omega_{ph}t+\varphi_2}{2}\Big)\Big|_{t=0} = \frac{J(\frac{q}{2})^2}{\Omega}\phi_0\sin\varphi_1,\\
&Q_S\dot{\text{₵}}\Big(\tilde{G}_1,\tilde{G}_2,\frac{\omega_{ph}t+\varphi_2}{2}\Big)\Big|_{t=0} + R_S\dot{\$}\Big(\tilde{G}_1,\tilde{G}_2,\frac{\omega_{ph}t+\varphi_2}{2}\Big)\Big|_{t=0} = -J(\frac{q}{2})^2\phi_0\cos\varphi_1,\\
&Q_C\text{₵}\Big(\tilde{G}_1,-\tilde{G}_2,\frac{\omega_{ph}t+\varphi_2}{2}\Big)\Big|_{t=0} + R_C\$\Big(\tilde{G}_1,-\tilde{G}_2,\frac{\omega_{ph}t+\varphi_2}{2}\Big)\Big|_{t=0} = -\frac{J(\frac{q}{2})^2}{\Omega}\phi_0\cos\varphi_1,\\
&Q_C\dot{\text{₵}}\Big(\tilde{G}_1,-\tilde{G}_2,\frac{\omega_{ph}t+\varphi_2}{2}\Big)\Big|_{t=0} + R_C\dot{\$}\Big(\tilde{G}_1,-\tilde{G}_2,\frac{\omega_{ph}t+\varphi_2}{2}\Big)\Big|_{t=0} = -J(\frac{q}{2})^2\phi_0\sin\varphi_1
\end{aligned} \tag{B.24}$$

with $\tilde{G}_1 \equiv JG_1q^2/\omega_{ph}^2$ and $\tilde{G}_2 \equiv JG_2q^2/4\omega_{ph}^2$. Thus, one needs to solve the matrix equation (B.24) to determine the coefficients $Q_{S/C}$ and $R_{S/C}$.

We present first the result of studying the effect of the phase φ_1 on the propagation of the spin waves. As it is shown in Fig. B.3, similarly to the case of static modulation, motion of the spin wave does not depend much on φ_1. By contrast, the motion strongly depends on the other phase, φ_2, which is the initial phase in the time dependence of the standing acoustic wave.

We start discussion of the phase φ_2 with the special case $\varphi_2 = 0$ for various ω_{ph}. As it could be observed from Fig. B.4, a decisive factor here is the relation between the frequency of alternation $\omega_{\downarrow\uparrow}$ (determined for the static deformation) and the frequency of the acoustic wave, ω_{ph}. The characteristics of the spin wave motion in this special case are as follows: (i) In the limit of slowly varying acoustic wave, when $\omega_{ph} \ll \omega_{\downarrow\uparrow}$, the adiabatic picture holds. The alternating motion of

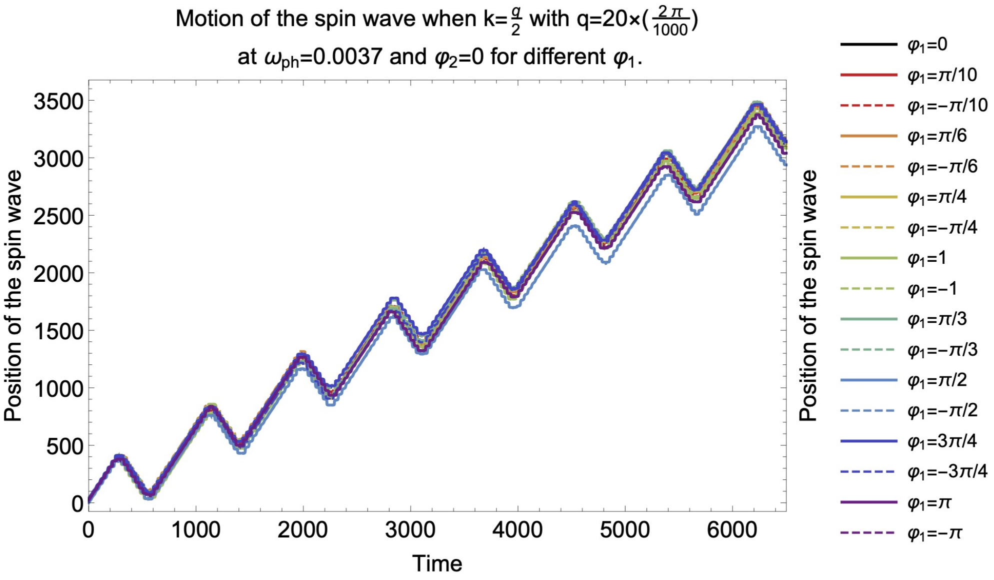

Figure B.3: Zig-zag motion of a spin wave at the spatial resonance condition, $k = q/2$, for different φ_1. The wave vector $q = 20 \times (2\pi/1000)$. Parameters of the system are $J = 1$, $G_1 = 2$, $G_2 = 0.3$. Frequency of the phonon $\omega_{ph} = 0.0037$, and the phase $\varphi_2 = 0$.

the spin wave still develops, but for a limited interval of time when the deformation induced by the acoustic wave is large enough. Next, a window follows when the deformation is weak and, hence, not effective. Within this window, the spin wave propagates in one direction only. (ii) The motion is strictly quantized. In the discussed case of $\varphi_2 = 0$, during a half-period of the standing acoustic wave, changing of the propagation direction occurs always *in pairs*. The number of pairs decreases with increasing the frequency: in the interval of frequencies shown in Fig. B.4(b), there are two pairs of turns during a half-period. For larger frequencies, as one can see from Fig. B.4(c) there remains only one pair of turns. (iii) Finally, when ω_{ph} is comparable with or greater than $\omega_{\downarrow\uparrow}$, the alternation of the propagating direction ceases to exist. This is due to the rapidness of the acoustic deformation oscillation. There is simply not enough time for the modulated strain to change the propagation of the spin wave. As one can see from the top curve in Fig. B.4(c), the spin wave propagates unidirectionally with the velocity of the free spin waves. (iv) The averaged speed of the propagation changes non-monotonically with ω_{ph}. In this peculiar case, we observe that in the interval of frequencies presented in Fig. B.4(b), the averaged speed goes down, and even changes

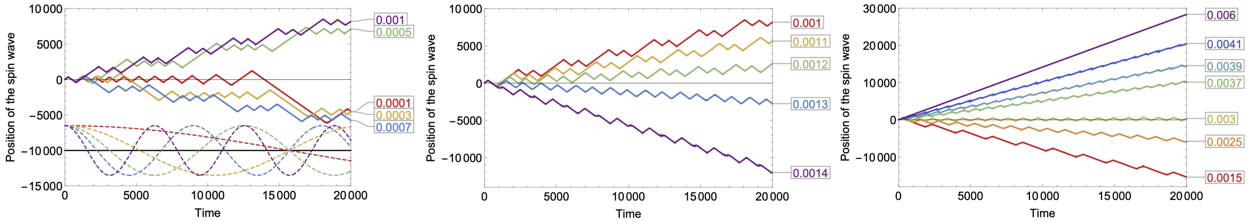

(a) ω_{ph}: 0.0001 to 0.001 (b) ω_{ph}: 0.001 to 0.0014 (b) ω_{ph}: 0.0015 to 0.006

Figure B.4: Motion of spin waves with $k = q/2$ at $\varphi_2 = 0$ and $\varphi_1 = 0$ for different ω_{ph}. Wave vector $q = 20 \times (2\pi/1000)$; other parameters are $J = 1$, $G_1 = 2$, $G_2 = 0.3$. For the chosen parameters, the frequency $\omega_{\downarrow\uparrow} \approx 0.0067$. At the bottom of the subfigure (a) the dashed lines show the magnitude of the external perturbation at different ω_{ph}. The phonon frequencies are indicated in the boxes on the right.

its sign. Then, for larger frequencies, the trend reverses (see Fig. B.4(c)). The speed grows up, so that eventually the motion becomes unidirectional.

Now, we present our results of studying the propagation of the spin wave at $\varphi_2 \neq 0$. In a number of panels in Fig. B.5, we show how the motion of the spin wave develops with time at various φ_2 for different intervals of ω_{ph}. Eventually, we demonstrate that the to-and-fro motion is a robust phenomenon. It exists for any phase φ_2, and even survives the averaging over different phases. One can notice from Figs. B.5(a), B.5(d), B.5(g), B.5(j), and B.5(m) that for $\varphi_2 \neq 0$ the adiabatic picture still holds when $\omega_{ph} \ll \omega_{\downarrow\uparrow}$. On the contrary, at not too small ω_{ph}, Figs. B.5(b), B.5(e), B.5(h), B.5(k), B.5(n) and Figs. B.5(c), B.5(f), B.5(i), B.5(l), B.5(o) demonstrate that for $\varphi_2 \neq 0$ the motion of the spin wave depends on ω_{ph} in a different manner as compared with the results obtained for the special case $\varphi_2 = 0$, cf. with Figs. B.4(b) and B.4(c). The main difference is in the time of periodicity. Instead of a half-period discussed above for $\varphi_2 = 0$, in the general case, $\varphi_2 \neq 0$, the period of the pattern for the propagation of the spin wave coincides with the (full) period of the acoustic wave. The results obtained here also confirm that the number of turns during a period decreases with increasing ω_{ph}. This eventually leads to a unidirectional propagation of the spin wave when ω_{ph} is comparable with $\omega_{\downarrow\uparrow}$.

One can observe by comparing Fig. B.6 with the corresponding panels in Figs. B.4 and B.5 that the patterns of the to-and-fro motion have a φ_2-periodicity that is (roughly) π. Interestingly,

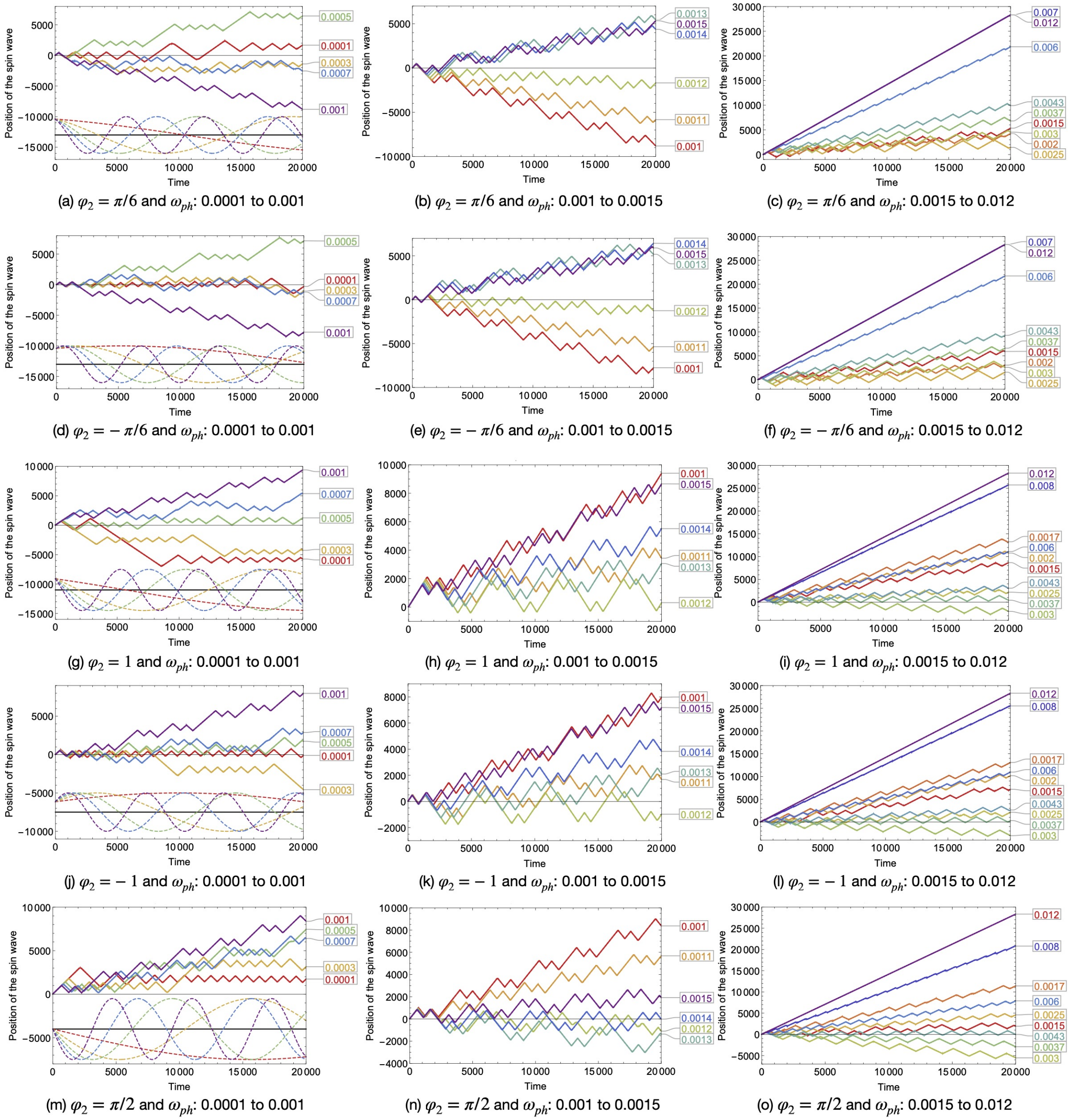

(a) $\varphi_2 = \pi/6$ and ω_{ph}: 0.0001 to 0.001

(b) $\varphi_2 = \pi/6$ and ω_{ph}: 0.001 to 0.0015

(c) $\varphi_2 = \pi/6$ and ω_{ph}: 0.0015 to 0.012

(d) $\varphi_2 = -\pi/6$ and ω_{ph}: 0.0001 to 0.001

(e) $\varphi_2 = -\pi/6$ and ω_{ph}: 0.001 to 0.0015

(f) $\varphi_2 = -\pi/6$ and ω_{ph}: 0.0015 to 0.012

(g) $\varphi_2 = 1$ and ω_{ph}: 0.0001 to 0.001

(h) $\varphi_2 = 1$ and ω_{ph}: 0.001 to 0.0015

(i) $\varphi_2 = 1$ and ω_{ph}: 0.0015 to 0.012

(j) $\varphi_2 = -1$ and ω_{ph}: 0.0001 to 0.001

(k) $\varphi_2 = -1$ and ω_{ph}: 0.001 to 0.0015

(l) $\varphi_2 = -1$ and ω_{ph}: 0.0015 to 0.012

(m) $\varphi_2 = \pi/2$ and ω_{ph}: 0.0001 to 0.001

(n) $\varphi_2 = \pi/2$ and ω_{ph}: 0.001 to 0.0015

(o) $\varphi_2 = \pi/2$ and ω_{ph}: 0.0015 to 0.012

Figure B.5: Motion of spin waves with $k = q/2$ at different ω_{ph} (see boxes on the right) for various φ_2. (a)-(c): $\varphi_2 = \pi/6$; (d)-(f): $\varphi_2 = -\pi/6$; (g)-(i): $\varphi_2 = 1$; (j)-(l): $\varphi_2 = -1$; (m)-(o): $\varphi_2 = \pi/2$. At the bottom of (a), (d), (g), (j), and (m) the dashed lines show the magnitude of the external perturbation at various ω_{ph}. Wave vector $q = 20 \times (2\pi/1000)$; other parameters are $J = 1$, $G_1 = 2$, $G_2 = 0.3$, and $\varphi_1 = 0$.

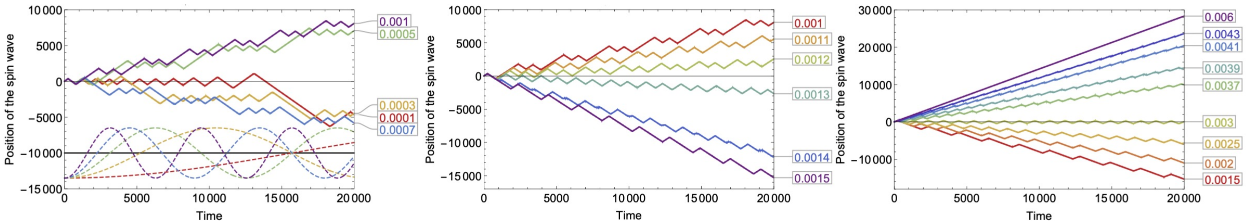

(a) $\varphi_2 = \pi$ and ω_{ph}: 0.0001 to 0.001 (b) $\varphi_2 = \pi$ and ω_{ph}: 0.001 to 0.0015 (c) $\varphi_2 = \pi$ and ω_{ph}: 0.0015 to 0.006

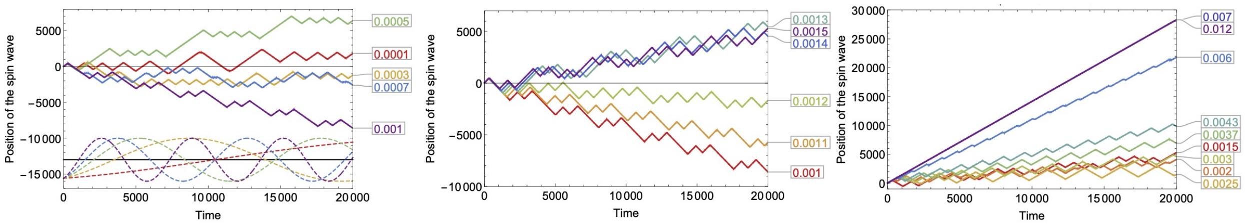

(d) $\varphi_2 = 7\pi/6$ and ω_{ph}: 0.0001 to 0.001 (e) $\varphi_2 = 7\pi/6$ and ω_{ph}: 0.001 to 0.0015 (f) $\varphi_2 = 7\pi/6$ and ω_{ph}: 0.0015 to 0.012

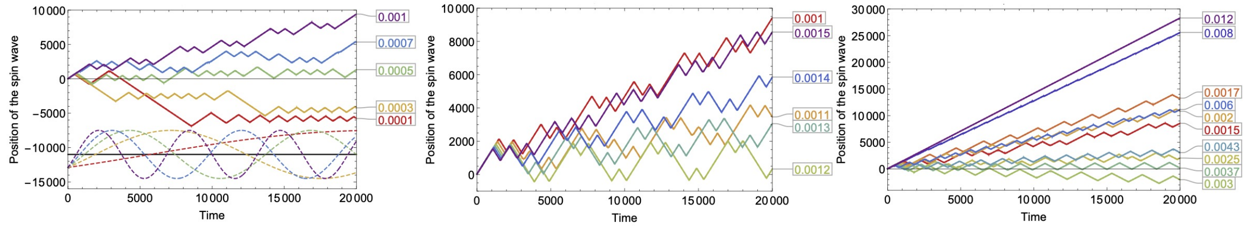

(g) $\varphi_2 = 1 + \pi$ and ω_{ph}: 0.0001 to 0.001 (h) $\varphi_2 = 1 + \pi$ and ω_{ph}: 0.001 to 0.0015 (i) $\varphi_2 = 1 + \pi$ and ω_{ph}: 0.0015 to 0.012

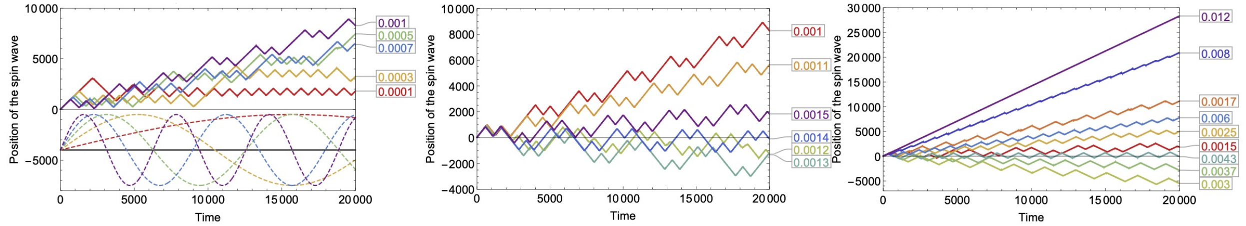

(j) $\varphi_2 = -\pi/2$ and ω_{ph}: 0.0001 to 0.001 (k) $\varphi_2 = -\pi/2$ and ω_{ph}: 0.001 to 0.0015 (l) $\varphi_2 = -\pi/2$ and ω_{ph}: 0.0015 to 0.012

Figure B.6: Motion of the spin wave with $k = q/2$ for different frequencies ω_{ph} (see boxes on the right) with various φ_2. (a)-(c): $\varphi_2 = \pi$, (d)-(f): $\varphi = 7\pi/6$; (g)-(i): $\varphi_2 = 1 + \pi$; (j)-(l): $\varphi_2 = -\pi/2$. At the bottom of (a), (d), (g), and (j), the dashed lines show the magnitude of the external perturbation with various ω_{ph}. Wave vector $q = 20 \times (2\pi/1000)$; other parameters are $J = 1$, $G_1 = 2$, $G_2 = 0.3$, and $\varphi_1 = 0$.

the solution does not coincide with itself when φ_2 is changed by π. But the *pattern* of propagation is reproduced. The reason for this is that changing φ_2 by π is equivalent to changing only the sign of the scattering amplitude G_2.

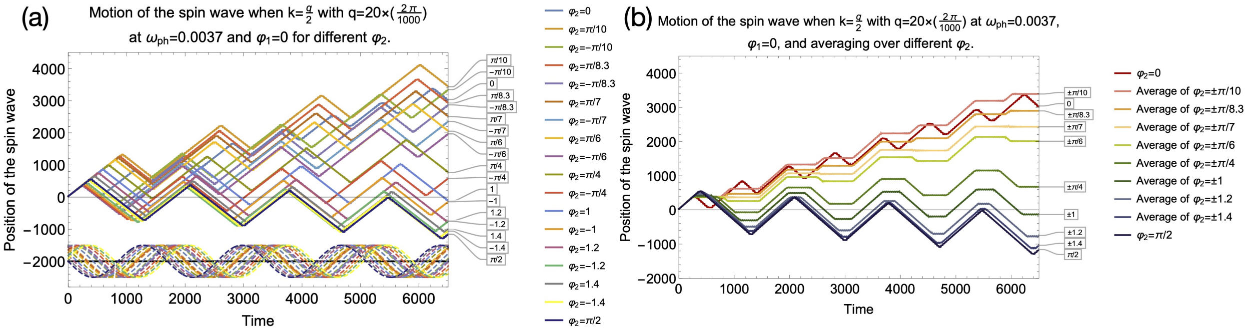

Figure B.7: (a) Motion of the spin wave with $k = q/2$ at $\omega_{ph} = 0.0037$ for different φ_2 (see boxes on the right). At the bottom of the figure, the dashed lines show the time-dependence of magnitude of the external perturbation for different φ_2. (b) The averaged motion of the spin wave over different positive and negative phases φ_2. Wave vector $q = 20 \times (2\pi/1000)$; other parameters are $J = 1$, $G_1 = 2$, $G_2 = 0.3$, and $\varphi_1 = 0$.

In order to study further the effects of φ_2, we plot (along with the propagation of the spin wave at different φ_2, Fig. B.7(a)) the motion *averaged* over both positive and negative values of φ_2. As one can observe from Fig. B.7(b), the to-and-fro pattern exists despite this averaging.

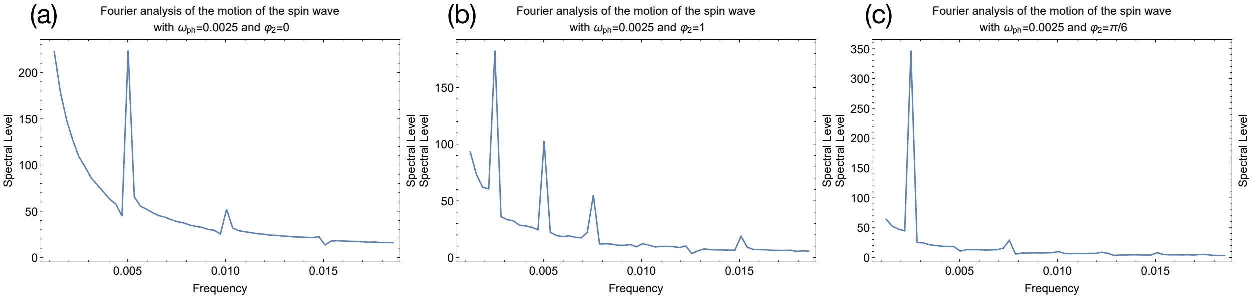

Figure B.8: The Fourier analysis of the spin wave propagation at $\omega_{ph} = 0.0025$ with different φ_2. Other parameters are $J = 1$, $G_1 = 2$, $G_2 = 0.3$, and $\varphi_1 = 0$.

Finally, we performed the Fourier analysis of the propagation patterns with different φ_2 for the spin wave when the frequency of the acoustic wave is $\omega_{ph} = 0.0025$. As it is shown in Figs. B.8, there is a major spectral peak at the frequency 0.0025 (at $\varphi_2 = \pi/6$ and 1), i.e., the position of the peak coincides with the frequency of the acoustic wave, ω_{ph}. However, in the special case of $\varphi_2 = 0$ the pattern has a pronounced spectral peak at the frequency equal to $2\omega_{ph} = 0.005$, which in this case is the lowest characteristic frequency. As a result, only for the special case $\varphi_2 = 0$, the propagation pattern repeats every half-period of the acoustic wave. Generally, however, the patterns repeat themselves in accord with the full period of the acoustic wave.

APPENDIX C

SUPPLEMENTAL INFORMATION FOR CHAPTER 5*

In this appendix, we present additional numerical results that support the study of AC magnonic crystal in Chapter 5. The results presented in Figs. C.1 and C.2 as well as in Figs. 5.2(a) and 5.2(b) in Chapter 5 are obtained through numerically solving Eq. (5.3) with the initial conditions (5.4) utilizing Mathematica "NDSolve" function [68]; while the simulations in Figs. C.3 and C.4 are done by the finite difference method based on the algorithm published in Ref. [69].

C.1 To-and-fro Motion

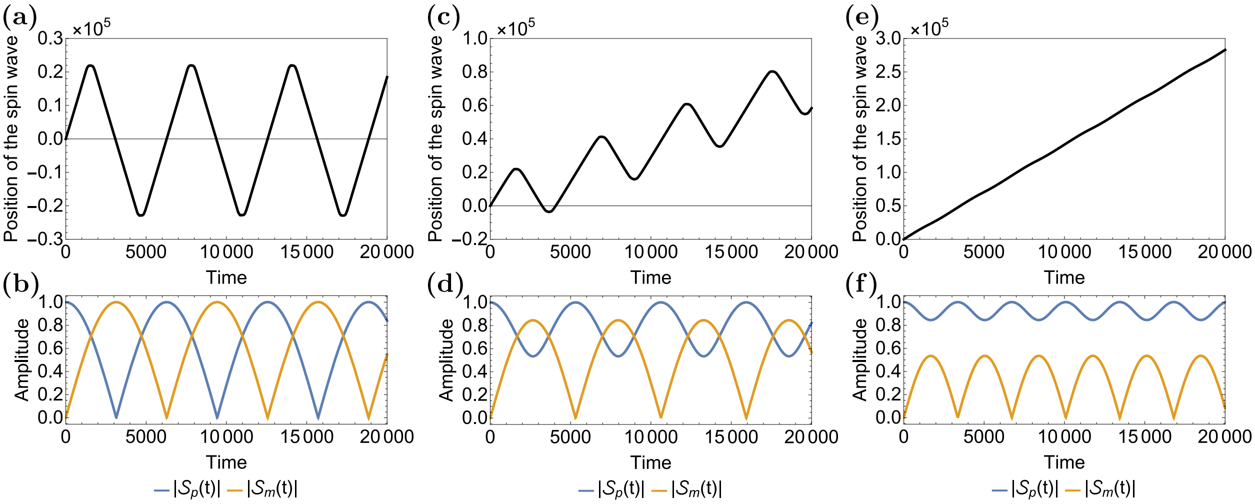

Figure C.1: Position of the spin waves with initial wave vectors $k = q/2 + \delta k$ (upper panels (a), (c), and (e)) together with $|\mathcal{S}_{p/m}(t)|$ (lower panels (b), (d), and (f)) as a function of time. Here, we plot for (a) and (b) the wave with $\delta k = 0.00$; (c) and (d) with $\delta k = 0.20$; while (e) and (f) with $\delta k = 0.50$ in units of $(2\pi/1000)$. Other parameters are $A = 2$, $q = 20 \times (2\pi/1000)$, $\gamma B_0 = 1$, $\gamma \Delta B_0 = 0.001$, and $\varphi_s = 0$. As shown in all three figures, the spin waves are propagating along the positive z direction when $|\mathcal{S}_p(t)| > |\mathcal{S}_m(t)|$, and vice versa.

---

*Reprinted with permission from "Spin-wave dynamics controlled by tunable ac magnonic crystal" by Ankang Liu and Alexander M. Finkel'stein, 2023. Phys. Rev. B (to be published), Copyright 2023 by American Physical Society.

As an extension of Fig. 5.2(a), in Fig. C.1 we plot the propagation of the spin waves with different wave vectors along with the competition between $|\mathcal{S}_p(t)|$ and $|\mathcal{S}_m(t)|$ after the DC magnonic crystal is switched on at $t = 0$. As one can conclude with the use of Fig. C.1, the direction of the propagation is determined by the relation of the amplitudes $|\mathcal{S}_p(t)|$ and $|\mathcal{S}_m(t)|$, which were introduced in Eq. (5.2). When $|\mathcal{S}_p(t)| > |\mathcal{S}_m(t)|$, the right-propagating component is dominant, and the wave is moving towards positive z direction, and vice versa.

C.2 Effect of Changing φ_s and φ_{ac}

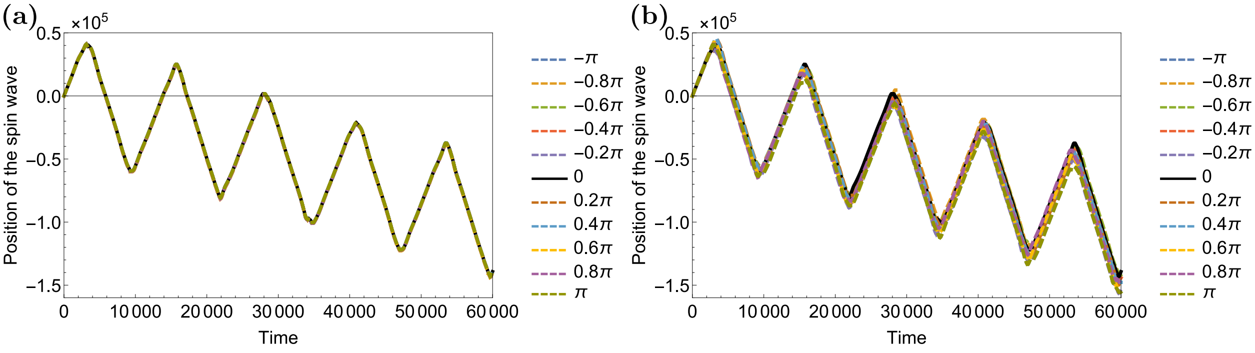

Figure C.2: Time-dependent position of the spin wave with initial wave vector $k = 11$ (in units of $(2\pi/1000)$) after the AC modulated magnonic crystal with $\omega_{ac} = 0.00316$ is switched on at $t = 0$. In (a) φ_s is varying at $\varphi_{ac} = 0$, while in (b) φ_{ac} is changing at $\varphi_s = 0$. Other parameters are $A = 2$, $q = 20 \times (2\pi/1000)$, $\gamma B_0 = 1$, and $\gamma \Delta B_0 = 0.001$.

To investigate the influence of different phases φ_s and φ_{ac} on the spin-wave propagation, we plot in Fig. C.2(a) the time-dependent positions of the spin waves with different initial phases φ_s when the AC magnonic crystal is activated; while in Fig. C.2(b) the spin-wave propagating curves with various φ_{ac} are shown for different AC magnonic crystals. We find from Figs. C.2(a) and C.2(b) that the effects of changing both φ_s and φ_{ac} on the spin-wave propagation are negligible. This can be explained by the strong inequality between $\gamma \Delta B_0$ and the spin-wave frequency ω_s. Note that, although the wave propagation is almost not affected by the changes of two phases; φ_{ac}, which is the phase in the AC modulation, directly enters into the evolution of the azimuthal angle of the spin-wave "qubit" (cf. Eq. (5.21) in Chapter 5).

It is worth pointing out that the propagation of the spin waves at the exact shifted resonance (see all curves in both Figs. C.2(a) and C.2(b) as well as the blue curve in Fig. 5.2(b) of Chapter 5) acquires a small negative average slope. This is caused by the difference between the velocities of the right- and left-propagating wave components in Eqs. (5.19) and (5.20). Namely, for the given ω_{ac} and δk, we have $(\Omega + \omega_{ac}/2)/k_{+} < (\Omega - \omega_{ac}/2)/k_{-}$.

C.3 Spin-wave Dynamics under π-pulse

To study the spin-wave dynamics under the π-pulse, we simulate the evolution of the spin wave while the magnonic crystal is switched on, and then, after completing the *half period* of the to-and-fro motion, is turned off. This is done by numerically solving Eq. (5.1) with the free spin-wave initial condition. The results are presented in Fig. C.3. It demonstrates clearly that after sending the DC π-pulse, the initially right-propagating spin wave with $k = 10$ (in units of $(2\pi/1000)$) is scattered backward to the state $k = -10$, while other waves with wave vectors $k = 11$ and 12 are still propagating forward (see Fig. C.3(c)). Furthermore, the simulations presented in Figs. C.3(e) and C.3(g) show that if the frequency of the AC π-pulse is properly tuned, then the spin wave with the *pre-selected* wave vector will be scattered by this pulse. For example, in Fig. C.3(e) we observe that only the spin wave with initial wave vector $k = 11$ is reflected to $k = -9$ by the AC π-pulse with $\omega_{ac} = 0.00316$. Besides, in Fig. C.3(g), when $\omega_{ac} = 0.00632$ is exploited, the spin wave which initially has $k = 12$ is scattered backward to the state with $k = -8$. Note that the complete backward scatterings of the spin waves with different wave vectors (see the magenta, orange, and cyan waves in Figs. C.3(c), C.3(e), and C.3(g), respectively) are equivalent to the flips of the corresponding spin-wave "qubits" from the north pole to the south pole by sending π-pulses (cf. Figs. C.3(b), C.3(d), and C.3(f)).

C.4 Spin-wave Packet

Up to now, the magnonic dynamics was studied only for the extended states, while in reality, the spin waves are sent as wave packets. For completeness, we simulated the evolution of a spin-wave packet when sending an AC $\pi/2$-pulse to the system. In this simulation, we initiate a wave

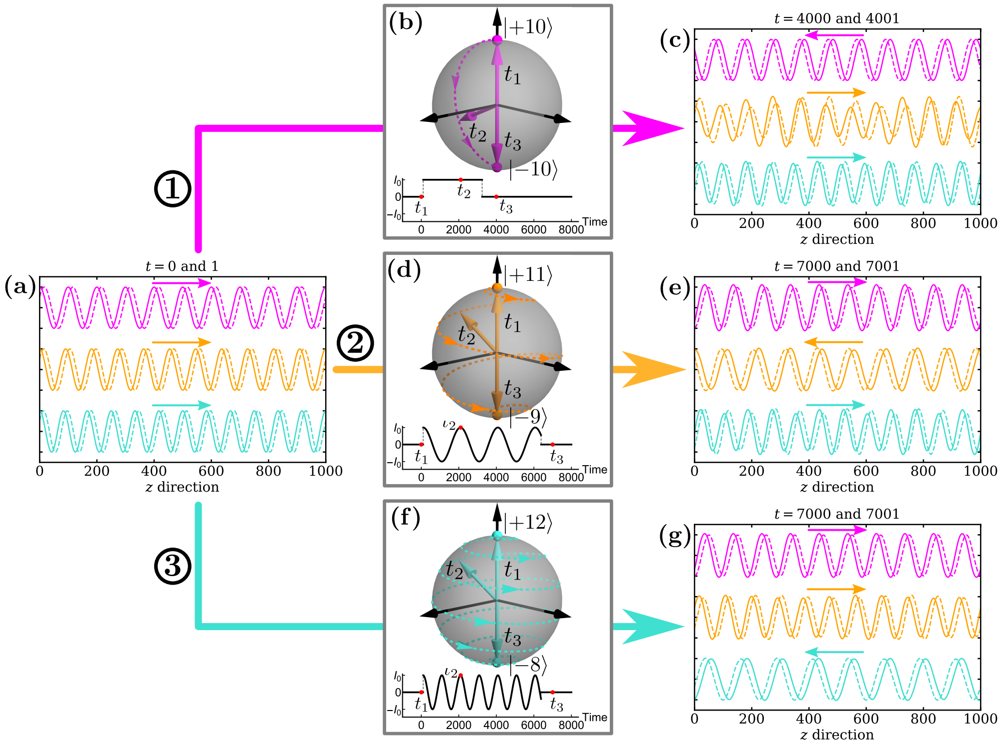

Figure C.3: Propagating directions of the spin waves before (subfigure (a)) and after (subfigures (c), (e) and (g)) sending the π-pulses as shown in (b), (d), and (f). The initial wave vectors, given in units of $(2\pi/1000)$, are $k = 10$ (magenta), 11 (orange), and 12 (cyan). To indicate the directions of the wave propagation, the spin-wave solutions $S^x(z,t)$ are plotted at two consecutive time points (the dashed ones are shown at the time after the solid ones), see also the colored arrows. From (a) to (c): a DC pulse, as shown in (b), was activated at $t = 100$ and turned off at $t = 3241$. The pulse has the duration $\Delta T = \pi/\gamma\Delta B_0 = 3141$, which is the half period of the to-and-fro motion under the DC magnonic crystal. From (a) to (e), and (a) to (g): the AC modulated π-pulses of the duration $\Delta T = 6283 \approx 2\pi/\gamma\Delta B_0$ were applied with the AC frequencies $\omega_{ac} = 0.00316$ and 0.00632 (cf. (d) and (f)), respectively. Subfigures (b), (d), and (f) also show the Bloch-sphere representation (see Eq. (5.21) in Chapter 5) of the time evolution of the resonantly coupled spin waves while sending the corresponding DC or AC π-pulse. Two resonantly coupled states $|k\rangle$ and $|k-q\rangle$ are represented as the north and south poles on the Bloch spheres. In subfigure (b), the waves with the wave vectors 10 and -10 are resonantly connected; in subfigure (d), the states $|11\rangle$ and $|-9\rangle$ are coupled; while in subfigure (f), the waves with the wave vectors 12 and -8 are paired. The trajectories of the states are presented as the dashed curves with the arrowheads on the surface of each Bloch sphere. The position of the states at three different times t_1, t_2, and t_3 (as indicated in the lower plots), are shown by the colored 3D arrows. The states initially located at the north poles is moved to the south poles by the corresponding π-pulses. The duration of the AC π-pulse is twice of the DC one. The parameters used for the simulations are $A = 2$, $q = 20 \times (2\pi/1000)$, $\gamma B_0 = 1$, $\Delta = \gamma\Delta B_0 = 0.001$, $\varphi_s = 0$, and $\varphi_{ac} = 0$. Time is measured in units $1/\gamma B_0$. *Main observation:* Waves satisfying the resonance conditions (the regular or shifted ones) change the direction of propagation, while those which are out of the resonance preserve their direction.

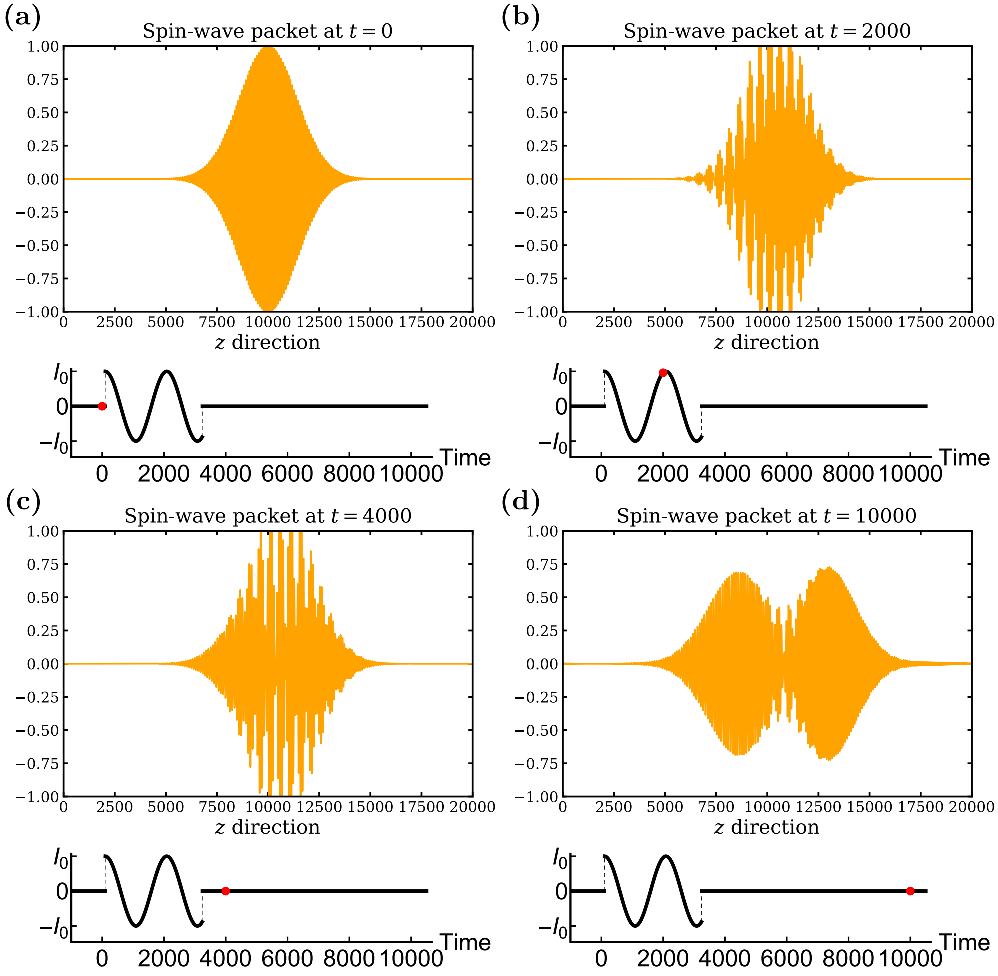

Figure C.4: Time evolution of the Gaussian spin-wave packet under the influence of the AC $\pi/2$-pulse. The wave packet has an initial form $S^{+}(z, t = 0) = e^{-[(z-z_0)/w]^2} e^{ik_0 z}$; and we plot $S^{x}(z, t)$ at (a) $t = 0$, (b) $t = 2000$, (c) $t = 4000$, and (d) $t = 10000$ (measured in units $1/\gamma B_0$). The time-dependent AC $\pi/2$-pulse are shown in the lower part of each subfigure with the red dot to indicate at which time point the wave is potted. The parameters used in this simulation are $A = 2$, $q = 20 \times (2\pi/1000)$, $\gamma B_0 = 1$, $\Delta = \gamma \Delta B_0 = 0.001$, $\omega_{ac} = 0.00316$, $\varphi_{ac} = 0$, $z_0 = 10000$, $w = 2000$, and $k_0 = 11 \times (2\pi/1000)$.

packet, which has the center wave vector $k_0 = 11 \times (2\pi/1000)$ and the wave-vector spreading $\Delta k \sim 1/w \approx 0.08 \times (2\pi/1000)$. For the chosen parameters, k_0 is at the exact shifted resonance and the wave-vector spreading is also within the resonant interval (cf. Fig. 5.2(b) in Chapter 5). As it is shown in Fig. C.4, after sending the $\pi/2$-pulse, the initial wave packet splits into two counter-propagating packets. From that, we conclude that the scattering of a spin-wave packet remains to be observable and the discussed mechanisms of spin-wave control can be functioning as well, provided that the energy spread (spectral extent) of the packet is within the gap and the meander structure is long enough to confine the to-and-fro motion of the wave packet.